



University of Kentucky  
UKnowledge

---

Theses and Dissertations--Mechanical  
Engineering

Mechanical Engineering

---


2023

## MULTISCALE MODELING OF CARDIAC GROWTH AND BAROREFLEX CONTROL

Hossein Sharifi

*University of Kentucky*, [hossein.sharifi@uky.edu](mailto:hossein.sharifi@uky.edu)

Author ORCID Identifier:

 <https://orcid.org/0009-0008-4955-254X>

Digital Object Identifier: <https://doi.org/10.13023/etd.2023.216>

[Right click to open a feedback form in a new tab to let us know how this document benefits you.](#)

### Recommended Citation

Sharifi, Hossein, "MULTISCALE MODELING OF CARDIAC GROWTH AND BAROREFLEX CONTROL" (2023).  
*Theses and Dissertations--Mechanical Engineering*. 212.  
[https://uknowledge.uky.edu/me\\_etds/212](https://uknowledge.uky.edu/me_etds/212)

This Doctoral Dissertation is brought to you for free and open access by the Mechanical Engineering at UKnowledge. It has been accepted for inclusion in Theses and Dissertations--Mechanical Engineering by an authorized administrator of UKnowledge. For more information, please contact [UKnowledge@lsv.uky.edu](mailto:UKnowledge@lsv.uky.edu).

## **STUDENT AGREEMENT:**

I represent that my thesis or dissertation and abstract are my original work. Proper attribution has been given to all outside sources. I understand that I am solely responsible for obtaining any needed copyright permissions. I have obtained needed written permission statement(s) from the owner(s) of each third-party copyrighted matter to be included in my work, allowing electronic distribution (if such use is not permitted by the fair use doctrine) which will be submitted to UKnowledge as Additional File.

I hereby grant to The University of Kentucky and its agents the irrevocable, non-exclusive, and royalty-free license to archive and make accessible my work in whole or in part in all forms of media, now or hereafter known. I agree that the document mentioned above may be made available immediately for worldwide access unless an embargo applies.

I retain all other ownership rights to the copyright of my work. I also retain the right to use in future works (such as articles or books) all or part of my work. I understand that I am free to register the copyright to my work.

## **REVIEW, APPROVAL AND ACCEPTANCE**

The document mentioned above has been reviewed and accepted by the student's advisor, on behalf of the advisory committee, and by the Director of Graduate Studies (DGS), on behalf of the program; we verify that this is the final, approved version of the student's thesis including all changes required by the advisory committee. The undersigned agree to abide by the statements above.

Hossein Sharifi, Student

Dr. Jonathan F. Wenk, Major Professor

Dr. Jonathan F. Wenk, Director of Graduate Studies

MULTISCALE MODELING OF CADIAC GROWTH AND BAROREFLEX  
CONTROL

---

DISSERTATION

---

A dissertation submitted in partial fulfillment of the  
requirements for the degree of Doctor of Philosophy in the  
College of Engineering  
at the University of Kentucky

By  
Hossein Sharifi  
Lexington, Kentucky  
Director: Dr. Jonathan F. Wenk, Professor of Mechanical Engineering  
Lexington, Kentucky  
2023

Copyright © Hossein Sharifi 2023  
<https://orcid.org/0009-0008-4955-254X>

## ABSTRACT OF DISSERTATION

### MULTISCALE MODELING OF CARDIAC GROWTH AND BAROREFLEX CONTROL

The heart functions within a complex system that adapts its function to any alteration in loading via several mechanisms. For example, the baroreflex is a short-term feedback loop that modulates the heart's function on a beat-to-beat basis to control arterial pressure. On the other hand, cardiac growth is a long-term adaptive response that occurs over weeks or months in response to changes in left ventricular loading. Understanding the mechanisms that drive ventricular growth and biological remodeling is critical to improving patient care. Multiscale models of the cardiovascular system have emerged as effective tools for investigating G&R, offering the ability to evaluate the effects of molecular-level mechanisms on organ-level function.

This dissertation presents MyoFE, a multiscale computer model that simulates the left ventricle (LV) pumping blood around a systemic circulation by bridging from molecular to organ-level mechanisms. The model integrates a baroreflex control of arterial pressure using feedback to regulate heart rate, intracellular  $\text{Ca}^{2+}$  dynamics, the molecular-level function of both the thick and thin myofilaments, and vascular tone. MyoFE is extended via a growth algorithm to simulate both concentric growth (wall thickening / thinning) and eccentric growth (chamber dilation / constriction). Specifically, concentric growth is controlled by the time-averaged total stress over the cardiac cycle, while eccentric growth responds to time-averaged intracellular myofiber passive stress.

Our integrated model replicated clinical measures of left ventricular growth in two types of valvular diseases - aortic stenosis and mitral regurgitation - at two different levels of severity for each case. Furthermore, our results showed that incorporating the effects of baroreflex control of arterial pressure in simulations of left ventricular growth not only led to more realistic hemodynamics, but also impacted the magnitude of growth. Specifically, our results highlighted the role of regulating venous compliance (vasoconstriction) by the baroreflex immediately after the onset of valvular diseases, which has a significant role on the extent of LV growth in the long term.

**KEYWORDS:** Multiscale modeling, Heart mechanics, Cardiac growth, Baroreflex, Left ventricle, Valvular disease

Hossein Sharifi

---

04/14/2023

---

Date

MULTISCALE MODELING OF CARDIAC GROWTH AND  
BAROREFLEX CONTROL

By  
Hossein Sharifi

Jonathan F. Wenk  
\_\_\_\_\_  
Director of Dissertation

Jonathan F. Wenk  
\_\_\_\_\_  
Director of Graduate Studies

04/14/2023  
\_\_\_\_\_  
Date

DEDICATION

To my wife, Azi.

## ACKNOWLEDGMENTS

I would like to take this opportunity to express my heartfelt gratitude to the individuals who have played an instrumental role in the successful completion of my dissertation. First and foremost, I would like to thank my advisor, Dr. Jonathan F. Wenk, for his unwavering support, guidance, and mentorship throughout my doctoral journey. Dr. Wenk's expertise, feedback, and encouragement have been invaluable, and I am truly grateful for everything I have learned under his supervision.

I would also like to extend my sincere appreciation to my PhD committee members, Dr. Christine Trinkle, Dr. Martha E. Grady, and Dr. Kenneth S. Campbell. Their insightful feedback, constructive criticism, and support have been instrumental in shaping my research and guiding me towards a successful dissertation defense. I have been fortunate to benefit from their wealth of knowledge and expertise, and I will always be grateful for their contributions to my academic and professional growth.

I would also like to take this opportunity to express my gratitude to my family for their unwavering love and support throughout my academic journey. To my wife, Azi, I am forever grateful for your love, patience, and endless support. You have been my rock, my confidante, and my best friend, and I could not have completed this journey without you by my side.

To my mother and father, thank you for instilling in me a love of learning and for supporting me every step of the way. Your encouragement, guidance, and sacrifices have been a constant source of inspiration, and I am truly grateful for everything you have done for me.



To my sister, thank you for your support, encouragement, and understanding throughout this journey. Your belief in me has been a constant source of motivation, and I am lucky to have you as my sister.

Finally, to my niece, Lia, thank you for bringing joy and light into our life. Your smile, laughter, and curious nature have reminded me of the importance of pursuing one's passions and always striving for excellence. I hope that one day you will look back on my dissertation and feel proud of your uncle's achievements.

# TABLE OF CONTENTS

ACKNOWLEDGMENTS.....	iii
LIST OF TABLES .....	viii
LIST OF FIGURES.....	ix
CHAPTER 1. Multiscale simulations of left ventricular growth and remodeling .....	1
1.1 Introduction.....	1
1.2 Current computational models of G&R .....	6
1.2.1 Volumetric growth theory .....	7
1.2.2 Constrained mixture theory .....	11
1.3 Limitations of current models.....	14
1.3.1 Contractile model of the heart .....	14
1.3.2 Hemodynamic feedback control .....	18
1.3.3 Reverse growth.....	19
1.3.4 Clinical application.....	21
1.3.5 Model calibration and validation .....	22
1.4 Future perspectives .....	23
1.4.1 Multiscale modeling of cardiac G&R.....	23
1.4.2 Machine learning and multiscale modeling of cardiac G&R.....	27
CHAPTER 2. A multiscale finite element model of left ventricular mechanics incorporating baroreflex regulation      31	
2.1 Introduction.....	31
2.2 Methods .....	34
2.2.1 Overview .....	34
2.2.2 Circulation .....	35
2.2.3 LV model geometry.....	37
2.2.4 Cardiac electrophysiology .....	38
2.2.5 Finite element formulation .....	38
2.2.6 Cardiac mechanics.....	40
2.2.7 Baroreflex.....	45
2.3 Results .....	50
2.3.1 Response to changes in user-defined arterial pressure setpoints .....	50
2.3.2 Response to acute increase in aortic resistance .....	53
2.3.3 Response to acute mitral regurgitation .....	56
2.3.4 Response to acute myocardial infarction.....	58
2.4 Discussion .....	65
2.5 Limitations.....	69
2.6 Summary and Conclusion.....	70
CHAPTER 3. Multiscale Finite element modeling of left ventricular growth in simulations of valve disease      71	

3.1	<i>Introduction</i> .....	71
3.2	<i>Methods</i> .....	74
3.2.1	Overview .....	74
3.2.2	Finite element formulation .....	75
3.2.3	Cardiac mechanics.....	77
3.2.4	Growth constitutive model .....	78
3.2.5	Separation of timescales between growth and elastic deformation .....	80
3.2.6	Simulation cases .....	83
3.3	<i>Results</i> .....	85
3.3.1	Concentric growth was captured in response to pressure overloading .....	85
3.3.2	Eccentric growth was captured in response to volume overloading .....	87
3.3.3	Effects on the pressure-volume relationship.....	89
3.3.4	Reversal of growth when the perturbation was removed.....	90
3.4	<i>Discussion</i> .....	92
3.4.1	Role of myofiber passive stress in driving eccentric growth.....	93
3.4.2	Role of myofiber total stress in driving concentric growth .....	94
3.4.3	Integration of LV growth with a mechanistic model of half-sarcomeres at myosin-level.....	95
3.4.4	Reversal of growth .....	96
3.5	<i>Limitations</i> .....	98
3.6	<i>Summary and conclusion</i> .....	99
CHAPTER 4. Role of Baroreflex Feedback Loop in LV Growth Prediction: A Multiscale Finite Element Modeling Study in Valvular Diseases .....		101
4.1	<i>Introduction</i> .....	101
4.2	<i>Method</i> .....	104
4.2.1	Circulation.....	105
4.2.2	LV model geometry.....	107
4.2.3	Finite element formulation of elastic deformation .....	107
4.2.4	Cardiac mechanics.....	108
4.2.5	Baroreflex.....	108
4.2.6	Growth constitutive model .....	110
4.2.7	Separation of timescales between growth and elastic deformation .....	112
4.2.8	Clinical data.....	115
4.2.9	Simulation cases .....	116
4.3	<i>Results</i> .....	119
4.3.1	Concentric growth in response to pressure overloading.....	119
4.3.2	Eccentric growth in response to volume overloading.....	121
4.3.3	Pressure-volume relationships .....	123
4.3.4	Baroreflex impacted both hemodynamics and magnitude of growth .....	125
4.3.5	The coupled baroreflex-growth model reproduced left ventricular characteristics measured in clinical data.....	129
4.4	<i>Discussion</i> .....	131
4.4.1	Overview .....	131
4.4.2	Capturing various timescales.....	131
4.4.3	Importance of baroreflex in simulations of LV growth .....	133
4.5	<i>Limitations</i> .....	137
4.6	<i>Summary and conclusion</i> .....	138

CHAPTER 5. Summary and future work .....	139
5.1 Summary of CHAPTER 1 .....	139
5.2 Summary of CHAPTER 2 .....	140
5.3 Summary of CHAPTER 3 .....	141
5.4 Summary of CHAPTER 4 .....	141
5.5 Future work .....	142
APPENDICES.....	145
APPENDIX 1. FILE S1.....	145
APPENDIX 2. FILE S2.....	170
APPENDIX 3. FILE S3.....	185
APPENDIX 4. SUPPLEMENTARY FIGURES.....	199
REFERENCES.....	203
VITA .....	215

## LIST OF TABLES

<i>Table 2.1 Baroreflex implementation functions.</i> .....	47
<i>Table 4.1 Utilized studies for collecting clinical data</i> .....	116
<i>Table 4.2 Simulated levels of severity for aortic stenosis (AS)</i> .....	117
<i>Table 4.3 Simulated different levels of severity for mitral regurgitation (MR)</i> .....	118

## LIST OF FIGURES

<i>Figure 1.1 Highlights on computational modeling of cardiac growth, based on volumetric growth theory and fiber remodeling, throughout the last three decades.</i>	6
<i>Figure 1.2 Schematic showing how <math>F_e</math>, <math>F_g</math>, <math>F_e^*</math> and <math>F</math> map between configurations in volumetric growth theory.</i>	8
<i>Figure 1.3 Schematic showing finite deformation of a soft tissue according to constrained mixture model.</i>	12
<i>Figure 1.4 Kinetic scheme.</i>	18
<i>Figure 1.5 Multiscale patient-specific modeling scheme for Hypertrophic Cardiomyopathy (HCM).</i>	30
<i>Figure 2.1 Overview of the MyoFE framework.</i>	34
<i>Figure 2.2 Myofiber orientation with a linear transmural variation from <math>60^\circ</math> at the endocardium to <math>-60^\circ</math> at the epicardium.</i>	37
<i>Figure 2.3 Kinetic scheme.</i>	44
<i>Figure 2.4 Simulation demonstrating baroreflex control of arterial pressure for increasing <math>P_{set}</math> by 30 mmHg.</i>	51
<i>Figure 2.5 Simulation demonstrating baroreflex control of arterial pressure for decreasing <math>P_{set}</math> by 30 mmHg.</i>	53
<i>Figure 2.6 The baroreflex stabilizes arterial pressure when aortic resistance is acutely increased.</i>	54
<i>Figure 2.7 The model cannot maintain arterial pressure without baroreflex when aortic resistance is acutely increased.</i>	55
<i>Figure 2.8 The baroreflex stabilizes arterial pressure when acute mitral regurgitation is induced.</i>	57
<i>Figure 2.9 The model cannot maintain arterial pressure without baroreflex when mitral regurgitation is induced.</i>	58
<i>Figure 2.10 Simulation of acute myocardial infarction.</i>	60
<i>Figure 2.11 Myofiber active contractile stress increased in the remote region in the model with baroreflex control of arterial pressure.</i>	61
<i>Figure 2.12 Pressure-volume loop shifted rightward for MI simulations compared to baseline.</i>	62
<i>Figure 2.13 Baroreflex regulation of thin filament parameters related to intracellular <math>Ca^{2+}</math> transient before and after mimicking acute myocardial infarction.</i>	63
<i>Figure 2.14 Baroreflex regulation of thick filament parameters related to myofilament contractility before and after mimicking acute myocardial infarction.</i>	64
<i>Figure 3.1 Integration of the central framework of MyoFE with a growth algorithm.</i>	75
<i>Figure 3.2 Scheme for imposing LV growth using the updated reference configuration approach.</i>	82
<i>Figure 3.3 The growth algorithm predicted thickening of the LV in response to pressure overloading.</i>	86
<i>Figure 3.4 The growth algorithm dilated LV in response to volume overloading.</i>	88
<i>Figure 3.5 Predicted pressure-volume relationships.</i>	90
<i>Figure 3.6 Reversal of LV growth in response to removal of valvular diseases. AS: Aortic stenosis, MR: Mitral regurgitation</i>	92
<i>Figure 4.1 Overview of MyoFE framework.</i>	105
<i>Figure 4.2 Growth algorithm predicted more hypertrophy (wall thickening) in response to higher pressure overloading.</i>	120
<i>Figure 4.3 Growth algorithm predicted more dilation in response to higher volume overloading.</i>	122
<i>Figure 4.4 Pressure-volume relationships in response to volume and pressure overloading.</i>	124
<i>Figure 4.5 Impact of baroreflex on capturing concentric growth.</i>	126
<i>Figure 4.6 Impact of baroreflex on eccentric growth.</i>	128
<i>Figure 4.7 Model validation with measured clinical data.</i>	130

## CHAPTER 1. MULTISCALE SIMULATIONS OF LEFT VENTRICULAR GROWTH AND REMODELING

This chapter is adopted from Sharifi et al. [1] with permission.

### 1.1 Introduction

The heart, whose primary function is to pump blood through the circulatory system in a regulated manner, is a complex organ that is governed by multiple physics operating across multiple scales. It is able to adapt its geometry [2] and function [3, 4] accordingly with acute or chronic alterations in pumping demand. Similar to skeletal muscle [5], the myocardial cells that make up the heart muscle [6], can evolve in size and dimension in response to neurohormonal, chemical, and mechanical stimulus signals. This process, referred to as cardiac growth and remodeling (G&R), includes sub-processes at the cellular level such as sarcomerogenesis [7] and myocardial fibrosis [8]. At the organ level, this hypertrophic response, depending on the disease, is manifested through wall thickening and/or chamber dilation. Usually in the field of cardiac biomechanics, the term “cardiac growth” refers to changes in the geometry of the heart, whereas “cardiac remodeling” refers to changes in material properties of the cardiac tissue, induced by myofiber disarray, myocardial fibrosis, and altered contractility.

Cardiac G&R can occur due to physiological-related demands (physiological hypertrophy) like pregnancy and athletic activities, or it can happen in response to pathological demands (pathological hypertrophy) such as valvular dysfunction and genetic mutation. Both types of cardiac G&R initiate as an adaptive response to the underlying

stimuli, but are significantly different in terms of the molecular mechanisms, signaling pathways, and the ultimate clinical outcome [2] as briefly described below.

Physiological hypertrophy is considered as an adaptive mechanism where the cardiac mass increases due to the growth of cardiomyocytes in both length and width. A heart with physiological hypertrophy has preserved or even increased systolic function. However, this increase does not lead to changes in extracellular matrix or fibrosis [9]. In addition, physiological hypertrophy is a fully reversible phenomenon, except for the postnatal hypertrophy. For example, the left ventricular dimension in trained athletes is significantly larger than non-athletic individuals [10, 11], but can return to a normal size after training is stopped [12]. During pregnancy, elevated hormones [13], increased blood volume, and cardiac output [14] cause the left ventricle (LV) to undergo an adaptive hypertrophy that returns to the normal condition within two weeks postpartum [15].

Pathological hypertrophy is classified as an early adaptive and compensatory response to abnormal ventricular loading or mutant sarcomeric proteins [16]. Prolonged pathological hypertrophy, however, can be maladaptive, causing myocardial fibrosis and altering myocyte function (e.g.,  $\text{Ca}^{2+}$  handling) that can impair systolic or diastolic function, which in turn, can lead to irreversible growth and heart failure [6, 17]. There are 2 classical types of pathological hypertrophy that are defined based on ventricular geometry resulting from the disease. 1) Concentric hypertrophy is when the LV wall thickens and cardiac mass increases with little or no change in the chamber volume because of the parallel deposition of sarcomeres in cardiomyocytes [6]. 2) Eccentric hypertrophy or dilated hypertrophy is when the chamber volume dilates and cardiac mass increases with a small change in the wall thickness due to the serial addition of sarcomeres and



lengthening of cardiomyocytes [6]. Although many heart diseases can produce these 2 types of pathological cardiac hypertrophy, three prevalent causes are illustrated in the following.

Pressure overloading is an external abnormal mechanical loading in which the ventricular afterload increases. To overcome the elevated afterload, the contractile stress in the sarcomeres increases to generate enough force to pump blood out of the LV and into the rest of the body [18]. In accordance with *Laplace's Law*, the heart increases the ventricular wall thickness by deposition of sarcomeres in parallel to alleviate the elevated wall stress. This wall thickening can result in diastolic dysfunction and impaired filling of the LV, which in turn, can lead to heart failure [19]. This is the characteristic feature of concentric hypertrophy that is generally seen during pressure overloading. Among the different types of disorder in the vasculature that can cause pressure overloading, hypertension is arguably the most common one. It can be either the primary cause or the secondary outcome of other diseases like kidney or thyroid disorders [20, 21]. Another prevalent cause of pressure overloading is aortic stenosis, a valvular disease where the aortic valve does not open properly or becomes narrow [22]. A stenotic valve can happen due to congenital heart defects, like a bicuspid aortic valve [23], or the deposition of calcium on the aortic valve [24].

Volume overloading is another type of abnormal ventricular loading in which the LV is filled with excess blood during diastole, which results in an elevated ventricular preload [18]. Valvular disorders that lead to imperfect closure of the valves are the most prevalent cause of volume overloading. For instance, mitral valve regurgitation occurs when the mitral valve does not close properly during systole, causing back flow of the

blood into the left atrium, which in turn, increases diastolic filling of the ventricle [25]. Similarly, aortic valve regurgitation is another type of valvular disorder where the aortic valve does not tightly close during diastole, which leads to overloading of the LV by retrograde flow of blood from the aorta back into the LV [26]. Excessive filling of the LV results in overstretching of sarcomeres, which initiates the process of sarcomerogenesis whereby the number of sarcomeres is increased in series [7]. This elongation process essentially re-establishes the sarcomeres back to an optimal force-generating length [5]. Eccentric hypertrophy is a distinctive outcome of volume overloading whereby the dilated chamber would preserve the stroke volume in response to excessive diastolic filling [27]. According to *Laplace's Law*, dilation of the chamber volume elevates the wall stress because of the reduction in  $h/r$  ratio [18] where  $h$  and  $r$  are the ventricular wall thickness and chamber radius, respectively, but will be normalized by wall thickening of the LV to preserve the mass-to-volume ratio [28].

Hypertrophic cardiomyopathy (HCM) is the most common form of genetic heart disease, which is caused by mutations in the sarcomeric proteins in the myocardium [29]. It has been reported that patients with HCM are at high risk for atrial fibrillation, as well as heart failure and sudden death [30]. Although HCM has been known to cause sudden death in youths, including athletes, it has also been reported as the cause of death in all age groups [31]. There are various mutations to the genes that encode the proteins of cardiac sarcomeres, which can lead to the onset of HCM at different time points over a life span [32, 33]. These mutations lead to hypercontractile sarcomeres by destabilizing the super-relaxed state of myosin heads, increasing myofilament activation, lowering efficient energy usage, and impairing  $\text{Ca}^{2+}$  cycling and sensitivity [34-36]. These underlying perturbations

at the cellular level trigger the signaling pathways that induce cardiac hypertrophy to accommodate for the elevated contractile function of the heart. The hallmark feature of HCM is asymmetrical hypertrophy, especially in the septal wall, along with myocardial fibrosis and myofiber disarray [37].

Computer and mathematical modeling of cardiac G&R has seen significant developments since its emergence nearly 30 years ago [38]. Computational cardiac G&R models have the potential to enhance our understanding of the complex interaction/behavior of how living systems adapt, especially when they are validated with experimental data collected at multiple scales. This is accomplished by developing mathematical relations between the underlying stimuli (e.g., mechanical signals) and the potential outcomes in the geometry and function of the heart (e.g., LV wall thickening, LV chamber dilation, myofiber disarray, hypercontractility). These computational models have helped to quantitatively investigate the effects of different hypotheses, such as the choice of mechanical stimuli [39, 40] and the reversal of cardiac hypertrophy [41], on the hypertrophic behavior of the heart. With recent developments in cardiac G&R models, along the other computational models of the heart, it has been predicted that we will have comprehensive patient-specific models of the heart within the next decade [42].

The objective of this review is to provide an overview of the current state of the art in computational modeling of cardiac G&R and discuss how the current models can be improved before implementation into personalized models for clinical use. To serve this purpose, in section 2, we summarize the most common computational models of cardiac G&R, including volumetric growth of the LV and myofiber remodeling. In section 3, we consider the limitations of the current models that need to be addressed. Finally, in section

4, we discuss the future perspective of the field and explain how computational models can improve patient care in the future.

## 1.2 Current computational models of G&R

Computational models have been extensively developed and applied to simulate cardiac G&R (Figure 1.1). In the following subsections, we recapitulate the key findings of current computational modeling of cardiac G&R.

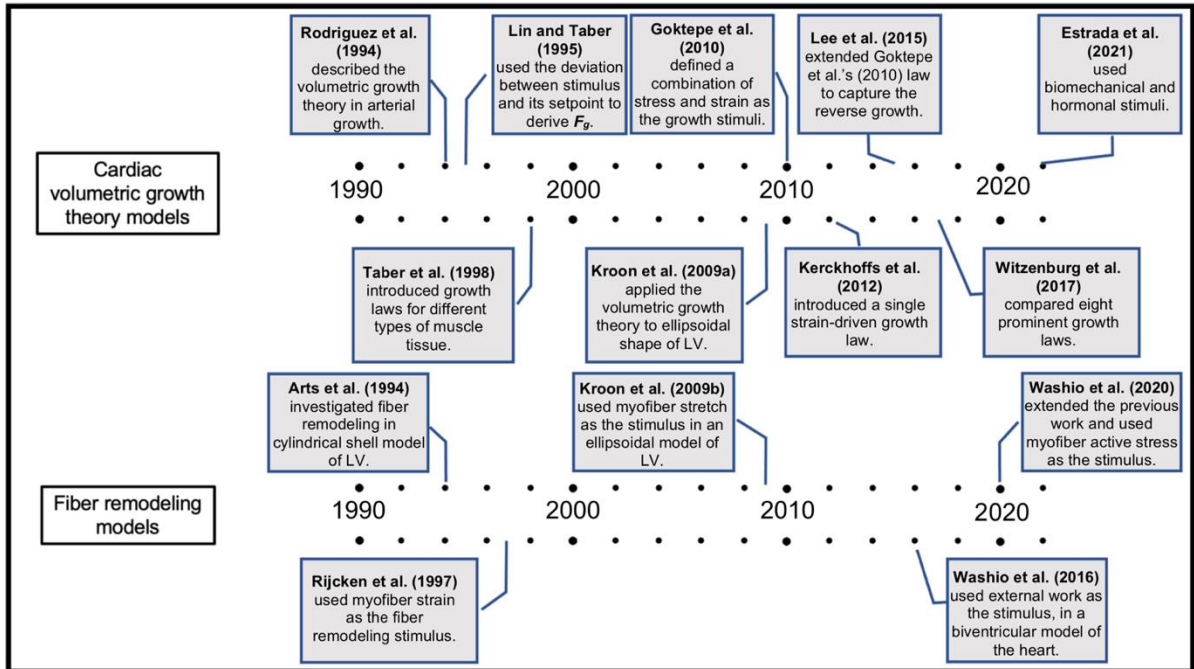


**Figure 1.1** Highlights on computational modeling of cardiac growth, based on volumetric growth theory and fiber remodeling, throughout the last three decades.

### 1.2.1 Volumetric growth theory

One of the most prevalent frameworks in modeling growth is “volumetric growth theory”. Utilizing the idea of a multiplicative decomposition of the deformation gradient  $\mathbf{F}$  from continuum plasticity, Rodriguez et. al [38] proposed splitting the deformation gradient as:

$$\mathbf{F} = \mathbf{F}_e \mathbf{F}_g \quad (1.1)$$

In this way, local changes in mass can be specified directionally via the inelastic growth tensor  $\mathbf{F}_g$  as shown in Figure 1.2 Applying  $\mathbf{F}_g$  maps the reference configuration  $\beta^0$  to an intermediate configuration  $\beta^*$  due to the stress-free removal or addition of material. Conventionally, addition in the fiber direction represents the serial addition of sarcomeres, while addition in the sheet and sheet normal directions represent the parallel addition of sarcomeres. In general, however,  $\beta^*$  is not guaranteed to be “kinematically” compatible, meaning that gaps and overlaps can form. Compatibility is restored by applying an elastic deformation  $\mathbf{F}_e^*$  that restores continuity in the absence of any external loads, which can produce residual stresses (i.e., non-zero stresses without the presence of external load). In fact, this framework has been used to model the existence of residual stresses observed in vivo [43-45]. The total current configuration  $\beta$  is achieved by applying  $\mathbf{F}_e$  to the intermediate configuration  $\beta^*$ . As growth occurs,  $\mathbf{F}_e$  is altered, changing the stress response of the tissue for a given load.

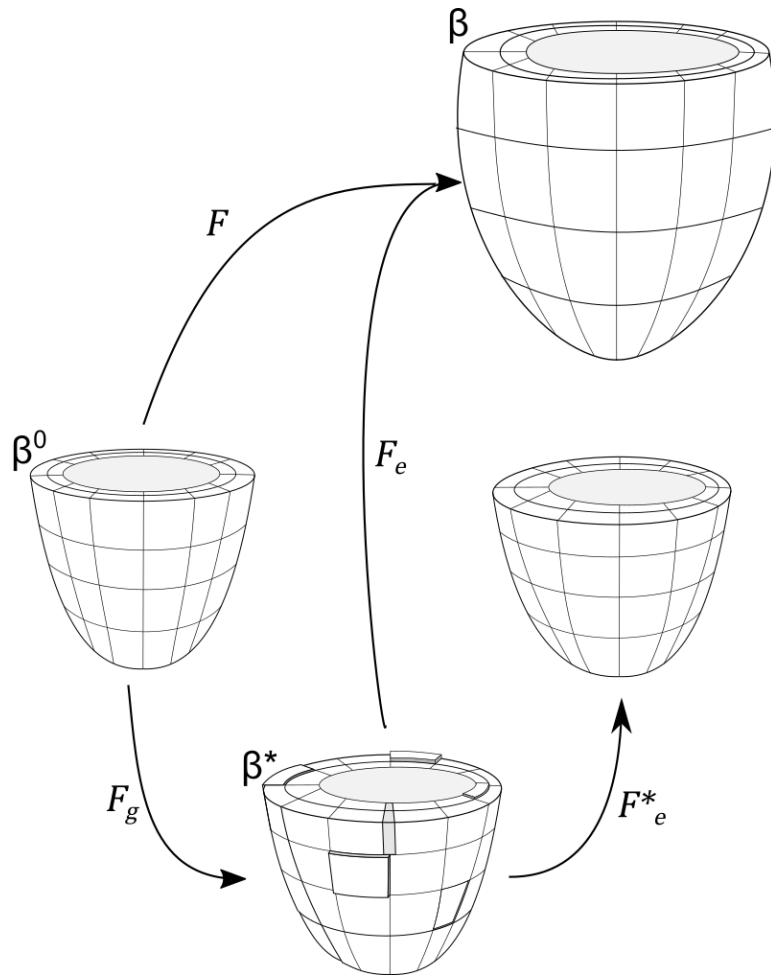


**Figure 1.2 Schematic showing how  $F_e$ ,  $F_g$ ,  $F_e^*$  and  $F$  map between configurations in volumetric growth theory.**

Ultimately  $F$  maps from the reference configuration  $\beta^0$  to the loaded, grown and deformed configuration  $\beta$ .  $F_g$  maps from  $\beta^0$  to  $\beta^*$  representing the stress-free removal or addition of material. This configuration is not necessarily compatible, as shown via discontinuities and overlaps here. Compatibility is restored via  $F_e^*$  to a new unloaded geometry. Finally,  $F_e$  maps from the incompatible grown configuration  $\beta^*$  to the final loaded configuration  $\beta$ .

This framework was originally used extensively in modeling arterial growth [46-50] and growth in the developing heart [51-55]. Lin and Taber [51] introduced the evolution of  $F_g$  as a differential equation involving the deviation of a growth stimulus from its homeostatic value. The first application of this framework to the geometry of a ventricle was by Kroon et al. [56]. This work simulated inhomogeneous growth in 3D and extended the framework by updating the reference configuration incrementally as growth occurs. This led to steady state growth in which the growth stimulus (deviation of end-diastolic myofiber strain from a homeostatic value) decreases as a steady state configuration is reached.

Much of the focus since has been on the development of constitutive growth laws that govern the formulation of  $F_g$ . The question of what stimulus/stimuli is the driver of growth is still debated [57], but conventionally, cardiac growth models use either stress, strain, or some combination of the two as their stimulus for driving the evolution of  $F_g$ . Grossman et al. [28] found that peak systolic wall stress was consistent between normal hearts and those that experienced concentric or eccentric growth, leading to a hypothesis that fiber stress is a stimuli for growth. Stress regulated growth has been used to successfully model cardiac growth in response to hypertension [58], myocardial infarction [59], and recently to analyze the effects hypertrophy has on the electromechanics of the LV [60].

Though Grossman's hypothesis supports stress as a valid mechanical stimulus, Emery and Omens [61] found that diastolic stresses remain elevated during growth, but end diastolic fiber strains return to normal, suggesting that strain may be the dominant growth stimulus in response to volume overload. Guterl et al. [62] further supports strain

as the regulator for cardiac growth after experiments on long-term cultured right ventricular papillary muscles showed that systolic stress played no role in the observed growth. Kroon et al. [56] used end-diastolic strain in their work to model growth during diastolic loading, comparing approaches that utilized either fixed or updated reference configurations. Kerckhoffs et al. [63] proposed a strain driven growth law that was able to qualitatively capture growth in response to both pressure and volume overload with a single set of growth parameters. This work was extended in 2018 by Witzenburg & Holmes [64], connecting Kerckhoffs' growth law to a compartmental model of the heart, which in turn was coupled with a circulatory model. They were able to quantitatively match multiple independent sets of growth data for pressure and volume overload as well as growth in response to myocardial infarction. In 2015 and 2016, Lee et al. [41, 65] extended the framework proposed by Goktepe et al. [66], using a strain based growth law to predict the reversal of growth, as well as growth, integrating it into an electromechanical model of the heart. Genet et al. [67] incorporated a strain-based growth law in a four-chamber model of the heart, predicting growth and also secondary effects such as valvular position and papillary muscle position. Recent studies on strain-driven growth include modeling forward and reverse growth due to cardiac dyssynchrony [68], incorporating multiscale and machine learning to analyze the predictive power of a strain based growth model [69], and incorporating an evolving set point to better predict growth reversal [70]. Some works used a combination of stimuli for deriving their growth model. Goktepe et al. [66] pre-selected the stimulus, using strain for eccentric growth and stress as the stimulus for concentric growth. Similarly, Berberoglu et al. [71] switched between stimuli when modeling cardiac dysfunction in grown hearts.



Recent works have focused more heavily on trying to deduce the best stimulus/combination of stimuli to accurately produce stable growth as well as incorporating more multiscale, mechanistic features. Witzenburg & Holmes [72] compared eight existing growth laws in response to cyclical stretches meant to represent either volume or pressure overload. They found that only two models [51, 63] could reach a steady state growth in both simulations and also highlighted the need to accurately capture evolving hemodynamics. In a recent work, Mojumder et al. [39] showed myofiber stress has a better correlation with the predicted concentric growth in response to pressure overloading using finite element modeling. Though not utilizing the volumetric framework, the studies performed by Rondanina and Bovendeerd [40, 73] concluded that (1) using at least one stress based stimulus and (2) accurately modeling hemodynamics, specifically hemodynamic feedback to maintain mean arterial pressure, yields a model that is able to capture growth while maintaining realistic pump function. Estrada et al. [74] and Yoshida [75] have recently incorporated cell level hormone networks into their models of growth. As with most modeling, the shift from phenomenological towards mechanistic models will drive the field forward regarding predictive capability and may shed light on the most relevant growth stimuli, mechanical or otherwise.

### **1.2.2 Constrained mixture theory**

Another approach for modeling of G&R is based on the constrained mixture theory [76]. According to this theory, the different constituents of tissue (cell, collagen, elastin, etc.) have distinct production/turnover rates, and are constrained to deform within a single continuum mixture. The key hypothesis in this theory is that deposition of new material for each constituent occurs at the current configuration. According to the constrained mixture

theory, constituent  $\alpha$  deposits in a preferred direction at time  $\lambda \in [0, s]$  with a homeostatic stretch or pre-stretch of  $\mathbf{G}^\alpha(\lambda)$ . If we assume  $\mathbf{F}(s)$  and  $\mathbf{F}(\lambda)$  are the deformation gradient of the whole continuum from a reference configuration at  $t = 0$  to the configurations at time  $s$  and  $\lambda$ , respectively, then  $\mathbf{F}(s)\mathbf{F}(\lambda)^{-1}$  accounts for deformation gradient of the whole continuum from time  $\lambda$  to the current configuration at time  $s$ . Consequently, the deformation gradient of constituent  $\alpha$  from time  $\lambda$  to the current configuration at time  $s$  can be formulated as  $\mathbf{F}_n^{\alpha(\lambda)}(s) = \mathbf{F}(s)\mathbf{F}(\lambda)^{-1}\mathbf{G}^\alpha(\lambda)$  (Figure 1.3).

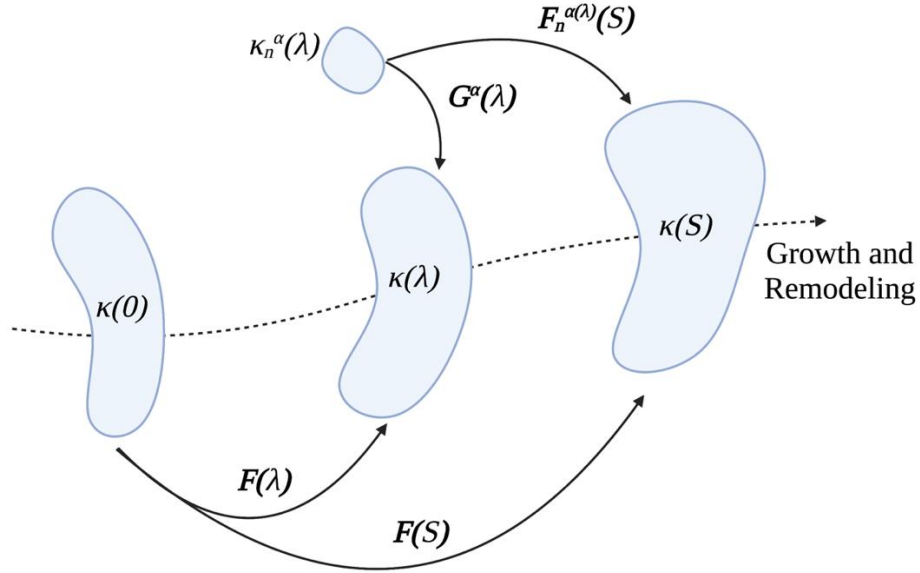


**Figure 1.3 Schematic showing finite deformation of a soft tissue according to constrained mixture model.**

Each constituent  $\alpha = 1, 2, \dots, n$  deposits within the current mixture with a preferred deposition stretch  $\mathbf{G}^\alpha(\lambda)$  at G&R time of  $\lambda \in [0, s]$  from its stress-free configuration of  $\kappa_n^\alpha(\lambda)$ . However, the constituent  $\alpha$  may have a different deformation because all constituents are constrained to deform within a single continuum from the configuration at time of  $\lambda$ ,  $\kappa(\lambda)$ , to current configuration at time  $s$ ,  $\kappa(s)$ . Constituent-specific deformation gradient associated with constituent-specific stored energy function then can be formulated as  $\mathbf{F}_n^{\alpha(\lambda)}(s) = \mathbf{F}(s)\mathbf{F}(\lambda)^{-1}\mathbf{G}^\alpha(\lambda)$ .

Constrained mixture theory has been widely used in G&R models of arteries and vessels [77, 78]. There are several reviews on constrained mixture-based G&R model, where the bulk of its mathematical background are summarized. For example, Ateshian

and Humphrey [79] reviewed the application of this theory to various illustrations of biological G&R and identified open problems in the field. Valentin and Holzapfel [80] summarized the core hypotheses integrated in constrained mixture theory of arterial G&R and recapitulated the remarkable findings. In the most recent study, Humphrey [81] reviewed the constrained mixture theory introduced twenty years ago and explored its application in various types of vascular conditions.

Compared to volumetric growth theory, constrained mixture modeling is computationally more complex because it needs to track the evolution of each constituent's stress-free configuration at each growth time step. Therefore, constrained mixture models have been mainly used on arterial G&R by assuming simple 2D geometry e.g. thin-wall membrane [80, 82]. To the best of our knowledge, no study has implemented the constrained mixture theory into cardiac G&R, and only a few studies have implemented 3D finite element models of arterial G&R based on constrained mixture theory [78, 83, 84].

Although constrained mixture theory is not routinely employed in the field of cardiac G&R, Yoshida and Holmes [85] suggested this approach might address some limitations of volumetric growth theory for cardiac G&R. First, they observed that as the new constituent replaces the old one with a unique turnover rate, the homeostatic configuration evolves in such a way that the new stage is fundamentally different from the original ungrown stage. The authors suggested that the evolution of the homeostatic configuration in constrained mixture theory might be a better suited solution for evolving the growth setpoint, which was already suggested to be a potential solution for capturing the reversal of cardiac growth when the pressure overloading is removed [70]. Second, they

suggested this approach might have some advantages in the modeling of myocardial fibrosis since it allows the modeling of different constituents of cardiac tissue. Hence, this approach will potentially address some limitations of kinematic (volumetric) growth theory and enhance the computational modeling of cardiac G&R.

### **1.3 Limitations of current models**

The current state of the art for cardiac G&R has certain limitations, which have hindered its use in clinical applications. In order to implement computational modeling into clinical care and improve patient outcomes, these limitations need to be addressed. Several of these key limitations are outlined as follows.

#### **1.3.1 Contractile model of the heart**

Several models of cardiac G&R [41, 51, 56, 59, 66] have only operated under passive loading of the LV (diastole) and neglected the active contractile behavior of myocardium during systolic ejection. In these models, the ventricular pressure was incrementally increased up to the end-diastolic pressure and then was kept constant to allow the ventricle to grow. Another group of works evaluated cardiac G&R during the full cardiac cycle by simulating both passive and active phases of cardiac function. Most of these models [63, 65, 68, 86] utilized phenomenological Hill-type models of contraction to simulate the LV during systole. This model of contractile mechanics defines the magnitude of active force using a length-dependent force generation model [87, 88]. Other studies [64, 74] have used a time-varying elastance model of the ventricle [89, 90] to simulate the full cardiac cycle. This model essentially assumes an exponential end-diastolic pressure-volume relationship and a linear end-systolic pressure-volume relationship. The pressure-

volume relationship for any points between these two is described by a smooth time-varying function. Rondanina and Bovendeerd recently investigated the effects of different mechanical stimuli on cardiac growth [40, 73]. In this case, the contractile behavior of the ventricle was modeled by a one-fiber model of cardiac function [91] and was used to relate mechanics at the organ level, via ventricular pressure and volume, to mechanics at the tissue level, via myofiber stress and sarcomere length.

Generally, the myocardium has two types of mechanical behavior, namely passive and active. The passive mechanical properties of myocardium are primarily related to collagen and titin that control the passive tension of the myocytes during ventricular diastole. Titin is a large protein that spans from the Z disk to the M line of sarcomeres [92], while collagen, as part of the ECM, surrounds and interconnects cardiac myocytes, muscle fibers, and the coronary microcirculation [93]. The active contractile mechanical properties of myocardium are related to the crossbridge cycling of myosin heads on the thick filament with actin binding sites on the thin filament, which drives the systolic behavior of the LV. This interaction is part of a cascade of multi-physics events that enable contraction. Briefly, an action potential leads to depolarization of the cell membrane, which activates  $\text{Ca}^{2+}$  channels and allows entry of  $\text{Ca}^{2+}$  into the cell.  $\text{Ca}^{2+}$  entry triggers the release of  $\text{Ca}^{2+}$  from the sarcoplasmic reticulum (SR) and increases the  $\text{Ca}^{2+}$  concentration within the cell [94]. Elevated  $\text{Ca}^{2+}$  concentration leads to the binding of  $\text{Ca}^{2+}$  to the myofilament troponin-C, which moves the tropomyosin on the surface of the thin myofilament. This exposes more available binding sites for attachment of myosin heads on the thick filament, which then generate the power stroke. For more insights on the regulatory system of myofilaments, we refer to the review by Solis and Solaro [95].

Although it is well accepted to simplify the sophisticated biological mechanisms of the beating heart in computational modeling, the contractile function is an integral process of the heart and should be modeled more accurately to allow the cardiac G&R to occur throughout the cardiac cycle, not just at certain timepoints such as end-diastole or end-systole. To our knowledge, none of the contractile models used in the current state of the art in cardiac G&R truly simulates the sliding of myofilaments based on the Huxley crossbridge formation [96] in the myosin level. To overcome this limitation, there are several models of sarcomere mechanics that could be employed, which describe the crossbridge cycling of myosin and actin binding sites using mathematical definitions [97-99]. These models typically assume a certain number of conformation states that myosin heads or binding sites can switch between throughout the contraction cycle based on the  $\text{Ca}^{2+}$  activation of actin binding sites. An example of a kinetic scheme is shown in Figure 1.4. The transition between these states is usually described by a system of ordinary differential equations (ODEs) that depend on the present population of myosin heads or binding sites at each state, and transition rate factors. The sarcomere contraction model proposed by Campbell et al. [97, 98], which captures length dependent activation, cooperativity between thick and thin filaments, and the strain-dependent behavior of cross-bridges, has successfully been implemented into several finite element models of LV mechanics. Zhang et al. [100] implemented this model of contraction into a finite element model of a rat LV, where the myosin heads were only able to move between the disordered relaxed (DRX) and force generating (FG) states. They showed that by considering key features of ventricular relaxation they could predict both the global function and regional deformation of the LV compared to measured data. Mann et al. [101] recently enhanced

that model by adding the super-relaxed (SRX) state for myosin heads and concluded that the force-dependent recruitment from the myosin SRX state increased the end-systolic pressure-volume relationship. This level of sarcomere mechanics has yet to be implemented in models of cardiac G&R. Although these types of contraction schemes can increase the complexity of computational models, cardiac G&R would occur under more realistic conditions that can quantitatively explain the relation between the pathological cardiac diseases observed at the organ level and cellular events at the myosin level.

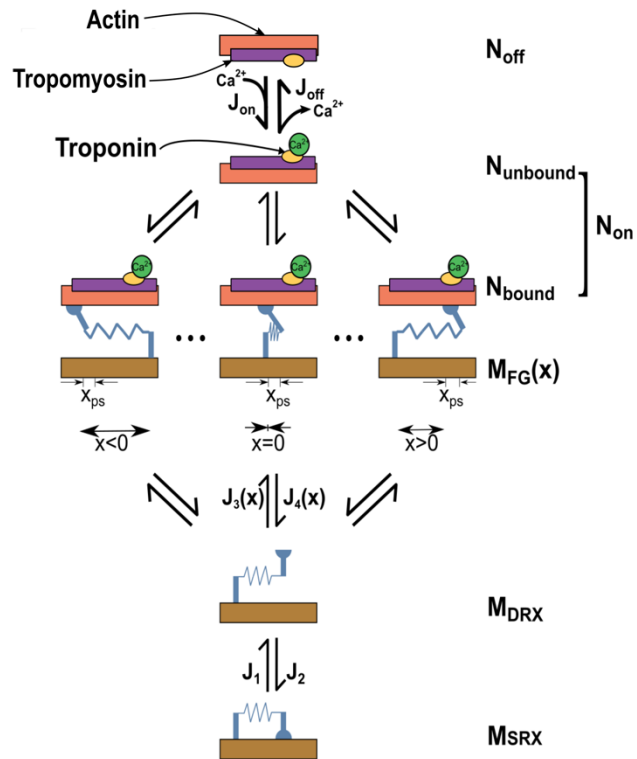


**Figure 1.4 Kinetic scheme.**

Sites on the thin filament switch between states that are available ( $N_{on}$ ) and unavailable ( $N_{off}$ ) for cross-bridges to bind to. Myosin heads transition between a super-relaxed detached state ( $M_{SRX}$ ), a disordered-relaxed detached state ( $M_{DRX}$ ), and a single attached force-generating state ( $M_{FG}$ ).  $J$  terms indicate fluxes between different states.

### 1.3.2 Hemodynamic feedback control

Valvular disorders, such as aortic stenosis and mitral regurgitation, change the ventricular loading and cardiac function, but the arterial pressure and cardiac output normally remain unchanged [102-104]. Current approaches to cardiac G&R have mainly focused on the geometry of the LV and paid less attention to hemodynamic feedback. The baroreflex loop is an important short-term hemodynamic feedback mechanism that maintains the arterial pressure by adapting the cardiac contractility, heart rate, and vascular



tone to acute changes in the ventricular loading. Current models are generally performed under constant heart rate and contractility assumptions, with no mechanisms for preserving the arterial pressure. The absence of hemodynamic feedback has been viewed as the potential cause of inaccuracy in certain model predictions of cardiac geometry and function, when compared to measured data. For example, Kerckhoffs et al. [63] reported a mismatch between the calculated peak LV cavity pressure and that measured in experiments, and posited that it could be due to the absence of fast baroreflex responses in their model. Recently, Rondanina and Bovendeerd [40] investigated the effect of mechanical stimulus signals on cardiac growth using a growth law lumped with a compartmental model of cardiovascular function. Their model erroneously predicted a 20% to 40% reduction in mean arterial pressure and cardiac output in response to aortic stenosis, aortic regurgitation, and mitral regurgitation. In their next study, Rondanina and Bovendeerd [73] incorporated a model of baroreflex feedback, along with their growth model, and suggested using a mixed stress-strain growth model in conjunction with a model of hemodynamic feedback could capture more realistic cardiac growth and preserved cardiac pump function.

### **1.3.3 Reverse growth**

The reversal of pathological hypertrophy is a primary goal of clinical interventions such as mitral valve replacement [105], aortic valve surgery [106], implementation of LV assist devices [107], cardiac resynchronization [108], and bioinjection hydrogel treatment [109-111]. These interventions essentially normalize the ventricular loading by reducing overloading conditions, which can improve function and positively alter ventricular geometry, ultimately leading to more favorable clinical outcomes. In terms of simulating

the onset of pathological hypertrophy, computational models of cardiac G&R enlarge the ventricular geometry when the underlying stimuli is higher than the homeostatic level. On the other hand, it is expected that during the reversal of an adverse event, when the stimulus signals are below the homeostatic level, the ventricle would shrink in order for the mechanical stimuli to return to their setpoint level.

However, current computational models have focused more on the prediction of “forward” cardiac growth and only a few works have tried to study the “reverse” of cardiac growth. Lee et al. [41] modified the eccentric growth law proposed by Goktepe et al. [66] and could successfully capture the “reverse” growth for a thick-walled cylindrical tube and realistic LV geometry under certain types of loading. Arumugam et al. [68] implemented a similar growth law into a biventricular FE model of the heart and used maximum elastic myofiber stretch over a cardiac cycle as the sole driving signal of their growth law. They lumped their growth model with an electromechanics model of the heart and showed that the model predicts growth in the LV chamber size and septal wall, but reversal of growth for RV chamber size and LV free wall in response to mechanical dyssynchrony. Recently, Yoshida et al. [70] adopted the growth law proposed by Kerckhoff et al. [63] into a biventricular FE model of the heart and investigated the regression of concentric growth due to the removal of pressure overloading. Although this growth law was shown in a study to perform the best in predicting cardiac hypertrophy in comparison to seven other growth laws [72], it was not able to predict the reversal of growth when the pressure overloading was lifted. The authors suggested that using an evolving growth setpoint might potentially address the inability of current models to predict the reversal of growth.

### 1.3.4 Clinical application

In addition to the model limitations described above, there are other types of limitations that have hindered the field from being applied to clinical care. These limitations are more general and are applicable to most multiscale models of the heart, including growth and remodeling.

Firstly, mathematical models of cardiac G&R are computationally expensive. The finite element method is widely used to simulate the mechanics of the heart by numerically solving partial-differential equations for each element in both time and space. The solution then needs to be integrated over the entire domain (whole geometry of the heart) at each time step. This process for 3-dimensional models that are non-linear and time dependent is computationally intensive and time-consuming, since it requires multiple hours to simulate a single cardiac cycle [112]. Secondly, these models, in general, require parameter identification and model calibration that add more sophistication in their application. Thirdly, computational models usually include uncertainties and variabilities that have limited their clinical application [113]. These uncertainties need to be quantified and propagated through different scales using statistical approaches, such as Bayesian inference and Gaussian process regression. Fourthly, performing computational models of cardiac G&R on the population scale is labor intensive. The number of trained technicians who can perform the computational simulations in comparison to the large pool of patients across the nation is lower, meaning that the ratio of demand over capacity is much larger than unity. Consequently, performing full patient-specific models of cardiac G&R for patients that need real-time results is not yet practical in the health care system.

### 1.3.5 Model calibration and validation

The accuracy of computational models of cardiac G&R can be assessed when they are calibrated and validated via experimental data. Animal models and clinical data from human patients are the main sources of measured experimental data. Animal models are more often used than patient data, since they are more available, and it is possible to conduct invasive measurements on them. On the other hand, acquiring data from human patients is more restricted and only procedures that are part of standard care, including non-invasive imaging techniques or measuring clinical data, are typically used.

Animal models provide the opportunity to validate computational models in different scales. Organ-level data are usually acquired using non-invasive imaging devices such as echocardiography or cardiac magnetic resonance images (MRI). Imaging data are mainly utilized to construct the patient-specific geometry of the LV, but can also provide information about myocardial deformation, such as displacement and strain. The predicted LV volume at end-diastole and end-systole, stroke volume, ejection fraction, and wall thickness can then be validated with the imaging data. This is also the case with regional strain patterns that are predicted by the model and then compared to *in vivo* measurements [100, 101]. Calculated myofiber remodeling can also be evaluated against the measured values from magnetic resonance diffusion tensor imaging (MR-DTI) [114]. At the cellular level, predicted hypertrophy is validated *ex vivo* by measured data for myocyte width and length, sarcomere number and length, and fibrosis from collected ventricular tissue samples

Model calibration is the adjustment of model parameters such that the model prediction best fit the data. However, the number of parameters in G&R models can be large, which in turn complicates the process of model calibration. A solution to this

complexity is to define simplified relations between them to reduce the number of free parameters [115]. One of the main free parameters in growth laws is growth rate or gain factor. This parameter controls the speed of the growth algorithm, and is usually adjusted in a way to fit the growth rate from the experimental data. Once the G&R model is calibrated, it needs to be validated against an independent set of measured data that has not been used in the calibration process. The process of model validation can be governed in two ways. First, the predicted results from computational models of cardiac G&R can be qualitatively compared with the experimental data by overlaying them in a single figure. A second approach is to quantitatively calculate the error between the computed results and measured ones over a range of inputs to quantify the level of agreement. This approach is comprised of statistical methods referred to as validation metrics. For more insights on different approaches for validation metrics, we refer to the review by Oberkampff and Baroneb [116].

## **1.4 Future perspectives**

### **1.4.1 Multiscale modeling of cardiac G&R**

Despite the limitations listed above, current models have done a reasonable job in simulating cardiac G&R due to extrinsic mechanical conditions such as valvular disorders [40, 63, 64], systemic and pulmonary hypertension [58], and myocardial infarction [59, 64]. However, cardiac G&R can occur due to intrinsic events, such as altered hormone level or mutant sarcomeric proteins, which have not been thoroughly investigated in the field of computational biomechanics. Multiscale modeling has the potential to solve many

of the issues with current cardiac G&R models and will most likely be the focus of cardiac biomechanics in the near future.

Inspired by the field of systems biology, there are several models that simulate the complex network of signaling pathways within the cell, which can predict cell growth in response to altered hormones. Ryall et al. [117] proposed a model of hypertrophic signaling pathways to predict the change in cell area of a cardiomyocyte in response to hormonal alteration and biomechanical stretching. Frank et al. [118] recently modified this model and validated it with *in vivo* data from multiple mouse models. Yoshida et al. [75] investigated pregnancy-induced cardiac growth by coupling a signaling pathway network that could predict the cell-level hypertrophy with a compartmental model of the rat heart in a circulatory system. Ultimately, they simulated the pregnancy condition by developing volume overload in conjunction with a surge in hormone levels. Their model successfully predicted cardiac growth in response to pregnancy that is consistent with experimental data, and concluded that most of the growth, especially during the first half of pregnancy, was due to an early rise in progesterone. Estarada et al. [74] went further and proposed a multiscale model of cardiac hypertrophy by adopting this approach into a finite element model of a LV, to investigate the prediction of concentric hypertrophy in response to transverse aortic constriction (TAC), which includes both elevated afterload along with the change in hormone levels. Interestingly, they concluded that the hormonal inputs had a larger effect than the mechanical signals in the prediction of hypertrophy due to TAC. Both studies emphasized the importance of multiscale modeling of cardiac growth wherein they could monitor the interaction of both mechanical and hormonal stimuli in the development of cardiac growth.

Multiscale modeling of cardiac G&R could also be beneficial in quantitatively studying familial hypertrophic cardiomyopathy (HCM). This type of genetic heart disease-- known as an intrinsic cause of cardiac hypertrophy--is mainly induced by mutant sarcomeric proteins. Different types of mutations associated with either the thick or thin myofilaments can cause HCM. Although the underlying mechanism of mutant genes and development of HCM is not completely clear, numerous mutations in the genes of sarcomeres have been identified that lead to HCM. Genetic mutations associated with the myosin heavy chain (*MYH7*) and myosin binding protein C (*MYBPC3*) are the most common cause of HCM [29, 119]. In general, these mutations affect the motor function of myosin heads, potentially destabilizing the SRX state and increasing the number of myosin heads that can interact with actin. Another outcome of thick filament mutations is the increase of energy required for myosin ATPase, which in turn can reduce the activity of other ATP-consuming processes such as sarcoendoplasmic reticulum  $\text{Ca}^{2+}$  ATPase [SERCA] [35]. HCM mutations can also occur in thin filament genes including cardiac troponin T (*TNNT2*), cardiac troponin I (*TNNI3*),  $\alpha$ -tropomyosin (*TPMI*), and cardiac actin (*ACTC*). The thin filament associated mutations ultimately lead to alterations in the  $\text{Ca}^{2+}$  balance within the cell by increasing the sensitivity of troponin C for calcium [35, 120]. Eventually, all of these molecular-level perturbations alter the signaling pathways [2] and develop hypercontractile sarcomeres [34] that lead to asymmetrical hypertrophy in the septal wall, along with myofiber disarray.

To date, no computational models have studied cardiac G&R in response to HCM. Here, we briefly hypothesize two potential solutions for modeling of HCM across multiple scales, from molecular-level to organ-level. The first solution to fill this gap is to lump a

model of the signaling pathway network, wherein it represents the interaction of pathological biochemical stimuli involved in HCM, with a mechanical model of cardiac G&R. In this approach, the effects of mutant genes, which disturb the signaling pathway within the myocardial cell, can be observed on larger scale events such as LV hypertrophy and myofiber remodeling. However, since HCM is a disease of the sarcomeres, it is important to simulate the mechanics of sarcomeres in a biologically relevant way and mimic the effects of mutant genes at the molecular level. Therefore, the second solution could be utilizing a mechanistic model of sarcomeres, rather than phenomenological models, for simulating the contractile behavior of the heart. As described in section 3, coupling a model of sarcomere mechanics, which simulates the interaction of myosin heads and actin binding sites to generate the active contractile force, with a model of cardiac G&R could be very beneficial. Due to the ability of these models, perturbations in molecular-level events such as an increased number of accessible heads to interact with actin binding sites, elevated ATPase, or even perturbed  $\text{Ca}^{2+}$  handling, can be quantitatively predicted [121]. Thus, implementing a growth law that utilizes these perturbations in molecular events as the stimuli to predict cardiac growth, in terms of ventricular size, would be a remarkable success in the field of cardiac biomechanics. In addition to growth of the LV, hypercontractile sarcomeres will lead to the development of myofiber disarray in the myocardium of HCM patients [122]. In the study by Avazmohammadi et al. [123], the authors emphasized that multiscale modeling of the heart was needed to better understand the myofiber remodeling that was observed in the presence of pulmonary arterial hypertension. With this in mind, the “prospective” multiscale model of HCM (Figure 1.5) can be completed by incorporating a model of myofiber reorientation as well as volumetric



growth. Consequently, the effect of key perturbations in molecular and cellular events on the growth of the LV and myofiber reorientation/disarray can be predicted simultaneously. This level of multiscale modeling will also have the ability to simulate the effects of pharmaceutical interventions for treating HCM, such as small molecule therapeutics, which would be a milestone step in the field of cardiac biomechanics.

#### **1.4.2 Machine learning and multiscale modeling of cardiac G&R**

Although advances in multiscale modeling of living matter, such as cardiac G&R, can provide more insight on the underlying mechanisms, it can introduce more complexity into the computational models in terms of both physics and parameters [124, 125]. That is why the fully patient-specific model of the heart seems theoretically possible, but practically computationally expensive and labor intensive, which has hindered the field from being applied to clinical care [42]. Machine learning is recognized as a powerful tool in the biological, biomedical, and behavior sciences that integrates multi-modality and multi-fidelity data to identify the correlation among different phenomena. However, this technique weakens when dealing with sparse data [124]. Physics-based models, such as multiscale models, have been found helpful to address this issue. Essentially, machine learning can be integrated with multiscale models to learn both the underlying mechanisms (physics) in terms of governing equations and boundary equations [126], and the model parameters for a particular physics-based problem. On the other hand, multiscale models can utilize machine learning to identify the correlation, characterize the system parameters, and quantify the uncertainties between scales. Therefore, machine learning and multiscale models can mutually complement and benefit one another. In recent years, machine learning has been successfully integrated with patient-specific multiscale models of the

heart and showed promising results in predicting LV mechanics [112, 127], cardiac activation mapping [128], and risk predictions of sudden cardiac death [129].

In general, the concept of growth and remodeling of living matter is most applicable to the field of biomechanics, in conjunction with machine learning [130]. Multiscale modeling of cardiac G&R, in particular, can benefit from being integrated with machine learning. At the basic research phase, machine learning and multiscale modeling can complement one another. Specifically, techniques from machine learning can identify the correlations for different growth stimuli from the measured (i.e. experimental and/or clinical) data, while multiscale modeling of cardiac G&R can assess the causality of the phenomena with the highest correlation [124]. Secondly, the predictive power of growth laws can be quantified before being applied to clinical care cases. For instance, Peirlinck et al. [69] quantified that their stretch-driven growth law can explain 52.7% of the changes in myocyte length in response to mitral regurgitation. Thirdly, the uncertainties from the experimental and clinical data can be quantified and then propagated throughout the physics-based computational models using techniques from machine learning, such as Bayesian inference and Gaussian process regression [69, 131]. Fourthly, machine learning can learn the underlying dynamic system of cardiac G&R from the multiscale modeling and identify the system parameters such as growth factors, homeostatic level of stimuli signals, etc., based on the trained dataset.

Ultimately, the full patient-specific multiscale models of cardiac G&R can be replaced by surrogate models through the integration of machine learning and multiscale models, which are computationally more efficient. These surrogate models use experimental, clinical, computational, and multi-modality imaging data from different

scales and sources to predict the prognosis of cardiac G&R in response to various cardiovascular diseases. By moving the field closer to real-time predictive models, this event will be a big achievement towards the application of multiscale modeling in clinical cardiac care.

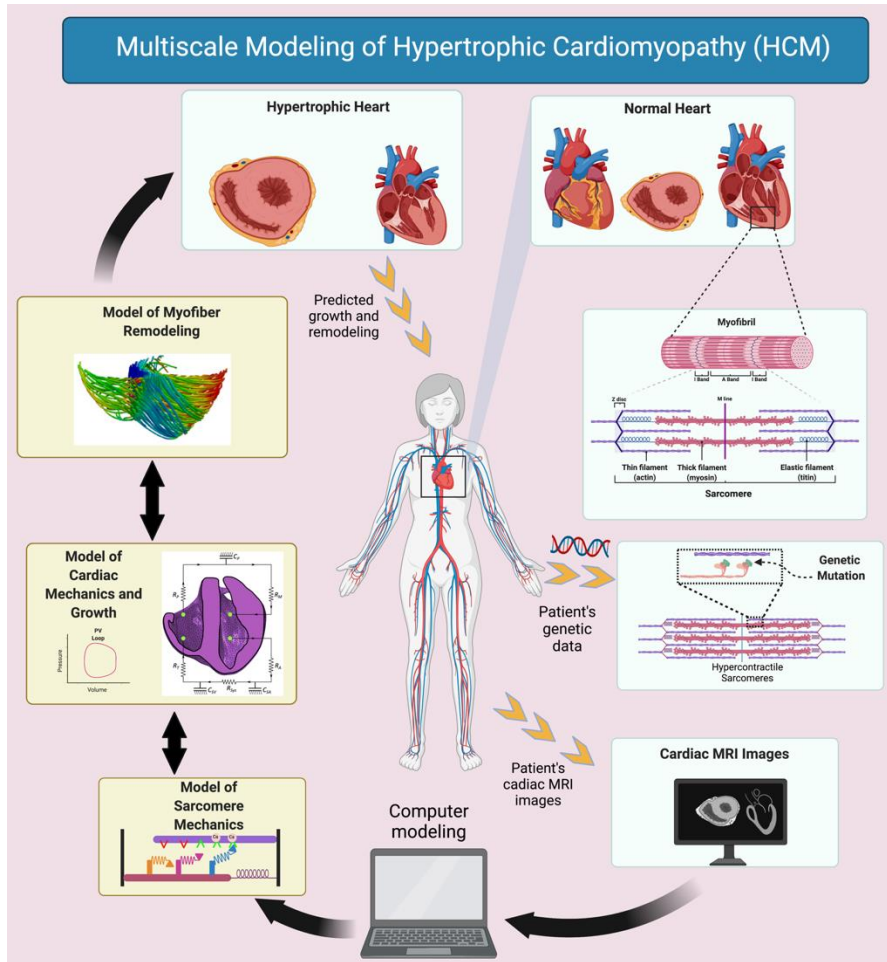


**Figure 1.5 Multiscale patient-specific modeling scheme for Hypertrophic Cardiomyopathy (HCM).** A patient’s genetic data drives the model properties of the sarcomere mechanics and determines the HCM mutations. Cardiac magnetic resonance images (MRI) form the patient-specific geometry of the heart for computational modeling. A multiscale model of HCM then predicts the progression of cardiac growth and remodeling (G&R) in response to specific mutations associated with HCM. The bi-ventricular scheme of the heart for “Model of Cardiac Mechanics and Growth” subfigure is adopted from Sack et al. with permission [132]. The schematic subfigure for “Model of Myofiber Remodeling” is adopted from Washio et al. with permission [133].

## 2.1 Introduction

The heart functions as part of a complex feedback loop known as the hemodynamic reflex or baroreflex loop, which helps regulate blood pressure and blood flow to the various organs of the body. The loop involves interactions between the heart, blood vessels, and blood pressure receptors in the cardiovascular system. The loop starts with changes in blood pressure and blood flow, which trigger signals to the heart and blood vessels. These signals are interpreted by the baroreceptors, specialized sensory nerve endings located in the blood vessels that monitor blood pressure changes.

If blood pressure is too low, the baroreceptors signal the heart to increase heart rate and contractile force, while simultaneously constricting the blood vessels, leading to an increase in cardiac output and blood pressure. This helps maintain the blood pressure within a normal range. On the other hand, if blood pressure is too high, the baroreceptors signal the heart to slow down heart rate, decrease contractile force, and relax blood vessels, leading to a decrease in cardiac output and blood pressure [134]. This in turn helps maintain the blood pressure within a normal range as well. Overall, the hemodynamic reflex loop helps ensure that the heart and blood vessels are functioning in a coordinated manner to maintain an optimal balance between blood pressure and blood flow.

Several previous studies have sought to mathematically simulate the beating heart. Such models could produce insights into cardiovascular physiology and might be

employed to improve the diagnosis and treatment of disease [42]. These studies have focused on different aspects of cardiovascular modeling, using techniques that range from a relatively simple model of left ventricle (LV) geometry [64, 86] to sophisticated 3D finite element-based approaches that incorporate growth and remodeling algorithms [65, 68]. However, the majority of existing models perform under a set of predefined conditions (e.g. constant heart rate, peak contractile stress, etc.) that ignore the adaptive response of the heart to disease driven perturbations. Some groups, on the other hand, have focused on modeling the effects of the baroreflex in controlling arterial blood pressure, but have simplified other aspects of their model. For example, Ursino [135] integrated a detailed model of carotid baroregulation that could capture the dynamics of different neuron pathways in the regulation of arterial blood pressure. However, this approach used a time-varying elastance model of the LV that ignored the complex torsional motion of the heart. Using a similar method, other groups [136, 137] implemented different aspects of the baroreflex into their model, but did not capture the regulation of the contractile function of the myocardium at the myosin level.

In our previous work, we introduced a multiscale model of cardiovascular function that was able to control arterial pressure at user-defined homeostatic setpoints by regulating heart rate, function of myofilaments at the molecular-level,  $\text{Ca}^{2+}$  dynamics, and vascular tone [138]. Although it was not intended to represent a complete and fully detailed model of the baroreflex, it demonstrated how the implemented hemodynamic reflex loop could maintain arterial pressure when challenged by different perturbations. However, since our previous approach was limited to using a one-dimensional hemispherical model of the LV, based on Laplace's law, it is unable to capture the effect of heterogenous changes in

myocardial properties. Thus, the model cannot account for alterations caused by diseases such as hypertrophic cardiomyopathy [139] or myocardial infarction (MI) [140], which induce spatially heterogeneous changes in the LV.

To better represent the spatial variations associated with myocardial infarction, a 3D finite element (FE) model of the LV is required to distinguish between infarcted and healthy tissue [110, 141]. To serve this purpose, we have incorporated a baroreflex feedback loop with a 3D multiscale FE model of the beating LV, which is built in the FEniCS open-source framework. The baroreflex algorithm in this study is inspired by our prior work [138]. However, instead of regulating the contractile function of a single half-sarcomere, the contractility of all myofibers across the entire LV can be regulated to control arterial pressure. Similar to our previous work, the baroreflex approach is based on a dynamic model that approximates the interaction of neural processing in the medulla and signaling pathways in effector cells. The model is driven by an afferent signal, resulting from alterations in arterial pressure, and outputs a control signal that is bounded between the maximum sympathetic and maximum parasympathetic drive. In response, the control signal modulates heart rate and vascular tone, as well as intracellular  $\text{Ca}^{2+}$  dynamics and the molecular-level function of both the thick and the thin filaments at each integration point in the mesh. The results of the current study will demonstrate that the algorithm can regulate arterial pressure at user-defined setpoints, as well as maintain arterial pressure in the presence of perturbations such as acute cases of aortic stenosis, mitral regurgitation, and myocardial infarction.

## 2.2 Methods

### 2.2.1 Overview

The model described in Figure 2.1 is called MyoFE. This framework is essentially a higher dimension version of the PyMyoVent model of cardiovascular function [138] in which the 1D model of LV mechanics was replaced with a more sophisticated 3D FE model of the LV. In the current framework, a pacing stimulus activates a 2-compartment model of electrophysiology that drives the  $\text{Ca}^{2+}$  transient at each integration point across the mesh. The  $\text{Ca}^{2+}$  transient then triggers the contractile behavior of the myofilaments, which is driven by a molecular-level model named MyoSim [97, 98]. Finally, the LV chamber pumps blood through a lumped parameter model of systemic circulation.

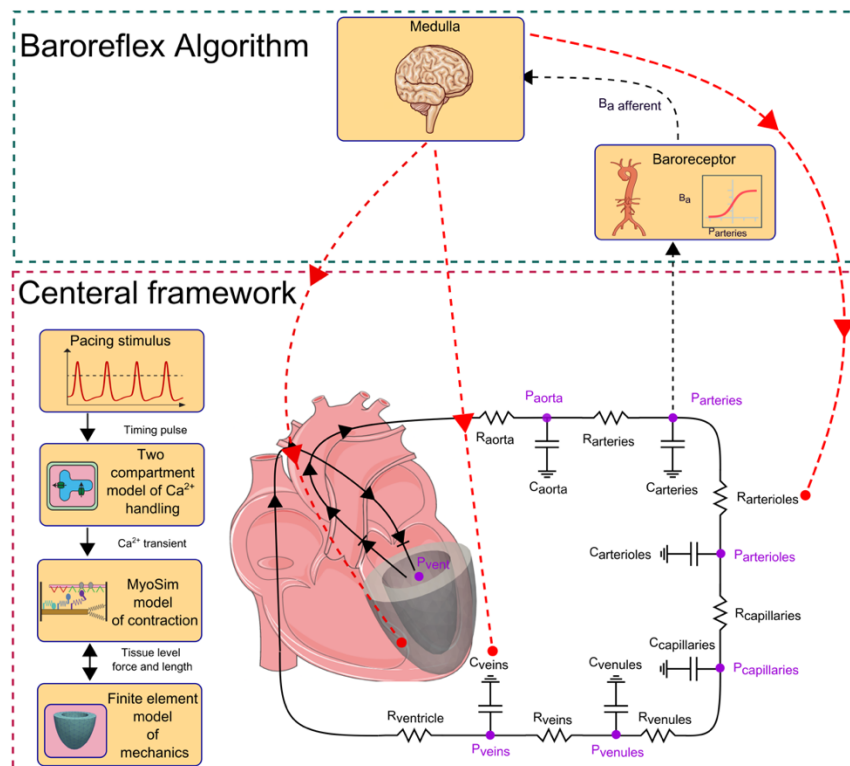


**Figure 2.1 Overview of the MyoFE framework.**

The baroreflex algorithm controls arterial pressure by regulating heart rate, intracellular  $\text{Ca}^{2+}$  handling, myofilament contractility, and vascular tone.



## 2.2.2 Circulation

As shown in Figure 2.1, the circulatory model only simulates the systemic circulation. In addition to the LV, there are six other compartments, namely the Aorta, Arteries, Arterioles, Capillaries, Venules, and Veins that each have a compliance  $C_i$  and resistance  $R_i$ , where  $i$  indicates the compartment. The rate of change of blood volume within each compartment is defined as the difference between the blood that flows into and out of the compartment:

$$\begin{aligned}
 \frac{dV_{\text{aorta}}}{dt} &= Q_{\text{LV to aorta}} - Q_{\text{aorta to arteries}} \\
 \frac{dV_{\text{arteries}}}{dt} &= Q_{\text{aorta to arteries}} - Q_{\text{arteries to arterioles}} \\
 \frac{dV_{\text{arterioles}}}{dt} &= Q_{\text{arteries to arterioles}} - Q_{\text{arterioles to capillaries}} \\
 \frac{dV_{\text{capillaries}}}{dt} &= Q_{\text{arterioles to capillaries}} - Q_{\text{capillaries to venules}} \\
 \frac{dV_{\text{venules}}}{dt} &= Q_{\text{capillaries to venules}} - Q_{\text{venules to veins}} \\
 \frac{dV_{\text{veins}}}{dt} &= Q_{\text{venules to veins}} - Q_{\text{veins to LV}} \\
 \frac{dV_{\text{LV}}}{dt} &= Q_{\text{veins to LV}} - Q_{\text{LV to aorta}}
 \end{aligned} \tag{2.1}$$

The blood flow between neighboring compartments is governed according to Ohm's law and is associated with the pressure gradient between the two compartments and the resistance of the compartment that the blood flows into. The blood flows are summarized as:

$$\begin{aligned}
Q_{LV \text{ to aorta}} &= \begin{cases} \frac{P_{LV} - P_{aorta}}{R_{aorta}} & \text{when } P_{LV} \geq P_{aorta} \\ (P_{LV} - P_{aorta})G_{AV} & \text{otherwise} \end{cases} \\
Q_{aorta \text{ to arteries}} &= \frac{P_{aorta} - P_{arteries}}{R_{arteries}} \\
Q_{arteries \text{ to arterioles}} &= \frac{P_{arteries} - P_{arterioles}}{R_{arterioles}} \\
Q_{arterioles \text{ to capillaries}} &= \frac{P_{arterioles} - P_{capillaries}}{R_{capillaries}} \\
Q_{capillaries \text{ to venules}} &= \frac{P_{capillaries} - P_{venules}}{R_{venules}} \\
Q_{venules \text{ to veins}} &= \frac{P_{venules} - P_{veins}}{R_{veins}} \\
Q_{veins \text{ to LV}} &= \begin{cases} \frac{P_{veins} - P_{LV}}{R_{LV}} & \text{when } P_{veins} \geq P_{LV} \\ (P_{veins} - P_{LV})G_{MV} & \text{otherwise} \end{cases} \quad (2.2)
\end{aligned}$$

where  $G_{AV}$  and  $G_{MV}$  are model parameters controlling the leakage through the aortic and mitral valves, respectively. The blood pressure within each compartment, except the LV, was associated with the compartment's compliance and its stressed blood volume, which is given by the difference between the instantaneous blood volume and the slack blood volume:

$$P_i = \frac{V_i(t) - V_{i,slack}}{C_i} \quad (2.3)$$

where  $V_i(t)$ ,  $V_{i,slack}$  and  $C_i$  are the instantaneous blood volume, the slack volume, and the compliance of compartment  $i$ , respectively. The LV pressure, on the other hand, was calculated from the FE model according to  $V_{LV}$  as the input. More details about this are provided in the finite element formulation section below.

### 2.2.3 LV model geometry

The geometry of a human LV was modeled using an ideal ellipsoidal shape with ~1280 quadratic tetrahedral elements. The slack chamber volume of LV was 66 ml with myocardium volume of 136 ml. The length of LV from base to apex was roughly 7 cm while the outer diameter of LV at base was 7.1 cm, As shown in Figure 2.2, myofiber directions  $f_\theta$  were defined by linearly changing the helix angle from  $60^\circ$  at the endocardium to  $-60^\circ$  at the epicardium transmurally across the wall using a Laplace-Dirichlet rule-based algorithm [142]. The sheet angles were assumed to align with the radial direction.

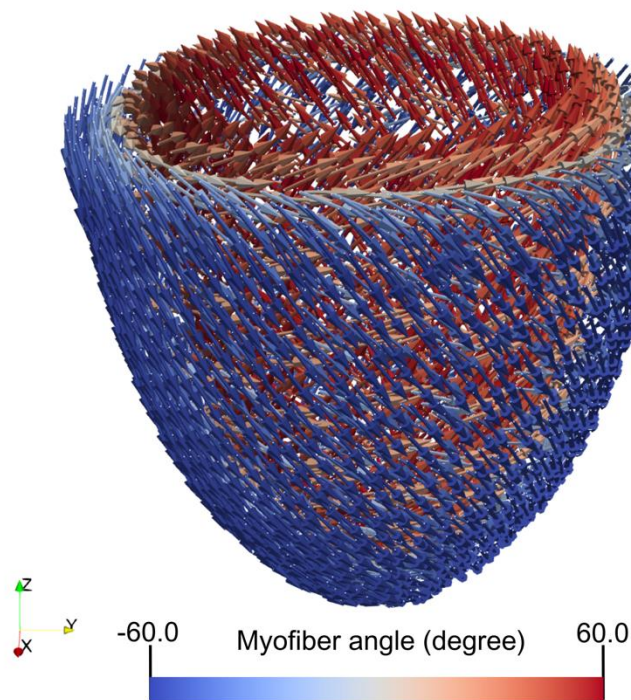


*Figure 2.2 Myofiber orientation with a linear transmural variation from  $60^\circ$  at the endocardium to  $-60^\circ$  at the epicardium.*

## 2.2.4 Cardiac electrophysiology

A simplified two compartment model of electrophysiology was used to increase the speed of the calculations. Specifically, the rates of change of the  $\text{Ca}^{2+}$  concentrations in the sarcoplasmic reticulum ( $Ca_{SR}$ ) and the myofilament space ( $Ca_{myo}$ ) were given by:

$$\frac{dCa_{SR}(t)}{dt} = k_{SERCA} Ca_{myo}(t) - (k_{leak} + A(t)k_{act}) Ca_{SR}(t) \quad (2.4)$$

$$\frac{dCa_{myo}(t)}{dt} = -\frac{dCa_{SR}(t)}{dt} \quad (2.5)$$

where the total  $\text{Ca}^{2+}$  concentration inside the cell  $Ca_{total} = Ca_{SR} + Ca_{myo}$  was kept constant,  $k_{SERCA}$  set the rate at which  $\text{Ca}^{2+}$  is pumped into the sarcoplasmic reticulum,  $k_{leak}$  defines a continual leak of  $\text{Ca}^{2+}$  into the myofilament space, and  $k_{act}$  controls the release of  $\text{Ca}^{2+}$  when the ryanodine receptors are open.  $A(t)$  is a pulse wave that is zero except for brief periods of duration  $t_{open}$  when  $A(t)$  is equal to one. These openings are initiated by the pacing stimuli that occur at time-intervals of  $t_{RR}$  and thus determine heart rate. This set of ODEs were solved at each integration point to drive the required  $\text{Ca}^{2+}$  transient for contraction of half-sarcomeres across the LV geometry.

## 2.2.5 Finite element formulation

The solution for LV mechanics was approximated using an implicit backward Euler scheme for numerical time-integration with a fixed time step of 1 ms. This was done using an open-source FE library called FEniCS [143]. The FE formulation of the LV mechanics problem was described by minimizing the following Lagrangian functional:

$$\begin{aligned}
\mathcal{L}(\mathbf{u}, p, P_{LV}, c_x, c_y, c_z) = & \int_{\Omega_0} W(\mathbf{u}) dV - \int_{\Omega_0} p(J-1) dV - \\
& P_{LV}(V_{LV}(\mathbf{u}) - V_{LV}) - c_x \cdot \int_{\Omega_0} u_x dV - \\
& c_y \cdot \int_{\Omega_0} u_y dV - c_z \cdot \int_{\Omega_0} \mathbf{z} \times \mathbf{u} dV
\end{aligned} \tag{2.6}$$

where  $\mathbf{z}$  is the longitudinal axis from apex-to-base,  $\mathbf{x}$  and  $\mathbf{y}$  are orthogonal axes to the  $\mathbf{z}$ -axis,  $\mathbf{u}$  is the displacement field,  $W$  is the total strain energy of the myocardium,  $p$  is a Lagrange multiplier to govern incompressibility of the tissue by enforcing the Jacobian of the deformation gradient tensor  $J=1$ ,  $P_{LV}$  is a Lagrange multiplier to constrain the LV cavity volume  $V_{LV}(\mathbf{u})$  to the prescribed value of  $V_{LV}$  (which is computed from the circulatory model),  $c_x$  and  $c_y$  are Lagrange multipliers to constrain the rigid body translation in the  $\mathbf{x}$  and  $\mathbf{y}$  directions, and  $c_z$  is a Lagrange multiplier to constrain the rigid body rotation. Finally, the relation between the LV cavity volume and the displacement field was given by equation (2.7) where  $\Omega_{k,endo}$  is the volume enclosed by the endocardial surface  $\Gamma_{k,endo}$  and the basal surface at  $\mathbf{z} = 0$ , and  $\mathbf{n}$  is the outward unit normal vector.

$$V_{LV}(\mathbf{u}) = \int_{\Omega_{k,endo}} dv = -\frac{1}{3} \int_{\Gamma_{k,endo}} \mathbf{x} \cdot \mathbf{n} da \tag{2.7}$$

where  $\mathbf{x}$  is the position vector relative to the original of the global coordinate system. The weak formulation of the mechanics problem then was obtained by taking the first variation of the Lagrangian functional:

$$\begin{aligned}
\delta\mathcal{L}(\mathbf{u}, p, P_{LV}, c_x, c_y, c_z) &= \int_{\Omega_0} \mathbf{F}\mathbf{S} : \nabla \delta\mathbf{u} dV - \int_{\Omega_0} (p\mathbf{J}\mathbf{F}^{-T} : \nabla \delta\mathbf{u} - \delta p(J-1)) dV - \\
P_{LV} \int_{\Omega_0} \mathbf{J}\mathbf{F}^{-T} : \nabla \delta\mathbf{u} dV - \delta P_{LV} (V_{LV}(\mathbf{u}) - V_{LV}) - \delta c_x \cdot \int_{\Omega_0} u_x dV - c_x \cdot \int_{\Omega_0} \delta u_x dV - \\
\delta c_y \cdot \int_{\Omega_0} u_y dV - c_y \cdot \int_{\Omega_0} \delta u_y dV - \delta c_z \cdot \int_{\Omega_0} \mathbf{z} \times \mathbf{u} dV - c_z \cdot \int_{\Omega_0} \mathbf{z} \times \delta\mathbf{u} dV &= 0
\end{aligned} \quad (2.8)$$

where  $\mathbf{F}$  is the deformation gradient tensor,  $\mathbf{S}$  is the 2<sup>nd</sup> Piola Kirchhoff stress tensor,  $\delta\mathbf{u} \in H^1(\Omega_0)$ ,  $\delta p \in L^2(\Omega_0)$ ,  $\delta P_{LV} \in R$ ,  $\delta c_x \in R$ ,  $\delta c_y \in R$ , and  $\delta c_z \in R$  are test functions corresponding to  $\mathbf{u}$ ,  $p$ ,  $P_{LV}$ ,  $c_x$ ,  $c_y$ , and  $c_z$ , respectively. In this formulation, the displacement field  $\mathbf{u}$  was approximated using quadratic interpolation functions, whereas linear functions were used for the Lagrange multiplier  $p$ .

## 2.2.6 Cardiac mechanics

The mechanical behavior of the LV was prescribed such that the 2<sup>nd</sup> Piola Kirchhoff stress tensor was additively decomposed into an active  $\mathbf{S}_a$  and a passive  $\mathbf{S}_p$  component, i.e.

$$\mathbf{S} = \mathbf{S}_a + \mathbf{S}_p \quad (2.9)$$

The myocardial tissue was modeled to be incompressible, hyperelastic, and transversely isotropic. The passive component of the stress tensor was further decomposed into three responses. This is due to incompressibility and the force-reliant nature of the active stress, which necessitates that the passive stress be decomposed into parts that account for the myofibers and remaining bulk tissue. Each response was obtained by differentiating a strain energy function with respect to Green-Lagrangian strain tensor,  $\mathbf{E}$ :

$$\mathbf{S}_p = \mathbf{S}_{vol} + \mathbf{S}_{bulk} + \mathbf{S}_{myofiber} = \frac{\partial\psi_{vol}}{\partial\mathbf{E}} + \frac{\partial\psi_{bulk}}{\partial\mathbf{E}} + \frac{\partial\psi_{myofiber}}{\partial\mathbf{E}} \quad (2.10)$$

In the above formulation, the function  $\psi_{vol} = -p(J-1)$  enforces the incompressibility of the tissue by a Lagrange multiplier  $p$ . The function  $\psi_{bulk}$  defines the response of the bulk tissue, which is described by a transversely isotropic Fung-type strain energy function [144]:

$$\psi_{bulk} = \frac{C}{2}(\mathbf{e}^Q - 1) \quad (2.11)$$

with  $Q = b_{ff}E_{ff}^2 + b_{xx}(E_{ss}^2 + E_{nn}^2 + E_{sn}^2 + E_{ns}^2) + b_{fs}(E_{fs}^2 + E_{sf}^2 + E_{fn}^2 + E_{nf}^2)$

where  $C$ ,  $b_{ff}$ ,  $b_{xx}$ , and  $b_{fs}$  are passive material parameters of the bulk tissue. Components of the Green-Lagrangian strain tensor  $\mathbf{E}$  are denoted by  $E_{ij}$  with  $(i, j) \in (f, s, n)$ , where  $f$ ,  $s$ , and  $n$  describe the fiber, sheet, and sheer-normal directions, respectively. Finally,  $\psi_{myofiber}$  prescribes the exponential strain energy function of the myofiber [145] which is given by:

$$\psi_{myofiber} = \begin{cases} C_1 \left( \mathbf{e}^{C_2(\alpha-1)^2} - 1 \right) & \alpha > 1 \\ 0 & \alpha \leq 1 \end{cases} \quad (2.12)$$

where  $C_1$ ,  $C_2$  are material parameters,  $\alpha$  is the myofiber stretch calculated as  $\alpha = \sqrt{\mathbf{f}_0 \cdot \mathbf{C} \cdot \mathbf{f}_0}$ , and  $\mathbf{C} = \mathbf{F}^T \mathbf{F}$  is the right Cauchy-Green deformation tensor.

The active stress component  $\mathbf{S}_a$  was driven by the MyoSim framework [97], which represents the mechanical properties of dynamically-coupled myofilaments of a half-sarcomere at each integration point across the LV mesh. As shown in Figure 2.3, binding sites on the thin filament transition between an inactive state named  $N_{off}$  (which is not available for myosin heads to attach) and an active state named  $N_{on}$  (which is available for myosin head binding). The activated binding sites are divided into two configurations named  $N_{unbound}$  (which is not bound to myosin heads) and  $N_{bound}$  (which is attached to

myosin heads and cannot be switch back to the  $N_{off}$  state). The flux for transition of binding sites from  $N_{off}$  to  $N_{on}$  is governed by:

$$J_{on} = k_{on} [Ca^{2+}] (N_{overlap} - N_{on}) \left( 1 + k_{coop} \left( \frac{N_{on}}{N_{overlap}} \right) \right) \quad (2.13)$$

where  $N_{on}$  is the fraction of binding sites in the active state,  $k_{on}$  is a rate constant,  $N_{overlap}$  is the fraction of binding sites that are in the range of myosin heads,  $k_{coop}$  is a constant factor that governs the cooperativity of the thin filament.

The activated unbound sites then turn into the off state via the  $J_{off}$  flux with a rate constant of  $k_{off}$ :

$$J_{off} = k_{off} (N_{on} - N_{bound}) \left( 1 + k_{coop} \left( \frac{N_{overlap} - N_{on}}{N_{overlap}} \right) \right) \quad (2.14)$$

On the thick filament, myosin heads can switch between three states, namely  $M_{SRX}$  (detached super-relaxed),  $M_{DRX}$  (detached disorder-relaxed), and  $M_{FG}$  (attached force generating). The transition fluxes between  $M_{SRX}$  and  $M_{DRX}$  are obtained via  $J_1$  and  $J_2$ :

$$\begin{aligned} J_1 &= k_1 (1 + k_{force} F_{total}) M_{SRX} \\ J_2 &= k_2 M_{DRX} \end{aligned} \quad (2.15)$$

where  $k_1$  and  $k_2$  are rate constants,  $k_{force}$  is a parameter with units of  $N^{-1}m^2$ ,  $F_{total} = F_{active} + F_{passive}$  is the total stress in the myofiber, and  $M_{SRX}$  and  $M_{DRX}$  are the fraction of myosin heads in the SRX and DRX states, respectively.

Myosin heads then attach to binding sites through  $J_3$  and detach via  $J_4$ :



$$\begin{aligned}
J_3(x) &= k_3 e^{\frac{-k_{cb}x^2}{2k_B T}} (N_{on} - N_{bound}) M_{SRX} \\
J_4(x) &= (k_{4,0} + k_{4,1}x^4) M_{FG}(x)
\end{aligned}
\tag{2.16}$$

where  $k_3$  and  $k_{4,0}$  are rate constants,  $k_{cb}$  is the stiffness of the cross-bridge link,  $k_B$  is Boltzmann's constant ( $1.38 \times 10^{-23} JK^{-1}$ ),  $T$  is the temperature in Kelvin,  $k_{4,1}$  is a parameter that sets the strain dependence of the cross-bridge detachment rate,  $M_{FG}$  is the fraction of myosin heads in the attached state, and  $x$  is the length to which the myosin heads are stretched.

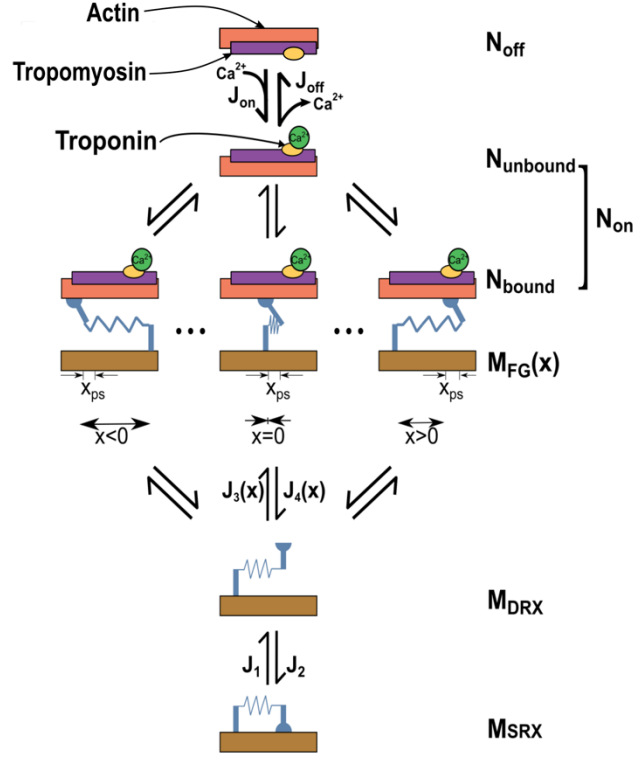


**Figure 2.3 Kinetic scheme.**

Sites on the thin filament switch between states that are available ( $N_{on}$ ) and unavailable ( $N_{off}$ ) for cross-bridges to bind to. Myosin heads transition between a super-relaxed detached state ( $M_{SRX}$ ), a disordered-relaxed detached state ( $M_{DRX}$ ), and a single attached force-generating state ( $M_{FG}$ ).  $J$  terms indicate fluxes between different states. Adapted from Sharifi et al. [1].

The fraction of myosin heads and binding sites at each configuration shown in Figure 2.3 are driven by a system of ODEs, given as:

$$\begin{aligned}
 \frac{dN_{off}}{dt} &= -J_{on} + J_{off} \\
 \frac{dN_{on}}{dt} &= J_{on} - J_{off} \\
 \frac{dM_{SRX}}{dt} &= -J_1 + J_2 \\
 \frac{dM_{DRX}}{dt} &= \left( J_1 + \sum_{i=1}^n J_{4,x_i} \right) - \left( J_2 + \sum_{i=1}^n J_{3,x_i} \right) \\
 \frac{dM_{FG,i}}{dt} &= J_{3,x_i} - J_{4,x_i} \text{ where } i = 1 \dots n
 \end{aligned} \tag{2.17}$$

The above ODEs were evaluated with 1nm resolution over the range of  $-10 \leq x \leq 10$  nm, resulting in  $n=21$ . This leads to a total number of 25 ODEs to be solved at each integration point across the geometry of LV. Calculations were initiated with all binding sites in the  $N_{off}$  configuration and all myosin heads in the  $M_{SRX}$  state.

The active stress experienced by a myofiber is given by:

$$\mathbf{F}_{active} = N_0 \mathbf{k}_{cb} \sum_{i=1}^n \mathbf{M}_{FG,i}(\mathbf{x}_i + \mathbf{x}_{ps}) \quad (2.18)$$

where  $N_0$  is the density of myosin heads (set to  $6.9 \times 10^{16} \text{ m}^{-2}$ ) [98] and  $x_{ps}$  is the power-stroke of an attached cross-bridge.

Finally, the active stress tensor is defined as:

$$\mathbf{S}_a = \mathbf{F}_{active} \mathbf{f}_0 \otimes \mathbf{f}_0 \quad (2.19)$$

### 2.2.7 Baroreflex

The normalized afferent signal  $B_a$  that mimics the output of the baroreceptors was driven via a sigmoidal relationship with arterial pressure ( $P_{arteries}$ ).

$$B_a(t) = \frac{1}{1 + e^{-S(P_{arteries}(t) - P_{set})}} \quad (2.20)$$

where  $P_{set}$  is the setpoint for arterial pressure and  $S$  defines the slope of the function around its midpoint.

In the present model, intricate processes related to sympathetic and parasympathetic drive have been simplified through the implementation of a single balance signal  $B_b$ , along with  $5k+3$  unique control signals ( $B_{c,1}, B_{c,2} \dots B_{c,5k+3}$ ), and  $5k+3$  distinct mapping functions ( $M_1, M_2 \dots M_{5k+3}$ ), where  $k$  represents the number of integration points present across the LV mesh. These control signals and mapping functions operate to

modulate crucial physiological processes, including heart rate,  $\text{Ca}^{2+}$  transients, myofilament function, and vascular tone. Further detailed explanation of this process is provided below.

The balance signal  $B_b$  is a normalized representation of the difference between sympathetic and parasympathetic efferent activity. Its rate of change was defined as

$$\frac{dB_b(t)}{dt} = \begin{cases} -k_{drive}(B_a(t)-0.5)B_b(t) & B_a \geq 0.5 \\ -k_{drive}(B_a(t)-0.5)(1-B_b(t)) & B_a < 0.5 \end{cases} \quad (2.21)$$

where  $k_{drive}$  is a rate constant. The equations described above lead to a  $B_b$  balance signal that converges to unity if the sympathetic drive dominates the control loop. Alternatively, when the parasympathetic drive has greater influence, the balance signal  $B_b$  approaches to zero. The speed at which the control signal responds to changes in arterial pressure and  $P_{set}$  is governed by the value assigned to the  $k_{drive}$  parameter.

The normalized control signals  $B_{c,i}$  describe how each of the reflex-sensitive parameters in the cardiovascular model respond to the balance signal. Similar to equation (2.22), their rates of change were defined as

$$\frac{dB_{c,i}(t)}{dt} = \begin{cases} k_{control,i}(B_b(t)-0.5)(1-B_{c,i}(t)) & B_b \geq 0.5 \\ k_{control,i}(B_b(t)-0.5)B_{c,i}(t) & B_b < 0.5 \end{cases} \quad (2.22)$$

where  $i$  ranges from 1 to  $5k+3$  and  $k_{control,i}$  is the rate constant for system  $i$ . Each signal tends to converge to a value of unity when sympathetic drive exceeds parasympathetic drive, ( $B_b > 0.5$ ). Conversely, if parasympathetic drive predominates ( $B_b < 0.5$ ) the control signals gradually diminish towards zero.

The final step in the algorithm used mapping functions  $M_i$  to link the normalized control signals  $B_{c,i}$  to actual parameter values. Each mapping function took the form

$$M_i(B_{c,i}(t)) = \begin{cases} M_{base,i} + \frac{1}{2}(B_{c,i}(t) - 0.5)(M_{symp,i} - M_{base,i}) & B_{c,i} \geq 0.5 \\ M_{base,i} + \frac{1}{2}(B_{c,i}(t) - 0.5)(M_{para,i} - M_{base,i}) & B_{c,i} < 0.5 \end{cases} \quad (2.23)$$

where  $M_{base,i}$  is the default value for parameter  $i$ , and  $M_{symp,i}$  and  $M_{para,i}$  are its limits during maximum sympathetic and maximum parasympathetic drive, respectively. Table 2.1 shows the mapping relationships.

**Table 2.1 Baroreflex implementation functions.**

	Function	Controlled parameters	Increased arterial pressure ...
Chronotropism	$M_1$	$t_{RR}$	Lengthens inter-beat interval and slows heart rate
Vascular tone	$M_2, M_3$	$R_{arterioles}$ and $C_{veins}$	Reduces systemic afterload and increases venous compliance
Calcium handling	$M_4 \cdots M_{k+3}$	$k_{SERCA}$	Reduces the amplitude and prolongs the duration of $Ca^{2+}$ transients at each integration point
	$M_{k+4} \cdots M_{2k+3}$	$k_{act}$	
Sarcomere contractility	$M_{2k+4} \cdots M_{3k+3}$	$k_1$	Reduces myosin cycling and sensitizes the thin filaments at each integration point
	$M_{3k+4} \cdots M_{4k+3}$	$k_3$	
	$M_{4k+4} \cdots M_{5k+3}$	$k_{on}$	

### 2.2.7.1 Chronotropism

The implementation of baroreflex control of heart rate in this study involved a mapping of the  $M_1$  signal to the inter-beat interval,  $t_{RR}$ . In order to maintain heart rate within a physiologically appropriate range, upper and lower limits ( $M_{symp,1}$  and  $M_{para,1}$ ,

respectively) were set at 0.33 seconds and 1.5 seconds. This corresponded to a heart rate range of 40 to 180 beats per minute.

### 2.2.7.2 Vascular tone

In this study, the  $M_2$  and  $M_3$  signals were set to modulate the arteriolar resistance ( $R_{arterioles}$ ) and venous compliance ( $C_{veins}$ ), respectively. In vivo, an increase in arterial pressure is associated with a decrease in arteriolar resistance and an increase in venous compliance. These physiological effects are consistent with a reduction in afterload and preload, and reflect the operation of a negative feedback loop. By modulating the resistance and compliance of the arterioles and veins, the baroreflex control system helps to regulate blood pressure and maintain cardiovascular homeostasis.

### 2.2.7.3 Cell-level contractility

To modulate cell-level contractility, five parameters were adjusted at each integration point in this study. Specifically,  $M_4 \dots M_{k+3}$ , and  $M_{k+4} \dots M_{2k+3}$ , were mapped to  $k_{act}$  and  $k_{SERCA}$  in equation (2.4) for all integration points, respectively. To achieve the desired effect of decreased contractility with increased arterial pressure, limits were placed on these parameters.

$M_{2k+4} \dots M_{5k+3}$  were designed to modulate the  $k_1$ ,  $k_3$  and  $k_{on}$  parameters in the MyoSim framework [98, 121] over all integration points. The  $k_1$  parameter controls the rate of transition of myosin heads from the SRX to the DRX state [146], while  $k_3$  controls the transition of myosin heads from the DRX state to the FG state. The  $k_{on}$  parameter, on the other hand, is the second-order rate constant for  $Ca^{2+}$  activation of binding sites on actin. Limits were placed on these parameters (as outlined in APPENDICES

APPENDIX 1. FILE S1) to reflect the effect of increased arterial pressure on contractile force. Specifically, increased arterial pressure was found to bias myosin heads towards the DRX and FG states, while desensitizing the thin filament to  $\text{Ca}^{2+}$ . These changes mimic some of the effects produced by increased phosphorylation of myosin regulatory light chain and troponin I [147, 148].

For the sake of simplicity in the current simulations, the base value ( $M_{base,i}$ ), maximum sympathetic ( $M_{symp,i}$ ), and maximum parasympathetic ( $M_{para,i}$ ) values for each of the five parameters  $k_{act}$ ,  $k_{SERCA}$ ,  $k_1$ ,  $k_3$  and  $k_{on}$  were assumed identical across all integration points. However, since they can be controlled independently at each integration point, it is possible to have spatial variation in these parameters. For example, if the  $\text{Ca}^{2+}$  dynamics are altered in a local region, those parameters could be assigned distinct values relative to the rest of the mesh.

## 2.3 Results

### 2.3.1 Response to changes in user-defined arterial pressure setpoints

Figure 2.4 illustrates how the implemented reflex algorithm controls arterial pressure at user-defined setpoints. The simulation was initialized, with the reflex algorithm deactivated, using default parameters until it reached steady state ( $\sim 5$  cardiac cycles) with an arterial pressure range of  $\sim 126/84$  mmHg. The baroreflex was activated at 5 s (shown by the first vertical dashed line in each plot). Since the mean value of  $B_a$  was greater than 0.5, the balance signal  $B_b$  started to decrease and subsequently decreased  $B_{c,i}$  and  $M_i$ . This led to a decrease in heart rate, intracellular  $\text{Ca}^{2+}$  handling, myofilament contractility and vascular tone. These changes in reflex-sensitive parameters reduced arterial pressure to its  $P_{set}$  value of 90 mmHg, which corresponded to a range of  $\sim 112/68$  mmHg.

Between the second and third vertical dashed lines  $P_{set}$  was linearly increased from 90 mmHg to 120 mmHg. This change induced a system-level response that increased  $B_{c,i}$  and  $M_i$  and consequently increased the arterial pressure range to  $\sim 141/98$  mmHg via increasing heart rate, intracellular  $\text{Ca}^{2+}$  transient, myofilament contractility, and vascular tone. Figure S 1 depicts how the reflex-sensitive parameters related to myofilament contractility were spatially adjusted across the geometry to account for the increase in  $P_{set}$ .



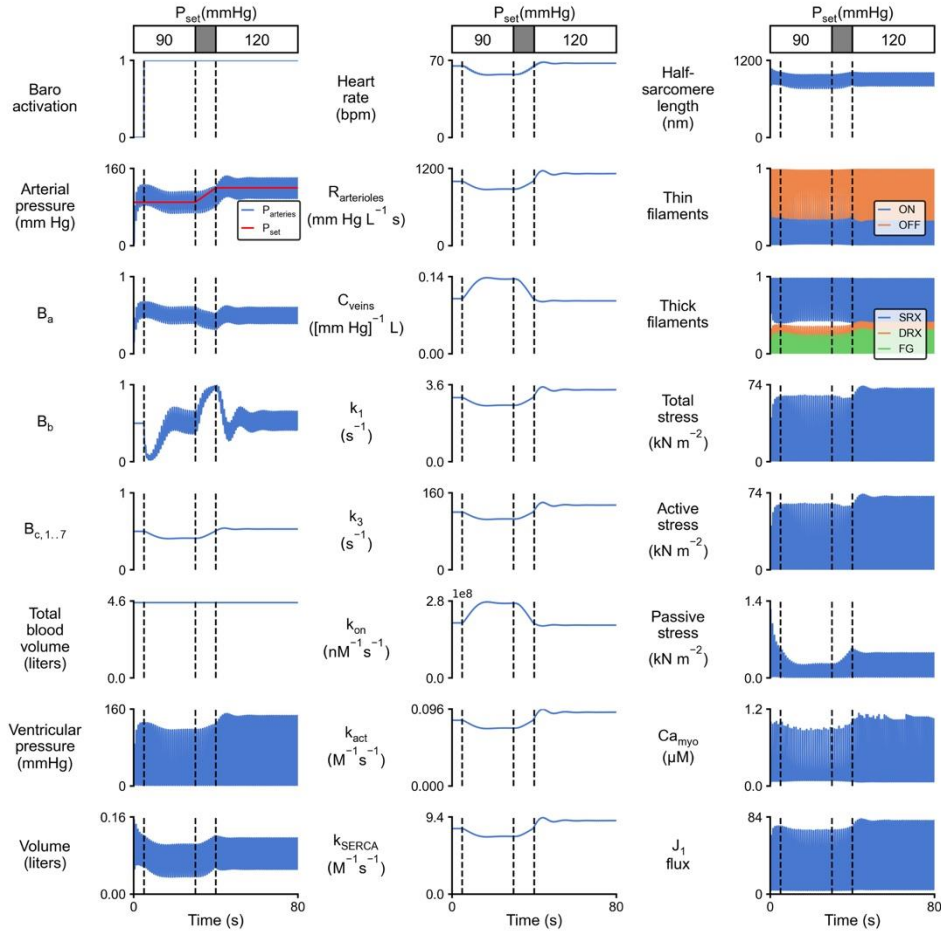


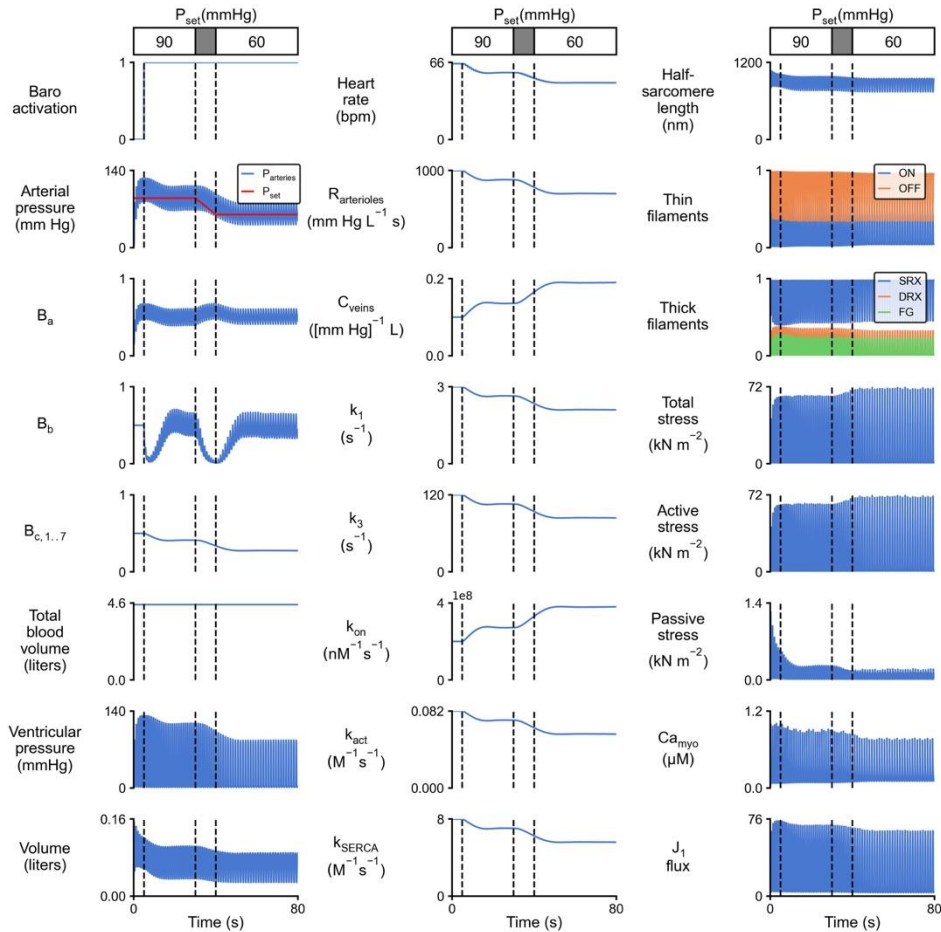
**Figure 2.4 Simulation demonstrating baroreflex control of arterial pressure for increasing  $P_{set}$  by 30 mmHg.**

The left-hand column shows baroreflex signals along with four other system-level properties. The middle column shows the 8 reflex sensitive parameters. The right-hand column shows properties relevant to myocardial function that are averaged over the entire mesh. The simulation started using default parameters. The baroreflex was initiated after 5 s (first vertical line on each plot). The baroreflex setpoint was increased from 90 to 120 mmHg over a 10 s period (between second and third vertical line). The OFF and ON labels describe the status of binding sites on the thin filament. The SRX, DRX, and FG labels refer to myosin heads in the super-relaxed, disordered-relaxed, and force-generating states, respectively.

Figure 2.5 shows how the model responds to a decrease of  $P_{set}$ . Similar to Figure 2.4, the simulation was initialized with default parameters and then the baroreflex was activated to regulate arterial pressure at  $P_{set}$  of 90 mmHg. Between second and third vertical dashed lines  $P_{set}$  decreased from 90 mmHg to 60 mmHg. In response to this change,

the baroreflex decreased  $B_{c,i}$  and  $M_i$  to down regulate the arterial pressure by decreasing heart rate,  $\text{Ca}^{2+}$  transient, myofilament contractility, and vascular tone. Furthermore, Figure S 2 shows how the spatial parameters related to myofilament contractility were adjusted to regulate arterial pressure for a  $P_{set}$  value of 60 mmHg.

In summary, Figure 2.4 and Figure 2.5 illustrate how the implemented reflex algorithm can adjust system-level properties to regulate arterial pressure at different setpoints.



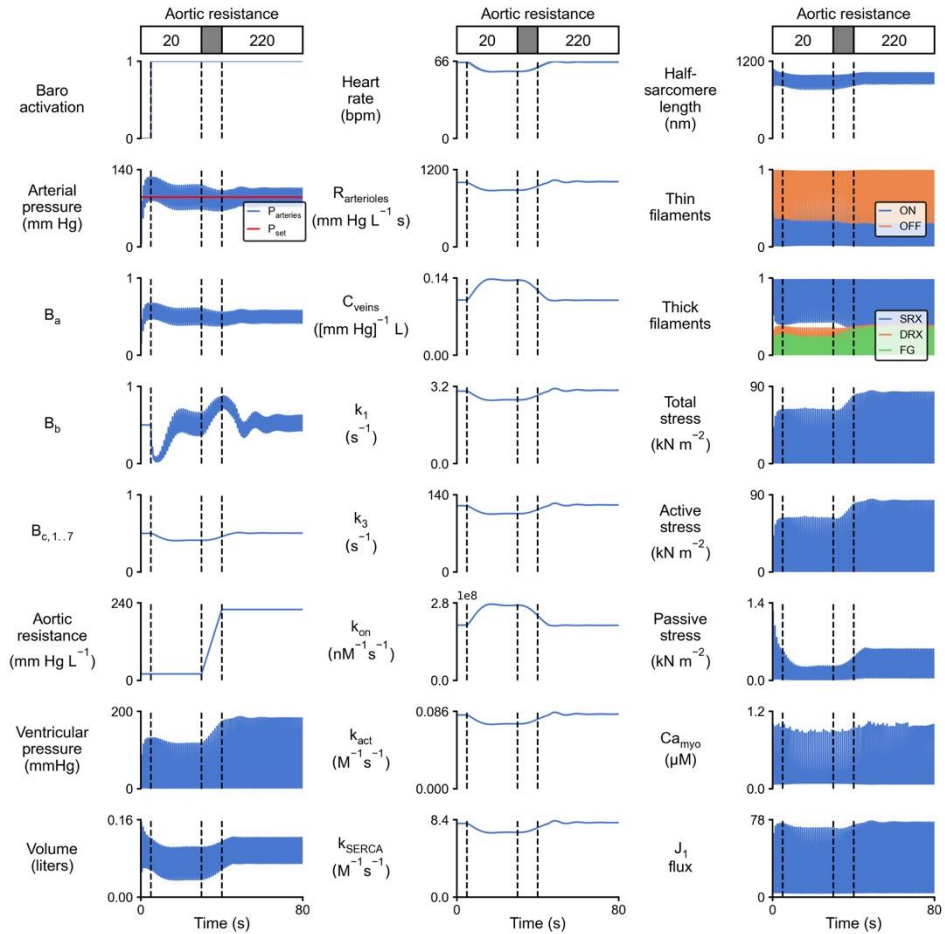
**Figure 2.5 Simulation demonstrating baroreflex control of arterial pressure for decreasing  $P_{set}$  by 30 mmHg.**

Figure panels are arranged as in Figure 2.4. The simulation started using default parameters. The baroreflex was initiated after 5 s (first vertical line on each plot). The baroreflex setpoint was decreased from 90 to 60 mmHg over a 10 s period (between second and third vertical line).

### 2.3.2 Response to acute increase in aortic resistance

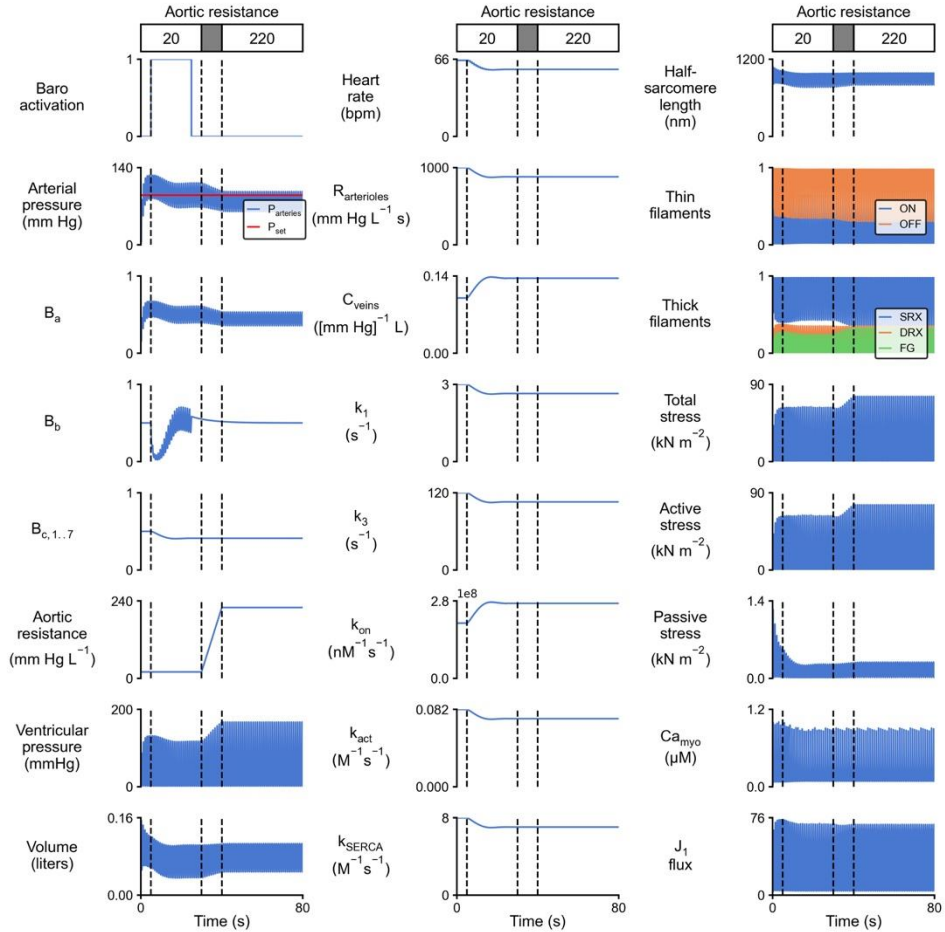
Figure 2.6 demonstrates the response of the baroreflex to an acute increase in aortic resistance (between second and third vertical dashed lines). Increasing the aortic resistance elevated the pressure gradient between the LV and aorta, which led to an increase in afterload. This perturbation slowed down the shortening of myofilaments and thus reduced the stroke volume and arterial pressure. The activated baroreflex restored arterial pressure

by increasing the  $B_{c,i}$  control signals, which resulted in a higher heart rate,  $\text{Ca}^{2+}$  transient, myofilament contractility (Figure S 1 in APPENDIX 4. SUPPLEMENTARY FIGURES) and vascular tone.



**Figure 2.6** The baroreflex stabilizes arterial pressure when aortic resistance is acutely increased. Figure panels are arranged as in Figure 2.4 except that aortic resistance parameter is shown in place of total blood volume. The simulation started using default parameters. The baroreflex activated after 5 s (first vertical line on each plot). Aortic resistance was increased from 20 to 220 mmHg L<sup>-1</sup> s over a 10 s period (between second and third vertical lines on each plot).

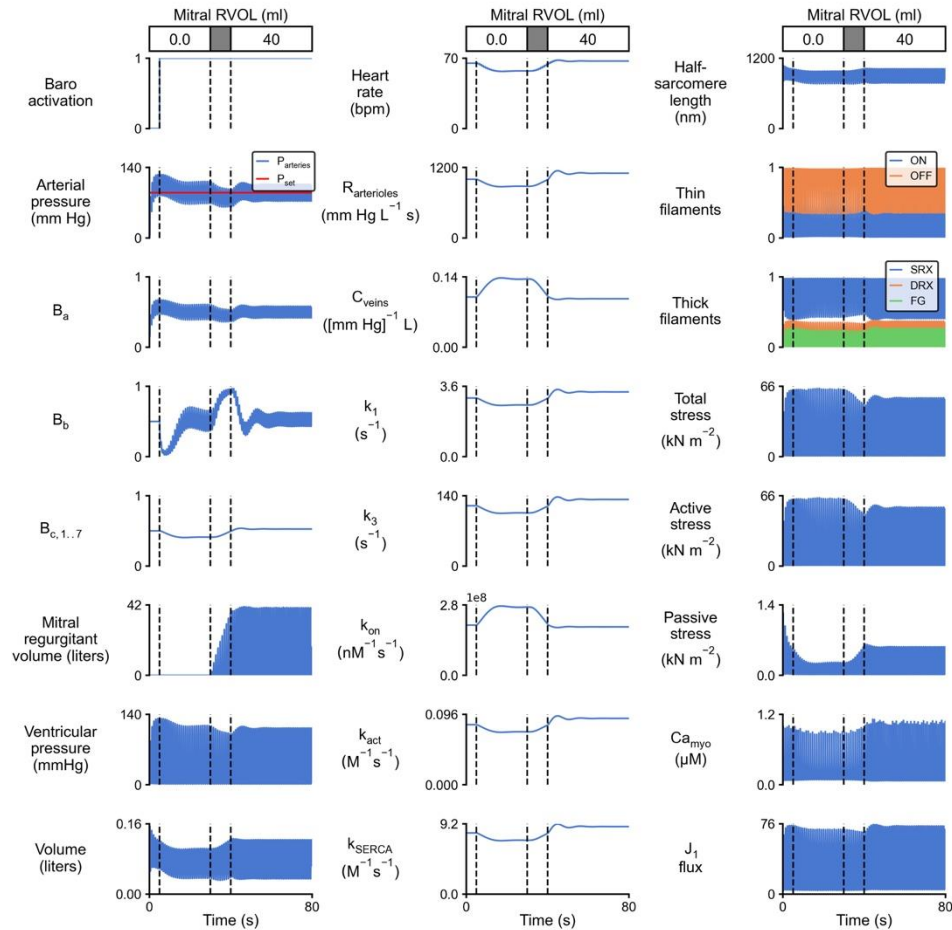
Figure 2.7 shows how arterial pressure drops in the absence the baroreflex. Although the peak active stress increased due to the change in afterload, the passive stress and end-diastolic volume (preload) remained unchanged.



**Figure 2.7** The model cannot maintain arterial pressure without baroreflex when aortic resistance is acutely increased. Figure panels are arranged as in Figure 2.6. Note that the baroreflex was deactivated before applying the perturbation.

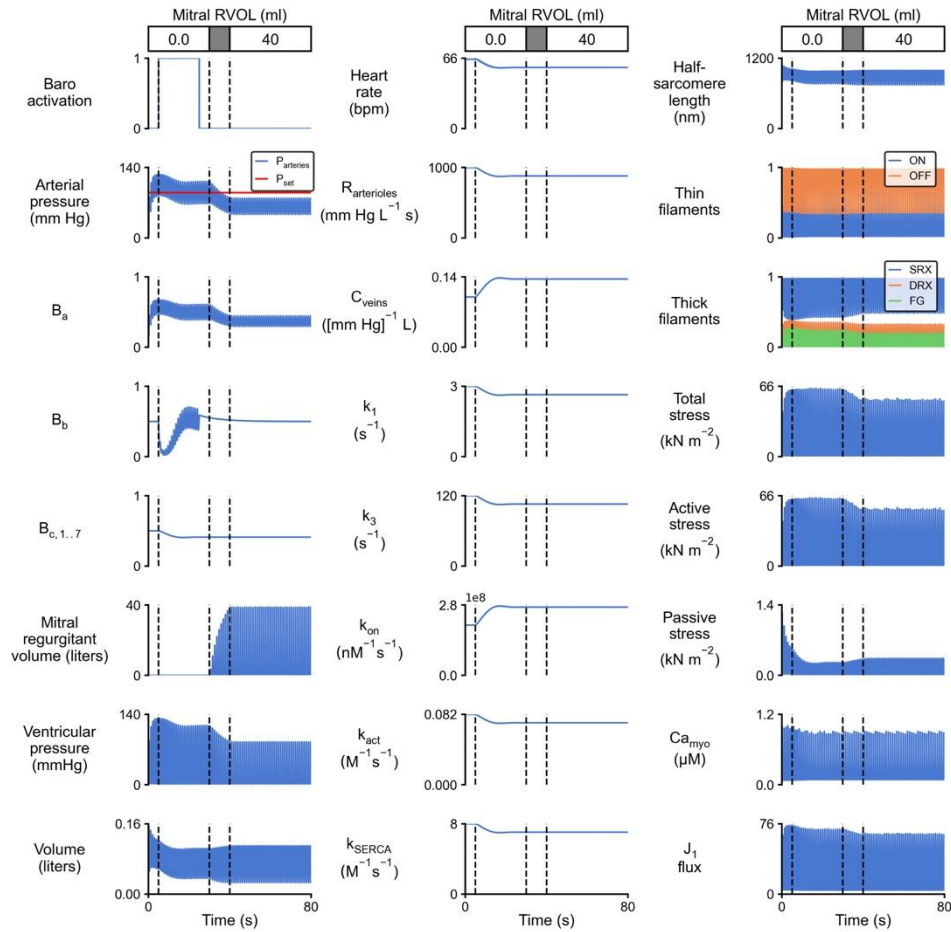
### 2.3.3 Response to acute mitral regurgitation

Figure 2.8 shows the model response when acute mitral regurgitation is induced. In the case below, a mild level of regurgitant volume was prescribed according to American Heart Association guideline [149]. By allowing the blood to flow back through the mitral valve, the forward stroke volume decreased and thus afterload, in particular, and arterial pressure started to fall. The change in arterial pressure was detected by the baroreflex algorithm, since  $B_a$  deviated from its normal level of 0.5. The control system responded to this change in received afferent signal and started to increase heart rate, intracellular  $\text{Ca}^{2+}$ , contractility of myofilaments (Figure S 4), and constricting of vessels to recover arterial pressure.



**Figure 2.8** The baroreflex stabilizes arterial pressure when acute mitral regurgitation is induced. Figure panels are arranged as in Figure 2.4 except that mitral regurgitant volume is shown in place of total blood volume. The simulation started using default parameters. The baroreflex activated after 5 s (first vertical line on each plot). Model parameter  $G_{MV}$  in equation (2.1) was increased from 0 to 0.002 over a 10 s period (between second and third vertical lines on each plot) that resulted in  $\sim 40$  ml of regurgitant volume.

In a similar simulation the baroreflex was deactivated before perturbing the mitral valve. The regurgitant volume led the arterial pressure to drop significantly from  $\sim 111/67$  mmHg, when the system was at steady state before applying the perturbation, to  $\sim 79/47$  mmHg at the final steady state (Figure 2.9). In addition to the drop in active stress, the passive stress and end-diastolic volume (preload) remained unchanged.



**Figure 2.9** The model cannot maintain arterial pressure without baroreflex when mitral regurgitation is induced.

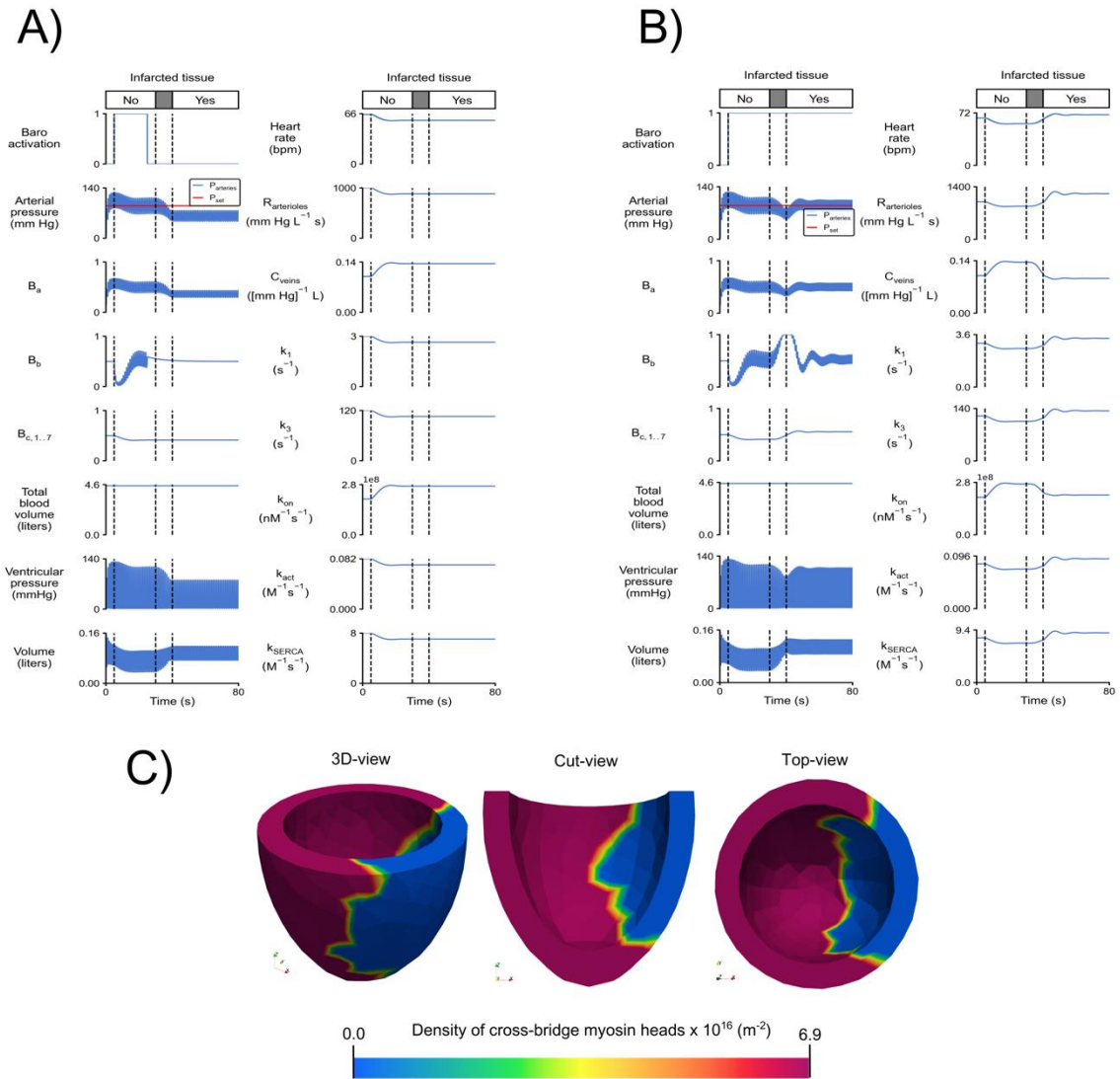
Figure panels are arranged as in Figure 2.4 except that mitral regurgitant volume is shown in place of total blood volume. The simulation started using default parameters. The baroreflex activated after 5 s (first vertical line on each plot) and deactivated after 15 s. Model parameter  $G_{MV}$  in equation (2.1) was increased from 0 to 0.003 during 10 s (between second and third vertical lines on each plot) to result in the same regurgitant volume as the case shown in Figure 2.8.

### 2.3.4 Response to acute myocardial infarction

In another model, the response of the baroreflex was tested by simulating acute myocardial infarction. Similar to the preceding sections, the simulation was initialized using default parameters and then the baroreflex was activated to regulate arterial pressure for a  $P_{set}$  of 90 mmHg. An additional simulation was run with the baroreflex deactivated



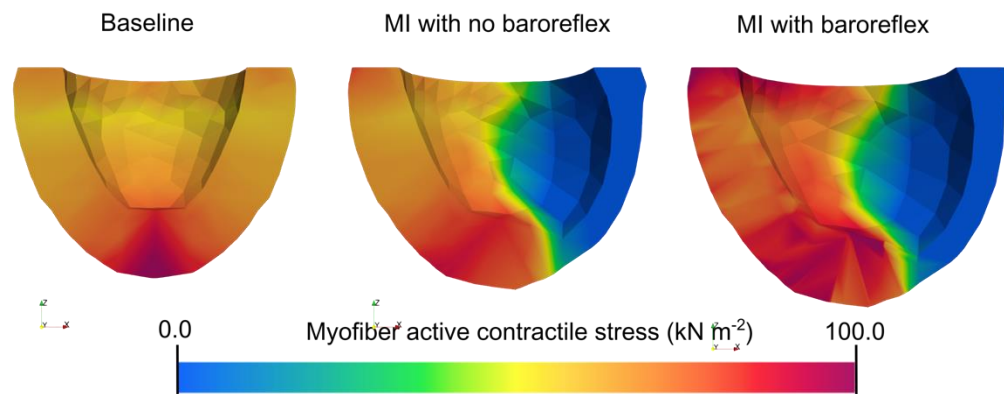
before the perturbation. Cardiomyocyte deterioration in the infarcted region was mimicked by reducing the density of cross-bridge myosin heads to zero (Figure 2.10.C), thus eliminating contractility. It should be noted that the border zone was not modeled in this simulation, since it usually forms as a result of the long-term effects of MI. (Figure 2.10.A) shows that without the baroreflex, arterial pressure drops significantly from  $\sim 112/68$  mmHg to  $\sim 77/47$  mmHg due to the loss of contractile function. However, the model with the baroreflex was able to maintain arterial pressure by increasing heart rate, intracellular  $\text{Ca}^{2+}$  transient, vascular tone (Figure 2.10.B) and adaptation of contractile function in the remote region (Figure 2.11).



**Figure 2.10 Simulation of acute myocardial infarction.**

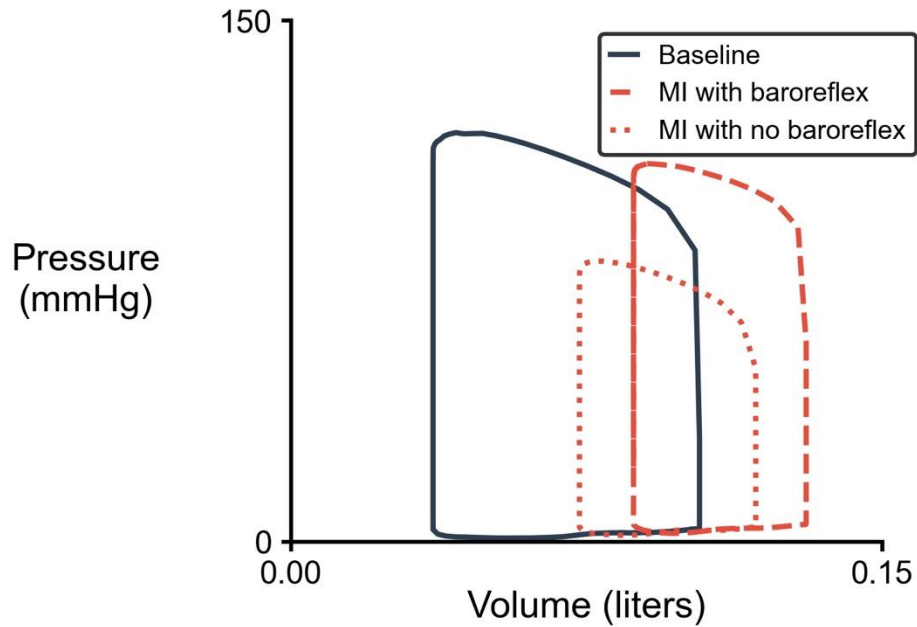
*A) without baroreflex control of arterial pressure and (b) with baroreflex control of arterial pressure by (c) reducing the density of cross-bridge myosin heads to zero in the infarcted region. The multi panel figures in (a) and (b) are arranged as in Figure 2.6 except showing only the left-hand and middle columns. The simulation started using default parameters and the baroreflex activated at 5 s. For (a), the baroreflex was deactivated once the system reached to steady state before mimicking MI. Density of cross-bridge myosin heads reduced to zero in the infarcted region over a 10 s period (between second and third vertical lines on each plot). Note: The yellow region in (c) is due to interpolation of cross-bridge density values over the mesh in Paraview and not a border zone region.*

Figure 2.11 demonstrates the peak active stress that was generated by myofibers across the LV chamber for three different cases. The infarcted tissue generated no contractile active stress for both MI cases. Regarding the remote regions, it can be seen that the reflex-activated case generated higher active stress to maintain arterial pressure at the  $P_{set}$  value of 90 mmHg. However, in an equivalent simulation with no baroreflex, the remote region generated the same magnitude of contractile stress as the baseline case.



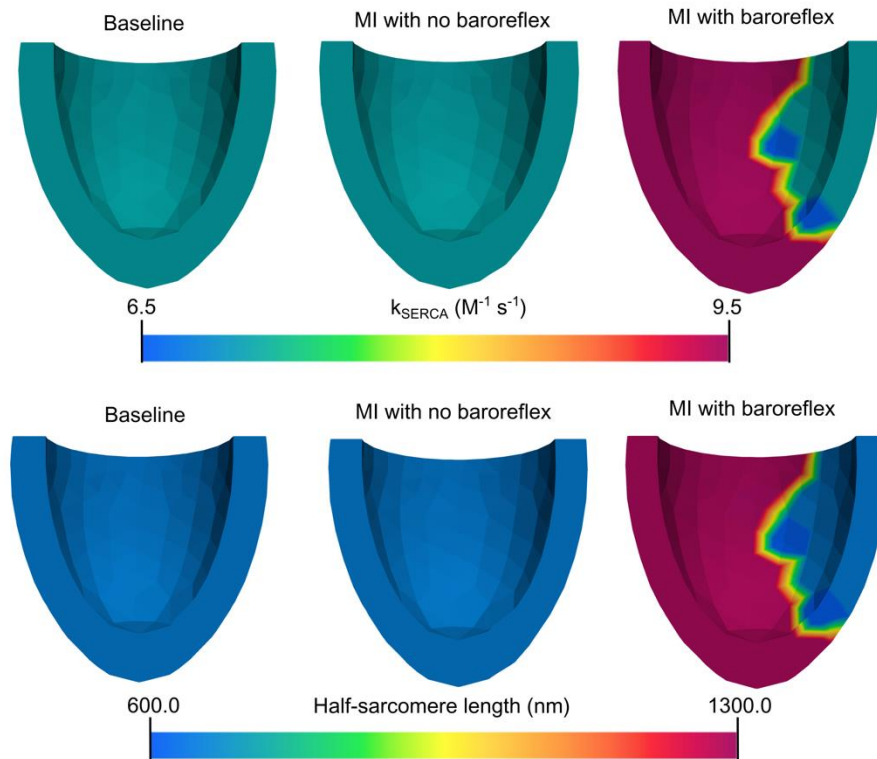
**Figure 2.11 Myofiber active contractile stress increased in the remote region in the model with baroreflex control of arterial pressure.**  
*Infarcted region could not generate any active stress, since as all myosin heads were deactivated.*

Figure 2.12 compares the predicted pressure-volume (PV) loops for the MI cases against the baseline case. For both MI cases the end-diastolic volume increased and ejection fraction reduced. The end-systolic pressure-volume relationship (ESPVR) for both MI cases fell below the baseline case as the PV loops shifted rightward, but for the MI case without the baroreflex it reduced more. Accordingly, the peak pressure for the case without the baroreflex dropped significantly below the baseline value. However, the peak pressure remained within the range of the baseline value for the baroreflex case.



**Figure 2.12 Pressure-volume loop shifted rightward for MI simulations compared to baseline.**

Figure 2.13 and Figure 2.14 demonstrate the distribution of the reflex-sensitive parameters over the LV chamber for the intracellular  $\text{Ca}^{2+}$  transient and myofilament contractility, respectively. It can be seen that these parameters were not adjusted in the infarcted tissue for either of the MI cases, and thus match the baseline value. However, the baroreflex-activated case adjusted these parameters for the remote region to maintain arterial pressure at a setpoint of 90 mmHg.



**Figure 2.13** Baroreflex regulation of thin filament parameters related to intracellular  $Ca^{2+}$  transient before and after mimicking acute myocardial infarction. Baroreflex could not regulate the parameters in the infarcted region.

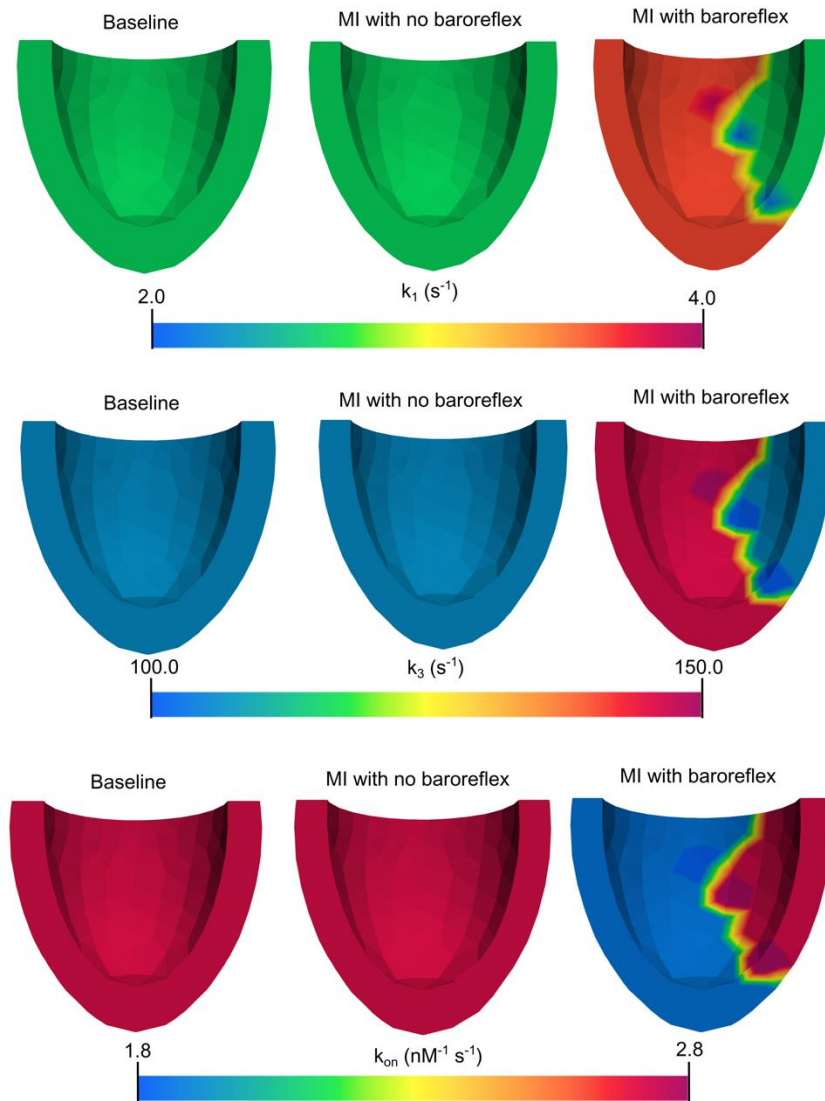


**Figure 2.14** Baroreflex regulation of thick filament parameters related to myofibril contractility before and after mimicking acute myocardial infarction. Baroreflex could not regulate the parameters in the infarcted region.

## 2.4 Discussion

The approach described in the current study incorporated a 3D FE model of the left ventricle with a model of the cardiovascular system, which also integrated a compensatory baroreflex to control arterial pressure by regulating heart rate, intracellular  $\text{Ca}^{2+}$  handling, myofilament function, and vascular tone. Although this work was not intended to develop a sophisticated model of the baroreflex loop, it was shown that the implementation can capture key aspects of the underlying physiology to preserve arterial pressure. The main goal of this study was to show that the algorithm could not only regulate arterial pressure at different user-defined setpoints, but it could also preserve pressure when the system was exposed to different perturbations, including acute cases of aortic stenosis, mitral regurgitation, and myocardial infarction. Of additional note is the response of the model with and without the baroreflex, as described below.

In the case of acute aortic stenosis without the baroreflex, the mean arterial pressure dropped below the set-point (Figure 2.7). However, it has been shown in animal experiments of acute aortic banding that the mean arterial pressure is maintained at the homeostatic level [150]. In the model that included the baroreflex, the end-diastolic volume (EDV) and end-systolic volume (ESV) increased, leading to increases in both passive and active stress (Figure 2.6). This also led to a rightward shift of the PV loop, as well as an increase in peak pressure in the LV, which matches the results seen in a previous study of acute aortic banding [151]. However, the model without the baroreflex showed no change in EDV and only a slight change in ESV (Figure 2.7). Therefore, the model without the baroreflex is unable to capture key elements of the physiological response to acute increases in aortic resistance.

For the model of acute mitral regurgitation without the baroreflex, the mean arterial pressure also dropped below the set-point (Figure 2.9). But, in animal experiments of mild mitral insufficiency, which was acutely induced with a percutaneous valve spreader, the mean arterial pressure was nearly maintained for a cohort of 7 dogs [152]. In the model that included the baroreflex loop the EDV increased, as well as the stroke volume (Figure 2.8). This increase in preload is consistent with observations related to acute regurgitation caused by papillary or chordae rupture in the LV [153]. However, the EDV did not change in the model that ignored the baroreflex (Figure 2.9). Thus, the model without the baroreflex cannot capture key elements of the response to acute mitral regurgitation.

In the model of acute myocardial infarction without the baroreflex, the mean arterial pressure also decreased, but with a larger magnitude compared to the other cases above (Figure 2.10.A). This decrease in arterial pressure is in conflict with a previous animal study of acute myocardial infarction, which used a rapidly expanding cuff to ligate the circumflex coronary artery [154]. As reported in that study, the mean arterial pressure was maintained, while heart rate increased, which is in agreement with the current model that includes the baroreflex (Figure 2.10.B). Additionally, end-diastolic pressure and volume increased, while the peak systolic pressure was minimally impacted, which is also in agreement with the model that includes the baroreflex (Figure 2.10.B). Finally, the PV loop shifted rightward (Figure 2.12), which is consistent with acute myocardial infarction [155]. Although the model that does not account for the baroreflex shifted slightly to the right, the drop in peak systolic pressure and the fixed heartrate do not match the previously reported experimental findings. Therefore, the model without the baroreflex is unable to capture key aspects of the physiological response to acute myocardial infarction.



Furthermore, the remote myocardium away from the MI adapts its contractile properties to compensate for the loss of contractile function in the affected area [156-158]. *In vivo*, compensatory reflexes preserve arterial pressure by increasing heart rate, contractility of surviving myocardium, and vascular tone [159]. The current model with the baroreflex exhibited this behavior, as seen by the increase in contractile force in the remote myocardium (Figure 2.11) and the increase in heart rate and vascular tone (Figure 2.10.A). Studying this type of adaptation process is challenging, as most compensatory responses, such as changes in myofilament contractility, are difficult to measure non-invasively. Therefore, a multiscale model of cardiovascular function that incorporates the effects of compensatory reflexes to preserve arterial pressure can provide insights for better understanding the adaptation process post-MI.

The baroreflex is an important regulatory mechanism that plays a key role in controlling the loading of the LV. As a result, it can influence secondary mechanisms such as cardiac growth and remodeling, which are closely associated with changes in LV loading. This has been observed in computational models of cardiac growth, which use simplified representations of the LV [1]. In our recent review paper, we noted that the absence of a baroreflex model resulted in mismatches between predicted and experimentally measured values of hemodynamics in simulations of LV growth [63, 73]. Several early studies have highlighted the significance of the baroreflex in predicting the prognosis of heart failure and cardiac death post-MI. For instance, La Rovere et al. [160] demonstrated that individuals with depressed baroreflex sensitivity were at a higher risk of subsequent mortality following myocardial infarction. In particular, it has been suggested that a reduced baroreflex sensitivity indicates an impaired vagal efferent component of the

baroreflex, which is associated with heart rate variability and an increased incidence of arrhythmic deaths [161]. In a later study, La Rovere et al. [162] found that the analysis of baroreflex sensitivity in post-MI patients can serve as a prognostic metric independent of left ventricular ejection fraction in predicting cardiac mortality.

Recent studies have further examined the role of the reflex response post-MI by observing the variability in global LV growth and remodeling for individual patients with moderately sized infarcts. Witzenburg and Holmes [159] hypothesized that such variability in reflex response could explain this phenomenon. In their study, they used a previously published computational model of LV growth and demonstrated that variability in reflex components could result in variability in the degree of predicted LV dilation. Therefore, they proposed that post-infarction reflex compensation could be a target for LV remodeling therapies [163]. However, in their subsequent work [164], they suggested that customizing pharmacological therapy based on the initial acute response of the baroreflex could be challenging.

The development of accurate cardiovascular models is essential for understanding and predicting the pathophysiology of cardiovascular diseases, as well as evaluating the efficacy of potential treatments. Among the key components of such models is the FE model of the LV, which allows for 3D representation of spatially varying quantities, such as mechanical behavior or reflex response. The current study advances the field by developing of a novel approach to FE modeling, which directly controls molecular-level contractility via the baroreflex control algorithm. This algorithm modulates four key parameters that define the magnitude and time-course of intracellular calcium transients, as well as the function of the thick and thin myofilaments. Compared to existing

cardiovascular models that rely on phenomenological relationships, the direct control of molecular-level contractility represents a significant advancement [110, 165, 166]. Additionally, the 3D representation of the LV geometry allows for spatially heterogeneous control of the reflex-sensitive parameters, which is not possible with 1D models of the LV [64, 73, 138]. This approach could provide a more detailed understanding of the underlying mechanisms governing cardiac function and enable future studies aimed at a more accurate assessment of how various pharmaceuticals and genetic modifications to calcium-handling proteins and/or sarcomeric proteins affect the baroreflex.

## **2.5 Limitations**

Several of the limitations in the current work related to the baroreflex model are shared with our prior work [138], which provides additional detail. One example is that the baroreflex algorithm employed in this work is simplified, in that it does not receive dual input from both the parasympathetic and sympathetic nerves. Rather, this is represented by a single Bb balance signal. This approach restricts the ability to adjust single reflex effectors independently of the others, but this limitation will be addressed in future work.

An additional limitation of the current model is its inability to capture long-term ventricular growth and remodeling following an acute MI or valvular disease perturbations. Although the current model successfully captures the short-term adaptation in hemodynamics and ventricular function, it does not account for the changes in ventricular geometry, fiber orientation, and mechanical properties that occur at later time points after disease onset. Ultimately, the remodeling process culminates in organ-level changes such as left ventricular dilation and wall thinning, or eccentric hypertrophy. To model long-term

ventricular growth and remodeling, new feedback loops must be added that alter the myocardial mass and orientation of myofibers in response to changes in stimulus signals such as myofiber stress or strain. However, given the goal of this study, modeling such long-term changes falls beyond its scope, but will be a major focus of future investigations specifically aimed at growth and remodeling.

## **2.6 Summary and Conclusion**

This study presents a novel open-source model of cardiovascular function, named MyoFE, which uses finite element modeling to simulate left ventricular mechanics to pump blood into the systemic circulation. The model incorporates a baroreflex algorithm that can control arterial pressure by modulating several parameters, including heart rate, intracellular  $\text{Ca}^{2+}$  handling, myofilament contractility, and vascular tone. The results of this study demonstrate that the implemented algorithm can not only regulate arterial pressure at various user-defined setpoints, but can also maintain it when the system is exposed to perturbations such as acute aortic stenosis, mitral regurgitation, and myocardial infarction. This suggests that the MyoFE model may prove useful in studying the mechanisms underlying short-term regulation of arterial pressure and the effects of various cardiovascular disorders on the system. Future work will focus on integrating cardiac growth and remodeling with the baroreflex response.

### 3.1 Introduction

The heart is able to adapt its shape and size in response to pathological conditions, such as altered ventricular loading from valvular disease. This process is referred to as cardiac growth and remodeling [16, 18]. Based on the ventricular geometry, there are two conventional types of growth. Concentric growth is defined by wall thickening and an increase in ventricular mass, due to the deposition of sarcomeres in parallel, with little or no change in the internal size of the ventricular chamber [6]. Eccentric growth reflects the addition of sarcomeres in series, which dilates the chamber and increases wall mass with minimal change in wall thickness [6]. In general, cardiac growth initiates as an early adaptive response to valvular diseases, but it can progress to heart failure if the underlying cause is left unresolved [2, 6, 17].

Computer based models are providing new insights on the progression of cardiac growth and remodeling. Despite numerous studies that have developed mathematical formulations to represent these phenomena, the choice of driving stimulus for these growth laws is still up for debate. Conventionally, computational models of cardiac growth have utilized either myofiber stress [58, 59], strain [62-64], or some combination of the two [66, 167] as their driving signal. However, several of these models either neglect the contractile behavior of the LV [41, 51, 56, 59, 66], or use non-mechanistic models of contraction that might be missing key elements that are needed in simulations of LV growth [1]. For

instance, several groups have employed a phenomenological Hill-type model of contraction to simulate the LV during systole [63, 65, 68, 86], which defines the magnitude of active force using a length-dependent force generation model [87, 88]. Other studies [64, 74] have used a time-varying elastance model of the ventricle [89, 90] to simulate the full cardiac cycle, which assumes an exponential end-diastolic pressure-volume relationship and a linear end-systolic pressure-volume relationship. In recent studies by Rondanina and Bovendeerd [40, 73], they investigated the effects of different mechanical stimuli on cardiac growth while the contractile behavior of the ventricle was modeled by a one-fiber model of cardiac function [91]. This model was essentially used to relate mechanics at the organ level, via ventricular pressure and volume, to mechanics at the tissue level, via myofiber stress and sarcomere length. In general, these contractile models do not simulate the sliding of myofilaments based on the Huxley crossbridge formation [96] at the myosin level.

Though previous models have shown promising results, the underlying mechanisms that drive growth are complex and are accompanied by perturbations at the molecular level. Emerging evidence has linked titin to fundamental signaling pathways, such as those regulating protein quality control, hypertrophic gene expression, and stress sensing. Titin can thus be viewed as a crucial integrating element at the intersection of myocyte signaling. The mechanical and mechano-signaling functions of the titin springs are variably tuned in health and disease, particularly in the heart by altering passive stiffness through titin-isoform switching, protein phosphorylation, and hypertrophic signaling. In heart muscle, titin is expressed in two main isoforms: the N2B-isoform, which contains a short, stiff spring segment, and (variable) N2BA-isoforms, which contain longer

springs and thus are more compliant [168]. Titin is a long protein that spans from the Z disk to M line with an elastic structure within the I band. This elastic behavior of titin within the I-band plays an essential role in generating passive stiffness of the sarcomere, which store strain-energy during diastolic filling and recoil during systole. Thus, increased passive stress could be linked to the eccentric growth induced by titin mediated stress sensing.

In pioneering work, Davis et al. [169] developed an innovative model that integrated mechanics and molecular signaling. They postulated that the aspect ratio of myocytes was related to MEK1-ERK signaling, with myocytes becoming wider with increasing values of the contractile force-time integral. This induced MEK1-ERK, which regulates cell cycle progression, to mediate concentric growth in their model. They also suggested that ventricular mass was regulated by calcineurin signaling, which increased if the force-time integral deviated (in either direction) from a homeostatic setpoint. These elegant assumptions allowed Davis et al.'s model to reproduce the different magnitudes of concentric and eccentric growth measured in several strains of genetically-modified mice. Therefore, the time course of stress throughout the cardiac cycle could be used as the stimulus for growth and remodeling.

The present study was developed based on this general hypothesis. Accordingly, the first step was to use a multiscale model of cardiovascular function named MyoFE so that the left ventricular contractile behavior is driven by a mechanistic model of half-sarcomere function, which simulates the sliding of myofilaments based on the Huxley crossbridge formation [96] in the myosin level. The second step was to extend this multiscale model of cardiovascular function so that the left ventricular geometry grows in

response to changes in biomechanical stimulus. In this study, concentric growth was driven by the time-averaged total stress (i.e., passive and active) along the myofiber direction over the cardiac cycle. Eccentric growth was driven by time-averaged passive intracellular myofiber stress over the cardiac cycle. Multiple simulations were then performed to investigate how the ventricle responded to changes in hemodynamic load associated with different types of valvular disease, which induce pressure or volume overload. The results of this study showed that the new framework could predict the correct form of LV growth in response to two forms of valvular disease, namely, aortic stenosis and mitral regurgitation. Additionally, the LV growth was reversed when the disease-mimicking perturbations were removed.

## **3.2 Methods**

### **3.2.1 Overview**

This chapter extends the central framework of MyoFE described in CHAPTER 2 by adding a growth algorithm (Figure 3.1). In the central framework, a pacing stimulus drives a simplified model of electrophysiology to compute the  $\text{Ca}^{2+}$  transient for calculation of contractile stress at the myosin-level. A 3D finite element model of the left ventricle then pumps blood into the systemic side of the circulatory system. More details on the central framework can be found in CHAPTER 2. In the following, we first describe the key aspects of the central framework. Then, the details related to the growth constitutive model and separation of timescales between the growth and elastic deformation are provided thereafter.



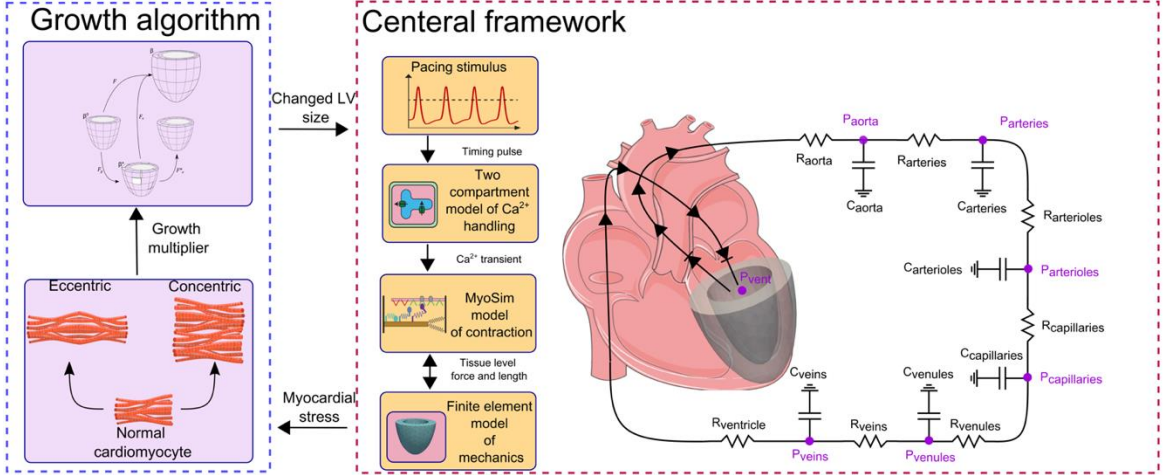


**Figure 3.1** Integration of the central framework of MyoFE with a growth algorithm.

### 3.2.2 Finite element formulation

The solution for LV mechanics was approximated using an implicit backward Euler scheme for numerical time-integration with a fixed time step of 1 ms. An open-source FE library called FEniCS [143] was used for this purpose. The FE formulation of the LV mechanics problem was prescribed by minimizing the following Lagrangian functional given below:

$$\begin{aligned}
 \mathcal{L}(\mathbf{u}, p, P_{LV}, c_x, c_y, c_z) = & \int_{\Omega_0} W(\mathbf{u}) dV - \int_{\Omega_0} p(J-1) dV - \\
 & P_{LV}(V_{LV}(\mathbf{u}) - V_{LV}) - c_x \cdot \int_{\Omega_0} u_x dV - \\
 & c_y \cdot \int_{\Omega_0} u_y dV - c_z \cdot \int_{\Omega_0} \mathbf{z} \times \mathbf{u} dV
 \end{aligned} \quad (3.1)$$

where  $\mathbf{z}$  is the longitudinal axis from apex-to-base,  $\mathbf{x}$  and  $\mathbf{y}$  are orthogonal axes to the  $\mathbf{z}$ -axis,  $\mathbf{u}$  is the displacement field,  $W$  is the total strain energy of the myocardium,  $p$  is a Lagrange multiplier to govern incompressibility of the tissue by enforcing the Jacobian of the deformation gradient tensor  $J = 1$ ,  $P_{LV}$  is a Lagrange multiplier to constrain the LV

cavity volume  $V_{LV}(\mathbf{u})$  to the prescribed value of  $V_{LV}$  (which is computed from the circulatory model),  $c_x$  and  $c_y$  are Lagrange multipliers to constrain the rigid body translation in the  $\mathbf{x}$  and  $\mathbf{y}$  directions, and  $c_z$  is a Lagrange multiplier to constrain the rigid body rotation. Finally, the relation between the LV cavity volume and the displacement field was given by equation (3.2) where  $\Omega_{k,endo}$  is the volume enclosed by the endocardial surface  $\Gamma_{k,endo}$  and the basal surface at  $\mathbf{z} = 0$ , and  $\mathbf{n}$  is the outward unit normal vector.

$$V_{LV}(\mathbf{u}) = \int_{\Omega_{k,endo}} dv = -\frac{1}{3} \int_{\Gamma_{k,endo}} \mathbf{x} \cdot \mathbf{n} da \quad (3.2)$$

where  $\mathbf{x}$  is the position vector relative to the original of the global coordinate system. The weak formulation of the mechanics problem then was obtained by taking the first variation of the Lagrangian functional described in equation (3.1):

$$\begin{aligned} \delta \mathcal{L}(\mathbf{u}, p, P_{LV}, c_x, c_y, c_z) &= \int_{\Omega_0} \mathbf{F} \mathbf{S} : \nabla \delta \mathbf{u} dV - \int_{\Omega_0} (p \mathbf{J} \mathbf{F}^{-T} : \nabla \delta \mathbf{u} - \delta p (J - 1)) dV - \\ P_{LV} \int_{\Omega_0} \mathbf{J} \mathbf{F}^{-T} : \nabla \delta \mathbf{u} dV - \delta P_{LV} (V_{LV}(\mathbf{u}) - V_{LV}) - \delta c_x \cdot \int_{\Omega_0} u_x dV - c_x \cdot \int_{\Omega_0} \delta u_x dV - \\ \delta c_y \cdot \int_{\Omega_0} u_y dV - c_y \cdot \int_{\Omega_0} \delta u_y dV - \delta c_z \cdot \int_{\Omega_0} \mathbf{z} \times \mathbf{u} dV - c_z \cdot \int_{\Omega_0} \mathbf{z} \times \delta \mathbf{u} dV &= 0 \end{aligned} \quad (3.3)$$

where  $\mathbf{F}$  is the deformation gradient tensor,  $\mathbf{S}$  is 2<sup>nd</sup> Piola Kirchhoff stress tensor,  $\delta \mathbf{u} \in H^1(\Omega_0)$ ,  $\delta p \in L^2(\Omega_0)$ ,  $\delta P_{LV} \in R$ ,  $\delta c_x \in R$ ,  $\delta c_y \in R$ , and  $\delta c_z \in R$  are test functions corresponding to  $\mathbf{u}$ ,  $p$ ,  $P_{LV}$ ,  $c_x$ ,  $c_y$ , and  $c_z$ , respectively. In this formulation, the displacement field  $\mathbf{u}$  was approximated using quadratic interpolation functions, whereas linear functions were used for the Lagrange multiplier  $p$ .

### 3.2.3 Cardiac mechanics

To define the LV mechanics, the 2<sup>nd</sup> Piola Kirchhoff stress tensor was additively decomposed into an active  $\mathbf{S}_a$  and a passive component  $\mathbf{S}_p$  i.e.

$$\mathbf{S} = \mathbf{S}_a + \mathbf{S}_p \quad (3.4)$$

The myocardium was modeled to be incompressible, hyperelastic, and transversely isotropic. The passive component of the stress tensor was further decomposed into three responses. This is due to incompressibility and the force-reliant nature of the active stress, which necessitates that the passive stress be decomposed into parts that account for the bulk tissue and the myofibers. Each response was obtained by differentiating a strain energy function with respect to Green-Lagrangian strain tensor,  $\mathbf{E}$ :

$$\mathbf{S}_p = \mathbf{S}_{vol} + \mathbf{S}_{bulk} + \mathbf{S}_{myofiber} = \frac{\partial \psi_{vol}}{\partial \mathbf{E}} + \frac{\partial \psi_{bulk}}{\partial \mathbf{E}} + \frac{\partial \psi_{myofiber}}{\partial \mathbf{E}} \quad (3.5)$$

In the above formulation, the function  $\psi_{vol} = -p(J-1)$  that enforces the incompressibility of tissue by a Lagrange multiplier  $p$ . The function  $\psi_{bulk}$  which defines the response of the bulk tissue is described by a transversely isotropic Fung-type strain energy function [144]:

$$\psi_{bulk} = \frac{C}{2} (e^Q - 1) \quad (3.6)$$

with  $Q = b_{ff} E_{ff}^2 + b_{xx} (E_{ss}^2 + E_{nn}^2 + E_{sn}^2 + E_{ns}^2) + b_{fs} (E_{fs}^2 + E_{sf}^2 + E_{fn}^2 + E_{nf}^2)$

where  $C$ ,  $b_{ff}$ ,  $b_{xx}$ , and  $b_{fs}$  are passive material parameters of the bulk tissue. Components of Green-Lagrangian strain tensor  $\mathbf{E}$  are denoted by  $E_{ij}$  with  $(i, j) \in (f, s, n)$ , where  $f$ ,  $s$ , and  $n$  describe the fiber, sheet, and shear-normal directions, respectively. Finally,  $\psi_{myofiber}$  prescribes the exponential strain energy function of the myofiber [145] which is given by:

$$\psi_{myofiber} = \begin{cases} C_1 \left( e^{C_2(\alpha-1)^2} - 1 \right) & \alpha > 1 \\ 0 & \alpha \leq 1 \end{cases} \quad (3.7)$$

where  $C_1$ ,  $C_2$  are material constants and  $\alpha$  is the myofiber stretch calculated as  $\alpha = \sqrt{\mathbf{f}_0 \cdot \mathbf{C} \cdot \mathbf{f}_0}$  and  $\mathbf{C} = \mathbf{F}^T \mathbf{F}$  is the right Cauchy-Green deformation tensor, and  $\mathbf{F}$  is deformation gradient tensor. Finally, using the active stress experienced by a myofiber calculated by MyoSim framework  $F_{active}$ , the active stress tensor can be described as:

$$\mathbf{S}_a = \mathbf{F}_{active} \mathbf{f}_0 \otimes \mathbf{f}_0 \quad (3.8)$$

More details on MyoSim framework are provided in CHAPTER 2.

### 3.2.4 Growth constitutive model

The growth algorithm in the current work is based on the volumetric growth theory by Roudriguez et al. [38]. According to this theory  $\mathbf{F}$  can be multiplicatively decomposed into an elastic component  $\mathbf{F}_e$  and incompatible growth  $\mathbf{F}_g$  component, i.e.

$$\mathbf{F} = \mathbf{F}_e \mathbf{F}_g \quad (3.9)$$

The growth deformation gradient tensor is further described as:

$$\mathbf{F}_g = \theta_{local, f_0} \mathbf{f}_0 \otimes \mathbf{f}_0 + \theta_{local, s_0} \mathbf{s}_0 \otimes \mathbf{s}_0 + \theta_{local, n_0} \mathbf{n}_0 \otimes \mathbf{n}_0 \quad (3.10)$$

where  $\theta_{local, f_0}$ ,  $\theta_{local, s_0}$ , and  $\theta_{local, n_0}$  are local scalar growth multipliers along the myofiber  $\mathbf{f}_0$ , sheet  $\mathbf{s}_0$ , and sheet-normal  $\mathbf{n}_0$  directions in the reference configuration, which control the magnitude of growth between consecutive growth steps. The rate of change in each local growth multiplier is prescribed as:

$$\frac{\partial \theta_{local,i}}{\partial t} = \begin{cases} \frac{1}{\tau_{fg,i}} \left( \frac{\theta_{max,i} - \theta_{global,i}}{\theta_{max,i} - \theta_{min,i}} \right) \frac{S_i - S_{setpoint,i}}{|S_{setpoint,i}|} & S_i - S_{setpoint} \geq 0 \\ \frac{1}{\tau_{rg,i}} \left( \frac{\theta_{global,i} - \theta_{min,i}}{\theta_{max,i} - \theta_{min,i}} \right) \frac{S_i - S_{setpoint}}{|S_{setpoint,i}|} & S_i - S_{setpoint} < 0 \end{cases} \quad (3.11)$$

where  $i$  denotes growth in the myofiber  $\mathbf{f}_0$ , sheet  $\mathbf{s}_0$ , and sheet-normal  $\mathbf{n}_0$  directions.  $\tau_{fg,i}$  and  $\tau_{rg,i}$  are rate time constants associated with forward growth and reverse growth in the  $i$  direction.  $S_i$  is the stimulus signal and  $S_{setpoint,i}$  is the homeostatic setpoint level of the stimulus signal, associated with growth along the  $i$  direction. It should be noted that the homeostatic level of the growth signal was established at each integration point in the mesh. This was accomplished by running a baseline simulation without any valvular perturbation.

In this study, the stimulus signal for eccentric growth along the myofiber direction  $\mathbf{f}_0$  was assumed to be the time-averaged myofiber passive stress over a cardiac cycle. This is defined as:

$$S_{f_0} = \frac{1}{T} \int_0^T \mathbf{f}_0 \cdot \mathbf{S}_{myofiber} \mathbf{f}_0 dt \quad (3.12)$$

where  $T$  is the period of one cardiac cycle. The stimulus signal for concentric growth in the cross-fiber directions ( $\mathbf{s}_0$  and  $\mathbf{n}_0$ ) was driven by the time-averaged total stress (passive and active) along the myofiber direction over a cardiac cycle. These signals are defined as:

$$S_{s_0} = S_{n_0} = \frac{1}{T} \int_0^T \mathbf{f}_0 \cdot \mathbf{S} \mathbf{f}_0 dt \quad (3.13)$$

Each  $S_{setpoint,i}$  value was established using the equations above during the baseline simulation of normal function. According to equation (3.11), local tissue growth is induced

when the stimulus signal is higher than its homeostatic setpoint level, while the myocardium shrinks when it falls below the setpoint level. Clearly, growth does not occur when the stimulus signal is equal to its homeostatic level.

$\theta_{global,i}$  is the global growth multiplier at each integration point that accounts for the total accumulation of growth in the direction  $i$ , relative to the initial reference configuration. These values are bounded between  $\theta_{max,i}$  and  $\theta_{min,i}$ , which reflect the maximum and minimum physiological tissue growth. In equation (3.11), as  $\theta_{global,i}$  tends towards  $\theta_{max,i}$  or  $\theta_{min,i}$  the rate of change in the local growth multiplier  $\frac{\partial \theta_{local,i}}{\partial t}$  tends to 0 and stops the myocardium from the excessive growth or shrinkage. To be clear, in the preceding descriptions the term local is meant to represent growth between two consecutive growth steps, whereas the term global represents the total accumulation of growth relative to the initial reference configuration. Additionally, growth occurs at each integration point in the mesh based on the established stimulus setpoint at that location. Model parameters utilized for one of the simulations in this study can be found in APPENDIX 2. FILE S2.

### 3.2.5 Separation of timescales between growth and elastic deformation

LV growth is a mechanism that takes place over a longer period of time, such as weeks and months. Therefore, in this study we separated the timescale of growth mechanics and normal elastic deformation as described previously [65, 68]. Based on this approach, the growth step occurs after a certain number of cardiac cycles, which can be set by the user. In the current study, the growth step occurred every 3 cardiac cycles. More specifically, normal elastic deformation was used during these cycles and then the growth step takes place at the very end of the 3<sup>rd</sup> cycle (as outlined in Figure 3.2). This allowed 2

cardiac cycles for the circulatory model to reach steady state, since the previous growth step alters the LV geometry. Then a 3<sup>rd</sup> cardiac cycle (step 0 in Figure 3.2), which is referred to as the “growth cycle”, is conducted for the assessment of the stimulus signal.

It can be seen that the growth step starts by calculating the associated time-averaged stimulus signal over the growth cycle (step 1 in Figure 3.2). Once the growth cycle reaches the end-diastolic volume, the LV geometry is unloaded back to its reference configuration (step 2 in Figure 3.2). In the next step, the local thetas ( $\theta_{local,i}$ ) are updated based on the growth stimulus (step 3 in Figure 3.2). With this approach, the growth tensor  $\mathbf{F}_g$  is referred to the most recent updated reference configuration, and correspondingly, its input parameters  $\theta_{local,i}$  were computed based on this updated configuration. Next, the LV geometry in the reference configuration grows, since  $\mathbf{F}_g$  is a non-identity tensor (step 4 in Figure 3.2). This is accomplished by solving for the elastic part of the deformation gradient  $\mathbf{F}_e$ , which is required to attain a compatible configuration in the absence of any loading on the LV (i.e., the endocardial surface is traction free). This results in a residually stressed unloaded configuration. However, in the current study we chose to alleviate this residual stress, similar to the “updated reference configuration approach” described in our previous work [65]. This was accomplished by updating the nodal positions of the reference configuration to match those of the nodes displaced during the growth step (step 5-1 in Figure 3.2). Once the updated reference configuration is established the global theta value is calculated (step 5-2 in Figure 3.2). Finally, the new reference configuration for the LV geometry is reload back to the prescribed end-diastolic volume (step 6 in Figure 3.2), which

conserves total blood volume in the system, and continues the normal elastic deformation until the next growth cycle (i.e.  $n+1$ ) starts.

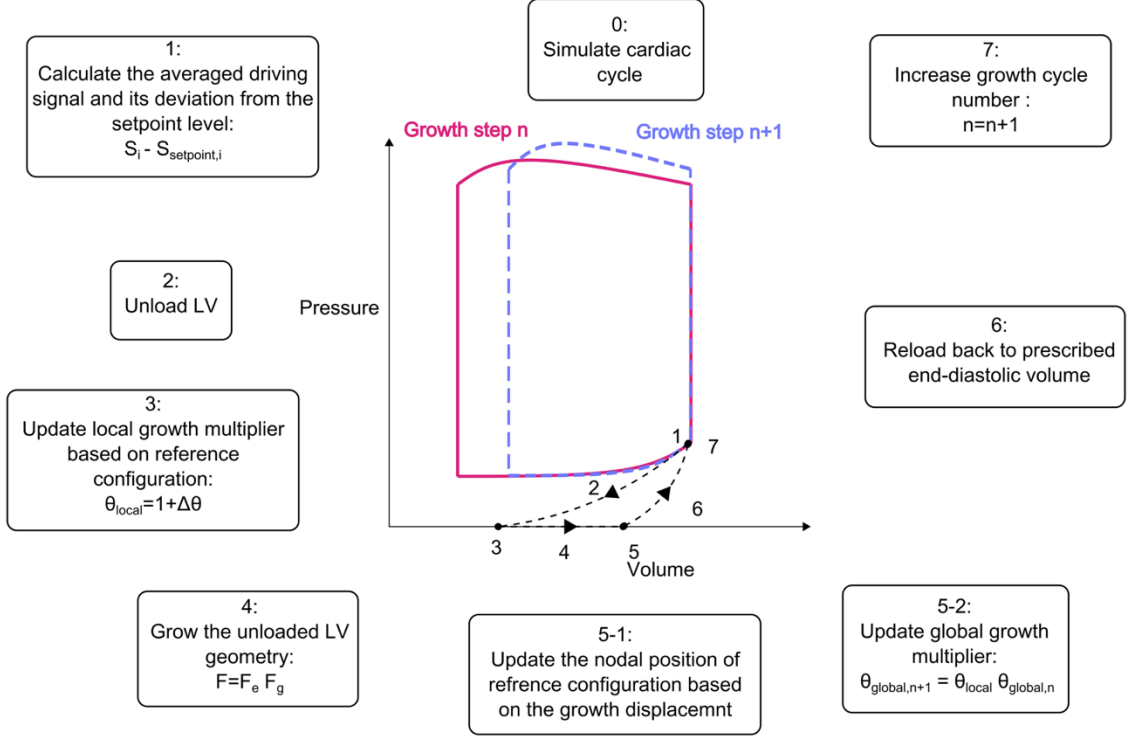


**Figure 3.2** Scheme for imposing LV growth using the updated reference configuration approach.

The weak formulation of the growth mechanics problem was obtained using the FE method to solve the following equation for  $\mathbf{u} \in H^1(\Omega_0)$  and  $p \in H^1(\Omega_0)$  such that

$$\begin{aligned} \delta \mathcal{L}_G = & \int_{\Omega_0} (\mathbf{F}\mathbf{S} - \mathbf{J}\mathbf{F}^{-T}) : \nabla \delta \mathbf{u} dV - \int_{\Omega_0} (\delta p (J - 1)) dV - \delta c_x \cdot \int_{\Omega_0} u_x dV - c_x \cdot \int_{\Omega_0} \delta u_x dV - \\ & \delta c_y \cdot \int_{\Omega_0} u_y dV - c_y \cdot \int_{\Omega_0} \delta u_y dV - \delta c_z \cdot \int_{\Omega_0} \mathbf{z} \times \mathbf{u} dV - c_z \cdot \int_{\Omega_0} \mathbf{z} \times \delta \mathbf{u} dV = 0 \end{aligned} \quad (3.14)$$

In the above equation,  $\mathbf{F}$  is deformation gradient tensor described in (3.9),  $\mathbf{S}$  is the 2<sup>nd</sup> Piola Kirchhoff stress tensor which does not include the active stress ( $\mathbf{S} = \mathbf{S}_p$ ),



$\delta \mathbf{u} \in H^1(\Omega_0)$ ,  $\delta p \in H^1(\Omega_0)$ ,  $\delta c_x \in R$ ,  $\delta c_y \in R$ , and  $\delta c_z \in R$  are test function corresponding to  $\mathbf{u}$ ,  $p$ ,  $c_x$ ,  $c_y$ , and  $c_z$  respectively. Similar to the elastic deformation, the displacement field  $\mathbf{u}$  was approximated using a quadratic tetrahedral element formulation, whereas a linear element formulation was used for Lagrange multiplier  $p$ .

### 3.2.6 Simulation cases

#### 3.2.6.1 Baseline

All simulations in this study started with default parameters to represent the cardiovascular function of a healthy adult with normal characteristics as reported in the literature [170, 171]. For example, total blood volume of the circulatory system was set to 4.5 liters such that when the system reaches to steady state the LV ejects 74 ml of blood with a heart rate of 60 beats per minute and an ejection fraction of 65%.

#### 3.2.6.2 Aortic Stenosis

According to *Poiseuille's* law, the resistance of flow across the aortic valve is proportional to one over the valve cross-sectional area squared. Therefore, the stenotic aortic valve was modeled by increasing the aortic valve resistance,  $R_{aorta}$  in equation (2.2), which describes the blood flow from the left ventricle to the aorta. According to American Heart Association (AHA) guidelines [149], a patient with asymptomatic severe aortic stenosis has a ~65 % reduction in the aortic valve area, from a mean value of 2.5 cm<sup>2</sup> for healthy adults [172-174] to a mean value of 0.86 cm<sup>2</sup> [175, 176]. This was mimicked in the current work by increasing the valve resistance from a baseline value of 20 to 170 (mmHg L<sup>-1</sup>).

### 3.2.6.3 Mitral Regurgitation

To model mitral regurgitation,  $G_{MV}$  in equation (2.2) was set to a positive value, which allows blood to leak backward through the mitral valve during systole. In the current work, we modeled a patient with progressive mitral regurgitation, as classified by AHA guidelines. Setting  $G_{MV} = 3E - 3$  (L mmHg<sup>-1</sup> s<sup>-1</sup>) resulted in a regurgitant volume of ~55 ml beat<sup>-1</sup>.

### 3.3 Results

#### 3.3.1 Concentric growth was captured in response to pressure overloading

Figure 3.3 illustrates the response of the model to a simulation of pressure overloading due to aortic stenosis. The simulation began by mimicking the baseline condition of a healthy adult. Upon reaching steady state, the system was challenged by increasing the aortic resistance from the baseline value of 20 (mmHg L<sup>-1</sup>) to 170 (mmHg L<sup>-1</sup>), simulating a 65% reduction in the aortic valve area.

The resulting perturbation elevated the pressure gradient between the ventricle and aorta, increasing the afterload against which the LV chamber ejected blood. This increased afterload led to slower myocyte shortening and an increase in total stress within the myocardium, which is caused by more myosin heads in the FG state. The diminished cardiac output lowered the arterial pressure from ~114/67 mmHg to ~107/63 mmHg. In response to the elevated stress, the growth algorithm increased the growth multiplier along local sheet and sheet-normal directions, resulting in a 24% increase in myocardial volume. The resulting change in myocardial volume caused thickening of the unloaded chamber wall (Figure 3.3.c), while the cavity volume remained unchanged, which is consistent with concentric growth in response to the pressure overloading.

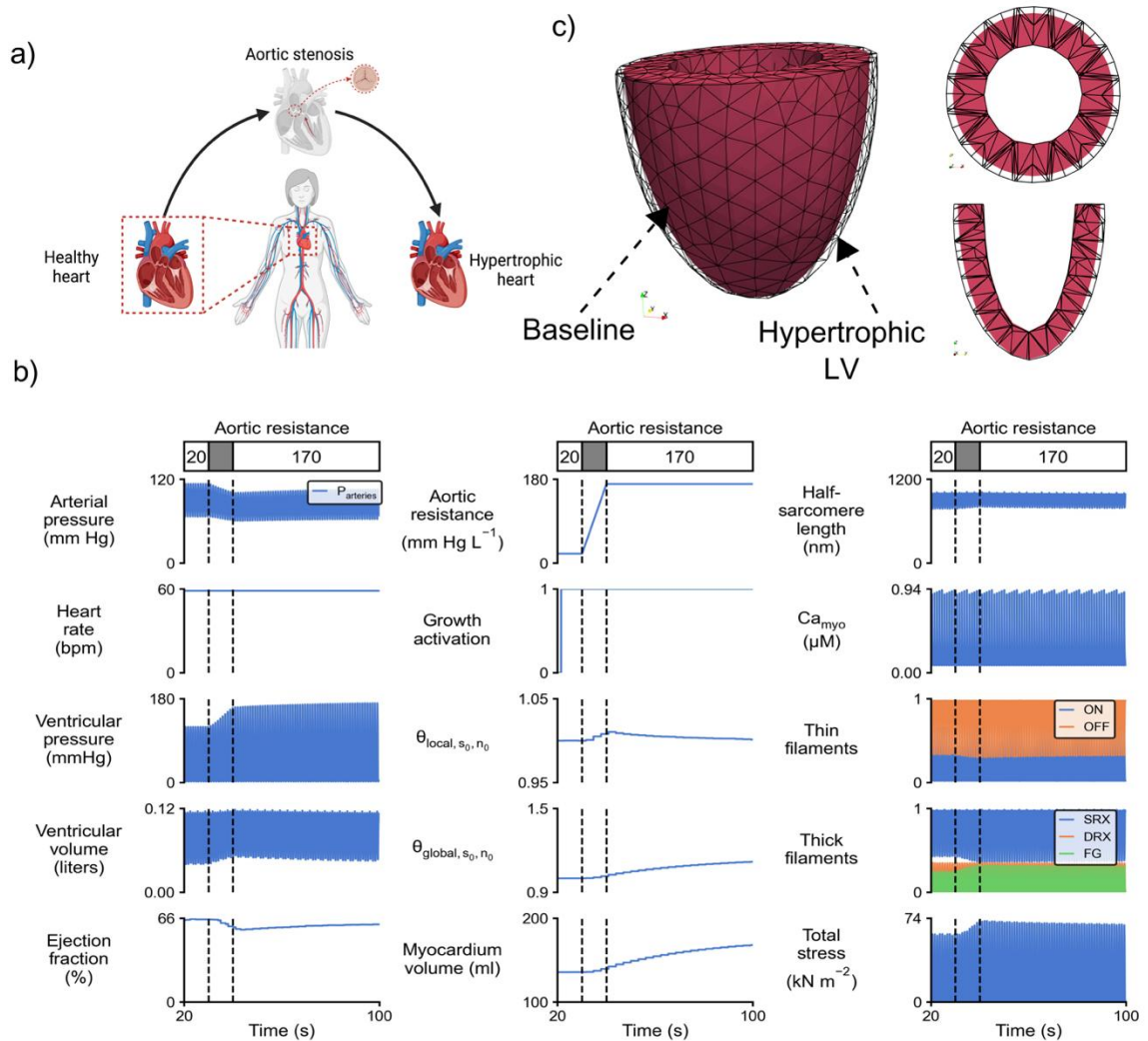


**Figure 3.3 The growth algorithm predicted thickening of the LV in response to pressure overloading.**

a) Schematic progress of concentric growth due to aortic stenosis. b) Multi-panel illustration of results for a simulation of aortic stenosis. c) Unloaded LV geometry for baseline (solid color) and hypertrophic LV (wireframe).

The left-hand column shows system-level properties. The middle column shows aortic resistance along with the model parameters related to growth algorithm. The right-hand column shows properties relevant to myocardial function. The simulation started using default parameters. The growth algorithm was initiated after 30 s. The aortic resistance was increased over a 10 s period (between the first and second vertical lines). The OFF and ON labels describe the status of binding sites on the thin filament. The SRX, DRX, and FG labels refer to myosin heads in the super-relaxed, disordered-relaxed, and force-generating states, respectively. It should be noted that the last three panels in the middle column and all panels in the right-hand column are average values over the entire LV mesh.

### 3.3.2 Eccentric growth was captured in response to volume overloading

Figure 3.4 depicts the model response to volume overloading caused by mitral regurgitation. Similar to the previously examined case of pressure overloading, the simulation began with default parameters until achieving steady state. At this stage, the left ventricle was pumping approximately 65% of its chamber volume at a rate of 60 beats per minute, producing an arterial pressure of approximately 114/67 mmHg. Upon inducing a regurgitant volume of approximately 55 ml, the  $\theta_{global, f_0}$  across the mesh increased from 1 to an average of approximately 1.22. This led to the growth of myofibers along the local myofiber direction (i.e.  $f_0$ ), resulting in an approximately 16.5% increase in myocardium volume. Consequently, the left ventricle underwent a 5% and 37% dilation for end-systolic and end-diastolic volumes, respectively. The regurgitant volume also caused a significant drop in arterial pressure to  $\sim 92/53$  mmHg, as shown in Figure 3.4.b. Regarding the unloaded geometry, the LV chamber dilated in a fairly uniform way from base to apex.

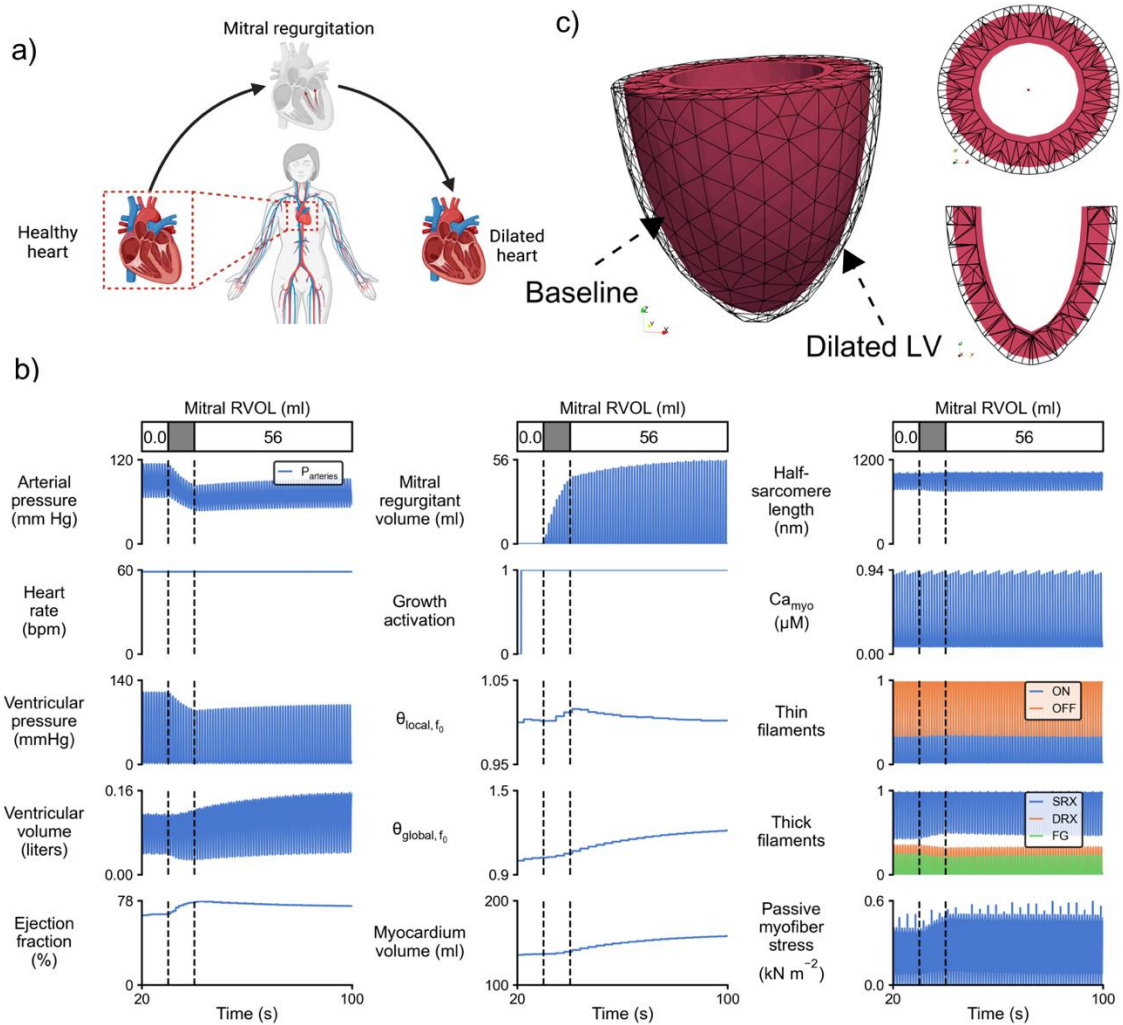


**Figure 3.4 The growth algorithm dilated LV in response to volume overloading.**

a) Schematic progress of eccentric growth due to mitral regurgitation. b) Multi-panel illustration of results for a simulation of mitral regurgitation. c) Unloaded LV geometry for baseline (solid color) and eccentric growth (wireframe). The left-hand column shows system-level properties. The middle column shows regurgitant volume along with the model parameters related to the growth algorithm. The right-hand column shows properties relevant to myocardial function. The simulation started using default parameters. The growth algorithm was initiated after 30 s. The regurgitant volume was induced over a 10 s period (between the first and second vertical lines). The OFF and ON labels describe the status of binding sites on the thin filament. The SRX, DRX, and FG labels refer to myosin heads in the super-relaxed, disordered-relaxed, and force-generating states, respectively. RVOL refers to regurgitant volume. It should be noted that the last three panels in the middle column and all panels in the right-hand column are average values over the entire LV mesh.

### **3.3.3 Effects on the pressure-volume relationship**

The results of the current study showed that the regurgitant volume induced by the leaking mitral valve had a significant impact on the forward stroke volume and peak LV pressure in comparison to the baseline case. Specifically, the forward stroke volume was reduced by approximately 23%, from 74 ml to 57 ml, resulting in a 17% drop in peak LV pressure from 118.7 to 97.7 mmHg (Figure 3.5). Mitral regurgitation also had a long-term effect on LV geometry as the end-diastolic volume dilated by 35%. Moreover, the isovolumic contraction and relaxation was perturbed due to retrograde blood flow through the mitral valve.

In contrast, aortic stenosis resulted in a 43% increase in peak systolic pressure due to the elevated pressure gradient between the ventricle and aorta. The long-term change in left ventricular geometry was a roughly 10% increase in end-systolic volume while the end-diastolic volume did not change and remained at the baseline level.

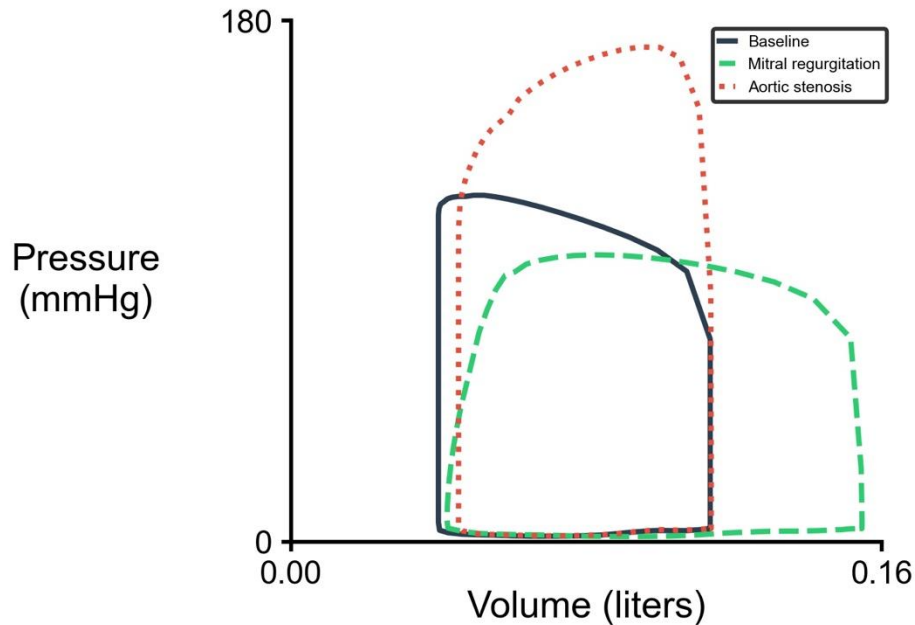


*Figure 3.5 Predicted pressure-volume relationships.*

### **3.3.4 Reversal of growth when the perturbation was removed**

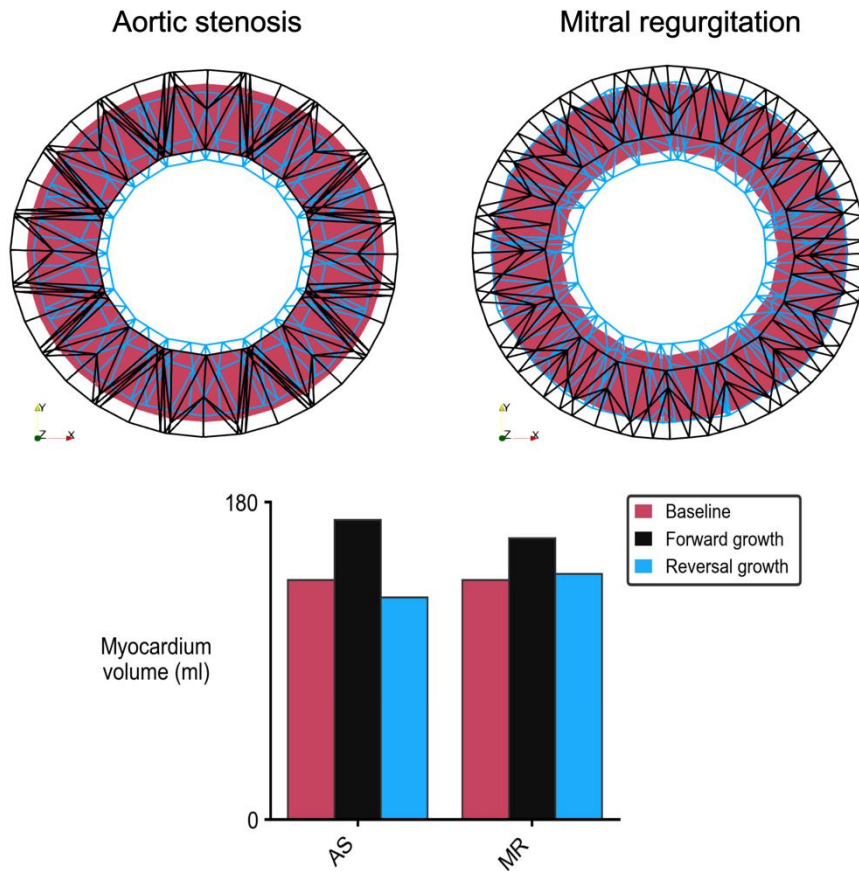
We aimed to investigate whether our computational model is capable of accurately capturing the phenomenon of reversed growth. Specifically, we examined the effects of treating mitral regurgitation (MR) and aortic stenosis (AS) by simulating the removal of underlying perturbations, such as regurgitant volume and elevated pressure gradient. To simulate these effects, we repeated the simulations illustrated in Figure 3.4 and Figure 3.5, but once the final forward growth step was captured we removed the underlying perturbation and continued the simulation for another 100 cardiac cycles.

Figure 3.6 demonstrates that the relief of myocytes from overstretching, due to the removal of excessive diastolic filling (i.e. treated MR), led to a reduction in myocardial volume, which was 2.5% higher than the myocardial volume at baseline. Regarding the



nodal position of the unloaded geometry, the growth algorithm displaced all the epicardial nodes back to their original coordinates at baseline. However, the endocardial nodes shifted slightly inward compared to the original nodes at baseline.

For the AS case, the removal of elevated aortic resistance reduced the pressure gradient (afterload) and sped up the myocyte shortening, which in turn reduced the total stress in the LV wall. This reduction led to the reversal of hypertrophy and decrease of myocardial mass, which was 7% lower than its baseline level. In terms of the nodal positions of the stress-free geometry, the thickness of left ventricular wall reduced, however, both epicardial and endocardial nodes shifted inwards in comparison to their original location at baseline.



**Figure 3.6** Reversal of LV growth in response to removal of valvular diseases. AS: Aortic stenosis, MR: Mitral regurgitation

### 3.4 Discussion

The approach described in this study utilized a computational model of the cardiovascular system that integrates a volumetric growth algorithm to simulate both concentric growth (wall thickening / thinning) and eccentric growth (chamber dilation / constriction). The growth algorithm uses time-average stresses, specifically, total stress and myofiber passive stress for driving concentric and eccentric growth, respectively. The results of this study showed that the new framework could predict the correct form of LV

growth in response to two forms of valvular disease, namely, aortic stenosis and mitral regurgitation. Moreover, simulations for each valvular disorder regained LV size and function (reversal of growth) when the disease-mimicking perturbation was removed.

### **3.4.1 Role of myofiber passive stress in driving eccentric growth**

Valvular diseases such as mitral regurgitation can cause eccentric growth in patients, driven by a cellular-level mechanism known as mechanotransduction [177]. This condition results in excessive diastolic filling of the left ventricle, leading to sarcomere overstretching. Consequently, higher stresses at the end of the sarcomeres are sensed by proteins located in these regions [178]. Titin, which spans from the Z disk to the M line, contains an elastic structure within the I band that interacts with other proteins on the Z disk and provides the passive stiffness of the sarcomeres by storing strain energy during diastole [177]. Mechanical stimuli in the form of passive stresses are sensed by sarcomeric titin domains, triggering a cascade of downstream signals that ultimately upregulate protein synthesis, sarcomere addition, and myocardium growth.

In the current model, we define that the intracellular myofiber passive stress has a nonlinear relationship with half-sarcomere stretch, as described in equation (3.7). Accordingly, volume overloading causes an initial increase in diastolic filling of the left ventricle, leading to half-sarcomere overstretching and a rise in time-averaged intracellular passive stress. In response to this elevated mechanical stimulus, the growth algorithm increases the growth multiplier along the fiber direction, reducing the extent of half-sarcomere stretch and thus alleviating the passive stress felt by myofibers. This mechanism drives the serial deposition of sarcomeres and the subsequent eccentric growth of the left ventricle.

In response to a progressive mitral regurgitation, our model predicted increased myocardial volume along the fiber direction. This led to the dilation of LV at both end diastole and end systole, which has been observed in the literature [179-181]. Our model predicted a 16.5 % increase in myocardial mass, while Schiros et al. [180] reported a 28% increase for MR patients with roughly the same regurgitant volume (i.e. ~55 ml) as our model. Regarding left ventricular chamber volume, our model prediction for the change in end-diastolic volume was aligned with the reported change by Schiros et al. (37% versus 52%). Moreover, in our model arterial pressure dropped from 114/67 to ~92/53 mmHg, however, patients with MR showed no difference in their blood pressure comparing to the control volunteers [180].

### **3.4.2 Role of myofiber total stress in driving concentric growth**

In patients with aortic stenosis, concentric growth is induced by the pressure overload experienced by the heart. This mechanical condition is characterized by an increase in the resistance of blood flow through the aortic valve during left ventricular systole. Consequently, the shortening velocity of sarcomeres is reduced. In the current study, this reduced shortening velocity increases the number of bound myosin heads in the MFG state, which mainly occurs because fewer myosin heads are pulled off due to strain-dependent detachment. Ultimately, this elevates the time-averaged total stress generated by myofibers, which drives the growth algorithm to grow the myocytes in the cross-fiber directions (i.e.  $\mathbf{s}_0$  and  $\mathbf{n}_0$ ). Our approach is further in line with recent findings that have investigated the stimulus signal for concentric growth. For instance, Davis et al. [169] demonstrated that concentric hypertrophy is associated with an increased force-time integral, which reflects the mechanical work performed by the heart. Therefore, using time-

averaged total stress could be used to model myocyte thickening in response to pressure overloading.

Comparing to reported measures in the literature, our growth algorithm predicted a 24% increase in LV mass in response to the simulated AS case, which was close to the reported change (32% increase) by Chin et al. [172] for patients with mild to severe AS. Additionally, our model predicted almost no change for left ventricular chamber volume, which aligned with reported data for patients with AS [172, 182]. Similar to MR case, our simulation for AS resulted in roughly 6% decrease in arterial pressure, although such a change has not been observed in the literature [182].

### **3.4.3 Integration of LV growth with a mechanistic model of half-sarcomeres at myosin-level**

Since the emergence of computational modeling of left ventricular (LV) growth [38], many models have shed light on the underlying mechanics of the LV growth that occurs. However, existing models have certain limitations related to the assumptions used for representing systolic function during the cardiac cycle. For example, some models [41, 59, 66] have only simulated LV growth during diastolic loading and neglected the systolic behavior of myocardium during ejection. Other models [63, 65, 68] investigated the mechanics of LV growth under a full cardiac cycle, but the contractile function was simulated using phenomenological Hill-type models. Yet another group of works [64, 74] used a time-varying elastance model of the ventricle to simulate a full cardiac cycle.

In contrast, our current framework simulates LV growth under a full cardiac cycle, in which the contractile behavior of the LV is driven by a mechanistic model of half-sarcomeres. This model simulates the sliding of myofilaments based on the Huxley

crossbridge formation [183] at the myosin level. Modeling the mechanics of sarcomeres at this level allows us to capture length-dependent activation, cooperativity between thick and thin filaments, and the strain-dependent behavior of cross-bridges, which is more realistic. Furthermore, using such models, we can study the effects of pathological processes at the molecular level and how they affect disease development at the organ level. Additionally, this framework could potentially be used to study the effects of various pharmaceutical interventions for treating cardiac diseases.

#### **3.4.4 Reversal of growth**

The reversal of cardiac growth is a favorable outcome of clinical interventions for dysfunctional valves, i.e., when the ventricle returns to a normal size and shape. Although existing computational models have shown success in predicting the development of growth, many of them are challenged when trying to predict the reversal of growth [1, 85].

Of the few works that have studied the reversal of growth, Lee et al. [41] modified a previously developed eccentric growth law [66] and were able to capture the reversal of growth for a realistic LV geometry under certain types of loading. In particular, their model was based on diastolic stretch as the driving growth signal and was only tested for volume overloading. Arumugam et al. [68] extended their previous work [41] and investigated the development of anisotropic growth in a biventricular model of the heart in response to mechanical dyssynchrony. Using maximum elastic myofiber stretch over a cardiac cycle as the sole stimulus signal of their growth law, their model demonstrated growth in the left ventricular chamber size and septal wall, but reversal of growth for the right ventricular chamber size and LV free wall. In a more recent work, Yoshida et al. [70] investigated the regression of growth due to the removal of pressure overloading, while using the growth

law developed by [63]. Although this strain-driven growth law performed the best in capturing the development of LV growth, in comparison to seven other growth laws [72], it could not predict the reversal of growth. Yoshida et al. [70] further suggested that using an evolving setpoint could potentially address the inability of existing models to predict the reversal of growth. Built upon this hypothesis, Oomen et al. [184] used this idea of “evolving setpoint” and was able to capture the reversal of growth when assessing Cardiac Resynchronization Therapy.

Our model was able to regain the LV size and function once the underlying perturbation for each valvular disorder was lifted. There are several potential explanations for this result. Firstly, our framework uses a mechanistic model of a half-sarcomere to simulate the contractile behavior of myocardium [97, 98]. Such a model can account for the effects of altered ventricular loading on the force generation of half-sarcomere that other models may be unable to capture. For instance, Yoshida et al. [70] had to manually adjust the muscle contractility in their model to mimic the lower force production of myocardium due to the removal of pressure overloading. In contrast, removal of the aortic stenosis condition in our model led to lower hemodynamic resistance during LV systole, which in turn increased the shortening velocity of half-sarcomeres due to higher strain in the myosin heads. This event reduces the number of bound myosin heads in the force-generating state ( $M_{FG}$ ) and thus lowers the associated force that is generated in the half-sarcomere, such that it matches with the altered hemodynamic loading.

Secondly, the choice of growth stimulus may be the reason for the inability of previous models to predict the reversal of growth, particularly in the presence of pressure overloading. Yoshida et al. [70] and Oomen et al. [184] both utilized the minimum of the

first principle strain to drive myocyte thickening. However, prior research has demonstrated that, without incorporating the concept of an "evolving setpoint," the growth stimulus does not decrease below the constant setpoint after the removal of pressure overloading, resulting in the growth model's inability to capture the reversal of growth. In contrast, our model employs time-averaged total stress along the myofiber direction as the growth stimulus, which is more consistent with the findings of other researchers who have suggested that myofiber stress may be a superior growth stimulus for pressure overloading. For instance, Rondanina and Bovendeerd [40] tested four combinations of myofiber stress and strain driven laws, for both concentric and eccentric growth, and concluded that using at least one stress-driven law would predict more reliable growth. In another study, Mojumder et al. [39] showed that concentric growth of the LV, due to pressure overloading, correlates better with myofiber stress than stretch/strain.

### **3.5 Limitations**

Although the current model resolves some of the issues found in previous studies of cardiac G&R [1], the simulations presented here still have some limitations. First, the current model, like many other existing models of cardiac G&R, does not incorporate the effect of hemodynamic reflex. This limitation led to some mismatch between the predicted arterial pressure and reported measures in the literature for patients with valve diseases. For instance, in our model arterial blood pressure dropped from  $\sim 114/67$  to  $\sim 107/63$  mmHg and  $\sim 92/53$  mmHg for aortic stenosis and mitral regurgitation, respectively, which are in contrast to reported data in such patients in the literature [179, 181]. Moreover, the absence of hemodynamic reflex can indirectly impact the performance of the algorithm in capturing long-term growth. Essentially, in the presence of a reflex control, the arterial pressure



would have been preserved when the system was challenged the valvular diseases. Therefore, the LV would have been functioning against a different level of loading that could result in some variation in predicted growth. The incorporation of a baroreflex control will be the focus of future work.

A second limitation of the current model is that we did not tune the rate constants in the local theta equations. This would require fitting to experimental data to find the correct rate constants to mimic the true time course of growth, i.e., find a set of rate constants such that one growth step represents a certain number of days, weeks, etc. The focus of the current work is on the utilization of the time-average of stress as the growth driver, and its interplay with the mechanistic law of active contraction. However, this will also be to focus of future studies. Another limitation is that the reversal of growth did not lead to a perfect recreation of the baseline geometry. However, this is somewhat expected given the path dependent nature of growth, due to the multiplicative split of the deformation gradient, which is based on finite plasticity theory, and the discrete motion of the FE mesh. Lastly, the current framework can only quantify the cardiac growth (i.e., change in the ventricular size and dimension), but not the myofiber remodeling. Alterations in mechanical loading can be accompanied by myofiber disarray and remodeling [18, 185]. However, this will be accounted for in future work.

### **3.6 Summary and conclusion**

This work extends a multiscale model of cardiovascular function by integrating a volumetric growth algorithm, which was based on the time-averaged stress over a cardiac cycle. The central framework uses a mechanistic model of half-sarcomeres to drive the

contractile function of myocytes at the myosin-level. Results of this study showed that the model could predict both concentric (wall thickening / thinning) and eccentric (chamber dilation / constriction) growth in simulations of valve diseases. Additionally, the newly extended framework could regain the LV size and function (reversal of growth) when the disease-mimicking perturbation was removed. In conclusion, the results of this study suggest that time-averaged total stress and time-averaged myofiber passive stress can be used to drive concentric and eccentric growth in simulations of valve disease.

## 4.1 Introduction

The heart pumps blood through the circulatory system in a regulated manner, which is governed by several mechanisms operating across multiple scales. It can adapt its size and shape in response to acute or chronic alterations in pumping demand due to either physiological or pathological changes. This process, referred to as cardiac growth and remodeling (G&R), is driven by a number of processes at the cellular level including alterations in signaling pathways and neurohormonal activation. These changes are manifested through wall thickening and/or chamber dilation at the organ level.

Computational cardiac G&R models have been seen as a useful tool to enhance our understanding of the complex interaction/behavior of how living systems adapt when their loading conditions change. Although current models have done a good job in predicting of the long-term change in the geometry of the heart, they have paid less attention to the predicted hemodynamics and the role of baroreflex mechanisms in altering the predicted G&R [1]. For instance, Kerckhoffs et al. [63] introduced a single strain-based model of cardiac growth, which was able to predict the correct form of growth due to either pressure or volume overloading. However, they reported a mismatch between the calculated peak left ventricular (LV) cavity pressure and that measured in experiments and posited that it could be due to the lack of a short-term baroreflex responses in their model. In another study by Witzenburg and Holmes [159], they investigated the role of compensatory reflexes that act to preserve mean arterial pressure (MAP) and its effect on the predicted

growth post myocardial infarction. They showed that the variability in the compensatory reflex mechanism can lead to different extent of predicted LV dilation consistent with reported variability in the literature. Another model developed by Rondanina and Bovendeerd [40] studied the effect of different mechanical stimulus signals in the prediction of cardiac growth in simulations of valvular diseases. However, their model predicted a 20% to 40% reduction in mean arterial pressure and cardiac output. In their subsequent work [73], they showed coupling a simplified reflex model with their growth model could capture more realistic cardiac growth and preserved cardiac pump function.

Building on these observations, in our previous work described in CHAPTER 3, we implemented a volumetric growth algorithm into the MyoFE framework, which is a high-fidelity multiscale model of cardiovascular function based on finite element modeling (FEM). The growth algorithm used total stress along the myofiber direction, which was time-averaged over a cardiac cycle, to drive the myofiber growth in the cross-fiber directions (i.e. sheet and sheet-normal), while growth along the fiber direction was governed by time-averaged myofiber passive stress over a cardiac cycle. The growth module was able to predict the correct form of growth in simulations of valvular disease. However, it was shown in those simulations that the model predicted lower systolic pressure within the LV cavity and lower mean arterial pressure in the arteries, which in turn, might not be as realistic as reported data in vivo.

Although valvular disorders might result in decreased cardiac function [186], in general, arterial pressure and cardiac output may be maintained at normal levels for such patients [104, 187-189]. In people, mean arterial pressure is maintained via several known mechanisms, such as the renin-angiotensin system [190] and the secretion of natriuretic

peptides [191], which adjust renal excretion of salt and water to regulate blood pressure over longer timescales. On the other hand, another mechanism, called the baroreflex loop, controls arterial pressure over short-term timescales. This feedback loop changes the activity of the sympathetic and parasympathetic nervous system in response to changes in blood pressure. When blood pressure rises, the baroreceptors in the carotid sinus and aortic arch detect the increased strain in the vessel walls and send signal to the brainstem or medulla. The brainstem then fires a signal that causes the sympathetic nervous system to decrease its activity and the parasympathetic nervous system to increase its activity. The net result of this change in the activity of the efferent neuron pathway is a decrease in heart rate, blood vessel constriction (vasodilation), contractility of the heart, and consequently an overall decrease in blood pressure. Similarly, when blood pressure falls the baroreceptors capture the decrease, which causes the opposite changes in the sympathetic and parasympathetic nervous system, leading to an increase in heart rate, vascular tone, contractility, and thus an overall increase in arterial blood pressure [134].

In this chapter we incorporated the baroreflex algorithm that was described in CHAPTER 2 into the framework outlined in CHAPTER 3 to study the role of compensatory reflex on the degree of predicted LV growth. The results of this study showed that the coupled baroreflex-growth algorithm predicted a more realistic form of growth and hemodynamic function consistent with the clinical data reported in the literature.

## 4.2 Method

This chapter combines three frameworks/algorithms, namely the central framework of MyoFE, a baroreflex algorithm, and a growth algorithm that are described in CHAPTER 2 and CHAPTER 3. Briefly, the central framework simulates the elastic deformation of the LV using a finite-element model. In this framework a pacing stimulus drives a simplified model of electrophysiology to compute the  $\text{Ca}^{2+}$  transient for calculation of contractile stress at the myosin-level. A 3-D ellipsoidal geometry of the LV then pumps blood into the systemic side of the circulatory system. The baroreflex algorithm, as was described in CHAPTER 2, controls arterial pressure at a setpoint level by regulating heart rate, intracellular  $\text{Ca}^{2+}$  transient, myofilaments function, and vascular tone. Lastly, the growth algorithm CHAPTER 3) captures long-term changes in the size and shape of the LV geometry by mimicking the serial and parallel deposition of sarcomeres, along the fiber and cross-fiber directions, in response to changes in the growth stimuli.

In addition to viewing our previous works, more details on the description of the central framework shown in Figure 4.1, such as the electrophysiology model, the finite element formulation of elastic deformation, and the contractile mechanics of LV model, are described in CHAPTER 2. In the following, we first briefly describe the lumped-parameter model of circulation. Then we outline the details of the LV geometry and cardiac mechanics. Finally, we describe the methodology of the baroreflex algorithm and constitutive law of the growth algorithm.

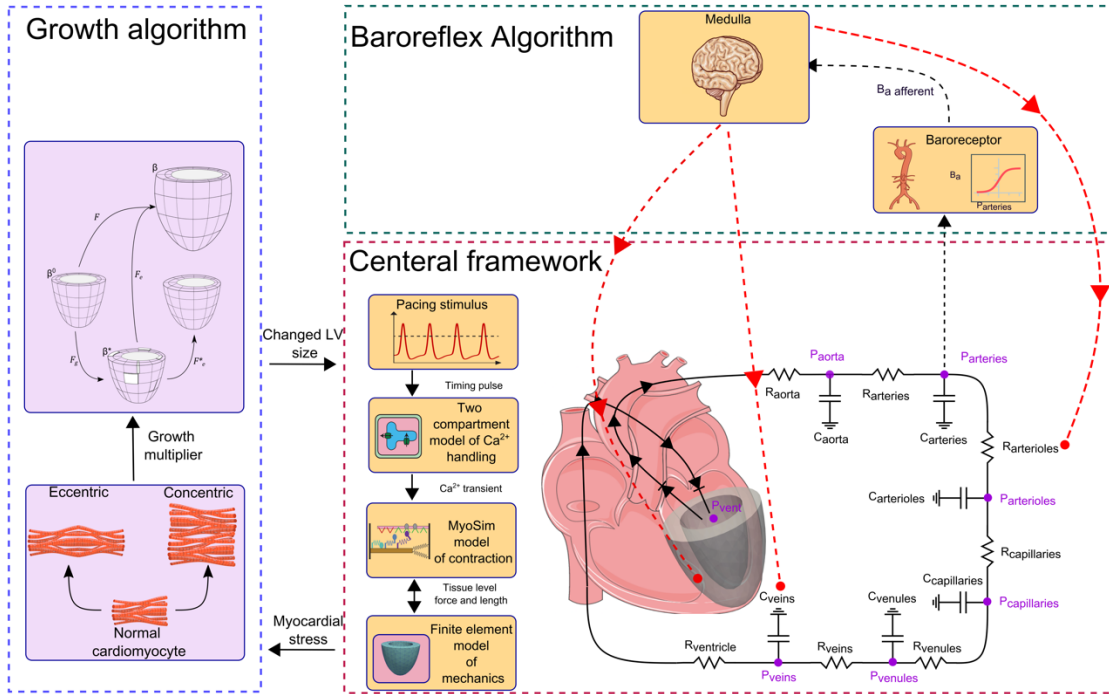


**Figure 4.1 Overview of MyoFE framework.** The central framework simulates the elastic deformation of a finite-element model of the LV. The baroreflex algorithm controls arterial pressure by regulating heart-rate, intracellular  $Ca^{2+}$  transient, function of both myofilaments, and vascular tone. The growth algorithm captures the long-term change in geometry of the LV due to overloading.

#### 4.2.1 Circulation

The circulation model in the central framework mimics only the systemic circulation. In addition to the LV, there are six additional compartments, namely Aorta, Arteries, Arterioles, Capillaries, Venules, and Veins, each of which possessed a compliance denoted by  $C_j$  and a resistance denoted by  $R_j$ . The blood volume within each compartment undergoes a rate of change that is determined by the difference between the inflow and outflow of blood into and out of that particular compartment (equation (4.1)).

$$\begin{aligned}
\frac{dV_{aorta}}{dt} &= Q_{LV \text{ to aorta}} - Q_{aorta \text{ to arteries}} \\
\frac{dV_{arteries}}{dt} &= Q_{aorta \text{ to arteries}} - Q_{arteries \text{ to arterioles}} \\
\frac{dV_{arterioles}}{dt} &= Q_{arteries \text{ to arterioles}} - Q_{arterioles \text{ to capillaries}} \\
\frac{dV_{capillaries}}{dt} &= Q_{arterioles \text{ to capillaries}} - Q_{capillaries \text{ to venules}} \quad (4.1) \\
\frac{dV_{venules}}{dt} &= Q_{capillaries \text{ to venules}} - Q_{venules \text{ to veins}} \\
\frac{dV_{veins}}{dt} &= Q_{venules \text{ to veins}} - Q_{veins \text{ to LV}} \\
\frac{dV_{LV}}{dt} &= Q_{veins \text{ to LV}} - Q_{LV \text{ to aorta}}
\end{aligned}$$

The flow of blood between two compartments is regulated by Ohm's law and is associated with the pressure gradient between the compartments and the resistance of the receiving compartment. The resulting blood flows can be succinctly described as follows:

$$\begin{aligned}
Q_{LV \text{ to aorta}} &= \begin{cases} \frac{P_{LV} - P_{aorta}}{R_{aorta}} & \text{when } P_{LV} \geq P_{aorta} \\ (P_{LV} - P_{aorta})G_{AV} & \text{otherwise} \end{cases} \\
Q_{aorta \text{ to arteries}} &= \frac{P_{aorta} - P_{arteries}}{R_{arteries}} \\
Q_{arteries \text{ to arterioles}} &= \frac{P_{arteries} - P_{arterioles}}{R_{arterioles}} \\
Q_{arterioles \text{ to capillaries}} &= \frac{P_{arterioles} - P_{capillaries}}{R_{capillaries}} \\
Q_{capillaries \text{ to venules}} &= \frac{P_{capillaries} - P_{venules}}{R_{venules}} \\
Q_{venules \text{ to veins}} &= \frac{P_{venules} - P_{veins}}{R_{veins}} \\
Q_{veins \text{ to LV}} &= \begin{cases} \frac{P_{veins} - P_{LV}}{R_{LV}} & \text{when } P_{veins} \geq P_{LV} \\ (P_{veins} - P_{LV})G_{MV} & \text{otherwise} \end{cases} \quad (4.2)
\end{aligned}$$



where  $G_{AV}$  and  $G_{MV}$  are model parameters controlling the leakage through the aortic and mitral valves, respectively. The blood pressure within each compartment, except the LV is described as:

$$P_i = \frac{V_i(t) - V_{i,slack}}{C_i} \quad (4.3)$$

where  $V_i(t)$ ,  $V_{i,slack}$  and  $C_i$  are the instantaneous blood volume, the slack volume, and the compliance of the compartment  $i$ , respectively. The LV pressure, on the other hand, was calculated from FE model according to  $V_{LV}$  as the input.

#### 4.2.2 LV model geometry

An ellipsoidal geometry of a human LV with  $\sim 1280$  tetrahedral elements was used in this study. The slack chamber volume of the LV was 66 ml with a myocardial volume of 136 ml. The length of the LV from base to apex was roughly 7 cm, while the outer diameter of the LV at base was 7.1 cm. Myofiber directions  $f_\theta$  were defined by linearly changing the helix angle from  $60^\circ$  at endocardium to  $-60^\circ$  at the epicardium transmurally across the wall (Figure 2.2) using a Laplace-Dirichlet rule-based algorithm [142].

#### 4.2.3 Finite element formulation of elastic deformation

The solution for LV mechanics was approximated using an implicit backward Euler scheme for numerical time-integration with a fixed time step of 1 ms. An open-source FE library called FEniCS [143] was used for this purpose. The FE formulation of the LV mechanics problem was prescribed by minimizing the Lagrangian functional described in the supplementary materials.

#### 4.2.4 Cardiac mechanics

To define the LV mechanics, the 2<sup>nd</sup> Piola Kirchhoff stress tensor was additively decomposed into an active component  $\mathbf{S}_a$  and a passive component  $\mathbf{S}_p$  i.e.

$$\mathbf{S} = \mathbf{S}_a + \mathbf{S}_p \quad (4.4)$$

The myocardial tissue was modeled to be incompressible, hyperelastic, and transversely isotropic. The passive component of the stress tensor further decomposed into three responses. This is due to incompressibility and the force-reliant nature of the active stress, which necessitates that the passive stress be decomposed into parts that account for the myofibers and remaining bulk tissue. Each response was obtained by differentiating a strain energy function with respect to Green-Lagrangian strain tensor,  $\mathbf{E}$ :

$$\mathbf{S}_p = \mathbf{S}_{vol} + \mathbf{S}_{bulk} + \mathbf{S}_{myofiber} = \frac{\partial \psi_{vol}}{\partial \mathbf{E}} + \frac{\partial \psi_{bulk}}{\partial \mathbf{E}} + \frac{\partial \psi_{myofiber}}{\partial \mathbf{E}} \quad (4.5)$$

More details on calculation of each component are outlined in CHAPTER 2. The active component,  $\mathbf{S}_a$ , of the total stress tensor was determined using the MyoSim framework [97], which is characterized in CHAPTER 2. Finally, using the active stress experienced by a myofiber  $F_{active}$ , the active stress tensor can be described as:

$$\mathbf{S}_a = F_{active} \mathbf{f}_0 \otimes \mathbf{f}_0 \quad (4.6)$$

#### 4.2.5 Baroreflex

The baroreflex algorithm is adapted from CHAPTER 2. Essentially, in this algorithm the afferent pathway is simplified via a normalized afferent signal  $B_a$  that has a sigmoidal relationship with arterial pressure ( $P_{arteries}$ ):

$$B_a(t) = \frac{1}{1 + e^{-S(P_{arteries}(t) - P_{set})}} \quad (4.7)$$

where  $P_{set}$  is the setpoint for arterial pressure, and  $S$  defines the slope of the function around its midpoint.

The efferent pathway, on the other hand, is described via a single balance signal  $B_b$ ,  $5k+3$  unique control signals ( $B_{c,1}, B_{c,2} \dots B_{c,5k+3}$ ), and  $5k+3$  distinct mapping functions ( $M_1, M_2 \dots M_{5k+3}$ ), where  $k$  represents the number of integration points present across the LV mesh. The balance signal  $B_b$  is a normalized representation of the difference between sympathetic and parasympathetic efferent activity. Its rate of change was defined as:

$$\frac{dB_b(t)}{dt} = \begin{cases} -k_{drive} (B_a(t) - 0.5) B_b(t) & B_a \geq 0.5 \\ -k_{drive} (B_a(t) - 0.5) (1 - B_b(t)) & B_a < 0.5 \end{cases} \quad (4.8)$$

where  $k_{drive}$  is a rate constant. The balance signal converges to the value of 1 when the sympathetic drive dominates the control loop. Alternatively, when the parasympathetic has a greater influence, the balance signal  $B_b$  approaches to zero.

The control signals  $B_{c,i}$  describe how each of reflex-sensitive parameters in the cardiovascular model respond to the balance signal. Similar to equation (4.8), their rates of change were defined as

$$\frac{dB_{c,i}(t)}{dt} = \begin{cases} k_{control,i} (B_b(t) - 0.5) (1 - B_{c,i}(t)) & B_b \geq 0.5 \\ k_{control,i} (B_b(t) - 0.5) B_{c,i}(t) & B_b < 0.5 \end{cases} \quad (4.9)$$

where  $i$  ranges from 1 to  $5k+3$  and  $k_{control,i}$  is the rate constant for system  $i$ .

Moreover, these signals are normalized, and reflect the cellular processes governed by autonomic control. Each signal tends to converge to a saturated value of unity when sympathetic drive exceeds parasympathetic drive, ( $B_b > 0.5$ ). Conversely, if parasympathetic drive prevails (i.e.  $B_b < 0.5$ ), it causes the control signals to gradually diminish towards zero.

The final step in the algorithm used mapping functions  $M_i$  to link the normalized control signals  $B_{c,i}$  to actual parameter values. Each mapping function took the form

$$M_i(B_{c,i}(t)) = \begin{cases} M_{base,i} + \frac{1}{2}(B_{c,i}(t) - 0.5)(M_{symp,i} - M_{base,i}) & B_{c,i} \geq 0.5 \\ M_{base,i} + \frac{1}{2}(B_{c,i}(t) - 0.5)(M_{para,i} - M_{base,i}) & B_{c,i} < 0.5 \end{cases} \quad (4.10)$$

where  $M_{base,i}$  is the default value for parameter  $i$ , and  $M_{symp,i}$  and  $M_{para,i}$  are its limits during maximum sympathetic and maximum parasympathetic drive respectively. These control signals and mapping functions operate to modulate crucial physiological processes, including heart rate,  $Ca^{2+}$  transients, myofilament function, and vascular tone.

#### 4.2.6 Growth constitutive model

The growth algorithm in the current work is based on the volumetric growth theory by Roudriguez et al. [38]. According to this theory, the total deformation gradient tensor ( $\mathbf{F}$ ) can be multiplicatively decomposed into an elastic component  $\mathbf{F}_e$  and incompatible growth  $\mathbf{F}_g$  component, i.e.

$$\mathbf{F} = \mathbf{F}_e \mathbf{F}_g \quad (4.11)$$

The growth deformation gradient tensor is further described as:

$$\mathbf{F}_g = \theta_{local,f_0} \mathbf{f}_0 \otimes \mathbf{f}_0 + \theta_{local,s_0} \mathbf{s}_0 \otimes \mathbf{s}_0 + \theta_{local,n_0} \mathbf{n}_0 \otimes \mathbf{n}_0 \quad (4.12)$$

where  $\theta_{local,f_0}$ ,  $\theta_{local,s_0}$ , and  $\theta_{local,n_0}$  are local scalar growth multipliers along the myofiber  $\mathbf{f}_0$ , sheet  $\mathbf{s}_0$ , and sheet-normal  $\mathbf{n}_0$  directions in the reference configuration that represent growth between two consecutive growth steps. The rate of change in each local growth multiplier is prescribed as:

$$\frac{\partial \theta_{local,j}}{\partial t} = \begin{cases} \frac{1}{\tau_{fg,j}} \left( \frac{\theta_{max,j} - \theta_{global,j}}{\theta_{max,j} - \theta_{min,j}} \right) \frac{S_j - S_{setpoint,j}}{|S_{setpoint,j}|} & S_j - S_{setpoint} \geq 0 \\ \frac{1}{\tau_{rg,j}} \left( \frac{\theta_{global,j} - \theta_{min,j}}{\theta_{max,j} - \theta_{min,j}} \right) \frac{S_j - S_{setpoint}}{|S_{setpoint,j}|} & S_j - S_{setpoint} < 0 \end{cases} \quad (4.13)$$

In above equation,  $j$  denotes local myofiber  $\mathbf{f}_0$ , sheet  $\mathbf{s}_0$ , and sheet-normal  $\mathbf{n}_0$  directions.  $\tau_{fg,j}$  and  $\tau_{rg,j}$  are rate time constants associated with forward growth and reverse growth in the  $j$  direction.  $S_j$  is the stimulus signal and  $S_{setpoint,j}$  is the homeostatic setpoint level of the stimulus signal, associated with growth along the  $j$  direction. The stimulus signal ( $S_j$ ) and its homeostatic level ( $S_{setpoint,j}$ ) were established at each integration point across the mesh, which was accomplished by running a baseline simulation without any valvular perturbation. Similar to the work described in CHAPTER 3, the stimulus signal for eccentric growth along the myofiber direction  $\mathbf{f}_0$  was assumed to be the time-averaged myofiber passive stress over a cardiac cycle described as:

$$S_{f_0} = \frac{1}{T} \int_0^T \mathbf{f}_0 \cdot S_{myofiber} \mathbf{f}_0 dt \quad (4.14)$$

where  $T$  is the period of one cardiac cycle. The stimulus signal for concentric growth in the cross-fiber directions ( $\mathbf{s}_0$  and  $\mathbf{n}_0$ ) was driven by the time-averaged total stress (passive and active) along the myofiber direction over a cardiac cycle. These signals are defined as:

$$\mathbf{S}_{s_0} = \mathbf{S}_{n_0} = \frac{1}{T} \int_0^T f_0 \cdot \mathbf{S} f_0 dt \quad (4.15)$$

According to equation (4.13), growth does not occur when the stimulus signal is equal to its homeostatic level.  $\theta_{global,j}$  is the global growth multiplier at each integration point that represents the total accumulation of growth in the direction  $j$  relative to the initial reference configuration. These values are bounded between  $\theta_{max,j}$  and  $\theta_{min,j}$ , which reflect the maximum and minimum physiological tissue growth. In equation (4.13), as  $\theta_{global,j}$  tends towards  $\theta_{max,j}$  or  $\theta_{min,j}$  the rate of change in the local growth multiplier  $\frac{\partial \theta_{local,i}}{\partial t}$  tends to 0 and stops the myocardium from excessive growth or shrinkage. Model parameters utilized for one of the simulations in this study can be found in APPENDIX 3. FILE S3.

#### 4.2.7 Separation of timescales between growth and elastic deformation

In vivo, LV growth takes place over a longer period of time, such as weeks and months. Therefore, in this study we separated the timescale of growth mechanics and normal elastic deformation to be consistent with the employed approach in CHAPTER 3 and other works [65, 68]. Based on this approach, the growth step occurs after a certain number of cardiac cycles, which can be set by the user. For instance, in this study, the growth step occurred every 3 cardiac cycles. More specifically, normal elastic deformation was used during these cycles and then the growth step takes place at the very end of the 3<sup>rd</sup> cycle (as outlined in Figure 3.2). This allowed 2 cardiac cycles for the circulatory model to reach steady state, since the previous growth step alters the LV geometry. Then a 3<sup>rd</sup> cardiac cycle (step 0 in Figure 3.2), which is referred to as the “growth cycle”, is conducted for the assessment of the stimulus signal.

The growth step starts by calculating the associated time-averaged stimulus signal over the growth cycle (step 1 in Figure 3.2). Once the growth cycle reaches the end-diastolic volume, the LV geometry is unloaded back to its reference configuration (step 2 in Figure 3.2). In the next step, the local thetas ( $\theta_{local,j}$ ) are updated based on the growth stimulus (step 3 in Figure 3.2). With this approach, the growth tensor  $\mathbf{F}_g$  is referred to the most recent updated reference configuration, and correspondingly, its input parameters  $\theta_{local,j}$  were computed based on this updated configuration. Next, the LV geometry in the reference configuration grows, since  $\mathbf{F}_g$  is a non-identity tensor (step 4 in Figure 3.2). This is accomplished by solving for the elastic part of the deformation gradient  $\mathbf{F}_e$ , which is required to attain a compatible configuration in the absence of any loading on the LV (i.e., the endocardial surface is traction free). This results in a residually stressed unloaded configuration. However, in the current study we chose to alleviate this residual stress, similar to the “updated reference configuration approach” described in our previous work [65]. This was accomplished by updating the nodal positions of the reference configuration to match those of the nodes displaced during the growth step (step 5-1 in Figure 3.2). Once the updated reference configuration is established the global theta value is calculated (step 5-2 in Figure 3.2). Finally, the new reference configuration for the LV geometry is reloaded back to the prescribed end-diastolic volume (step 6 in Figure 3.2), which conserves total blood volume in the system, and continues the normal elastic deformation until the next growth cycle (i.e. n+1) starts.

The weak formulation of the growth mechanics problem was obtained using FE method by solving the following equation for  $\mathbf{u} \in H^1(\Omega_0)$  and  $p \in H^1(\Omega_0)$  such that

$$\begin{aligned}
\delta \mathcal{L}_G = & \int_{\Omega_0} (\mathbf{FS} - \mathbf{JF}^{-T}) : \nabla \delta \mathbf{u} dV - \int_{\Omega_0} (\delta p (J - 1)) dV - \delta c_x \cdot \int_{\Omega_0} u_x dV - c_x \cdot \int_{\Omega_0} \delta u_x dV - \\
& \delta c_y \cdot \int_{\Omega_0} u_y dV - c_y \cdot \int_{\Omega_0} \delta u_y dV - \delta c_z \cdot \int_{\Omega_0} \mathbf{z} \times \mathbf{u} dV - c_z \cdot \int_{\Omega_0} \mathbf{z} \times \delta \mathbf{u} dV = 0
\end{aligned} \tag{4.16}$$

In the equation above,  $\mathbf{F}$  is the deformation gradient tensor described in equation (4.11),  $\mathbf{S}$  is the 2<sup>nd</sup> Piola Kirchhoff stress tensor which does not include the active stress (i.e.  $\mathbf{S} = \mathbf{S}_p$ ),  $\delta \mathbf{u} \in H^1(\Omega_0)$ ,  $\delta p \in H^1(\Omega_0)$ ,  $\delta c_x \in R$ ,  $\delta c_y \in R$ , and  $\delta c_z \in R$  are test function corresponding to  $\mathbf{u}$ ,  $p$ ,  $c_x$ ,  $c_y$ , and  $c_z$  respectively. Similar to the elastic deformation, the displacement field  $\mathbf{u}$  was approximated using a quadratic tetrahedral element formulation, whereas a linear element formulation was used for Lagrange multiplier  $p$ .



#### **4.2.8 Clinical data**

To validate our model, clinical data for patients with different severity levels of valvular diseases and volunteer control groups were collected from the literature, which was acquired by cardiac magnetic resonance imaging (Table 4.1). Clinical data were categorized into three groups labeled “Control volunteers”, “Patients with aortic stenosis”, and “Patients with mitral regurgitation”. For each category, measured data for left ventricular end-diastolic volume index (LVEDVi), left ventricular end-systolic volume index (LVESVi), and left ventricular mass index (LVMi) normalized by the body surface area were collected from eight different studies.

**Table 4.1 Utilized studies for collecting clinical data**

Control volunteers			Patients with aortic stenosis			Patients with mitral regurgitation		
Study	Year	n	Study	Year	n	Study	Year	n
Lee et al. [192]	2020	30	Lee et al. [192]	2020	191	Liu et al. [193]	2020	104
Spath et al. [176]	2019	41	Everett et al. [175]	2020	440	Seldrum et al. [181]	2019	59
Seldrum et al. [181]	2019	30	Spath et al. [176]	2019	159	Bakkestrom et al. [187]	2018	46
Lee et al. [194]	2015	15	Singh et al. [189]	2019	174	Polte et al. [195]	2017	40
Edwards et al. [179]	2014	35	Everett et al. [196]	2018	61	Myerson et al. [188]	2016	152
Chin et al. [172]	2014	33	Chin et al. [172]	2014	133	Edwards et al. [179]	2014	35
Barone-Rochette et al. [182]	2013	20	Barone-Rochette et al. [182]	2013	128	Schiros et al. [180]	2012	94
Schiros et al. [180]	2012	51	Steadman et al. [197]	2012	41	Uretsky et al. [198]	2010	23
Data were reported as mean $\pm$ standard deviation (SD) or median (interquartile range). n is number of studied patients.								

## 4.2.9 Simulation cases

### 4.2.9.1 Baseline

All simulations started with default parameters to represent the cardiovascular function of healthy adults with normal characteristics as reported in the literature [170, 171]. For example, the total blood volume of the systemic circulation system was set to 4.5

liters such that when the system reaches to steady state the LV ejects 74 ml of blood with heart rate of 60 beats per minute and ejection fraction of 65%.

#### 4.2.9.2 Aortic Stenosis (AS)

According to the *Poiseuille's* law, the resistance of flow across the aortic valve is proportional to one over the valve cross-sectional area squared. Therefore, the stenotic aortic valve was modeled by increasing the aortic valve resistance ( $R_{aorta}$ ) in (4.2). In this study, two levels of severity for aortic stenosis were modeled to represents patients with progressive AS and asymptomatic severe AS according to the American Heart Association (AHA) guidelines [149]. For instance, to mimic a patient with asymptomatic severe AS there is a ~65 % reduction in the aortic valve area, from a mean value of 2.5 cm<sup>2</sup> for healthy adults [172-174] to a mean value of 0.86 cm<sup>2</sup> [175, 176], we increased the aortic resistance in our model by 750 %. This was mimicked in the current work by increasing the valve resistance from a baseline value of 20 (mmHg L<sup>-1</sup>) to 170 (mmHg L<sup>-1</sup>). All simulated cases for aortic stenosis are summarized in Table 4.2.

**Table 4.2 Simulated levels of severity for aortic stenosis (AS).**

$R_{aorta}$ (mmHg L <sup>-1</sup> )	Equivalent % reduction in aortic valve area	Represented stage of disease according to AHA guidelines [149]
70	46.55 (From 2.50 cm <sup>2</sup> to 1.33 cm <sup>2</sup> )	At risk of AS / Progressive AS
170	65 (From 2.50 cm <sup>2</sup> to 0.86 cm <sup>2</sup> )	Asymptomatic severe AS

#### 4.2.9.3 Mitral Regurgitation (MR)

Mitral regurgitation was simulated by assigning a positive value to  $G_{MV}$  in equation (4.2), which allows blood to leak backward through the mitral valve during systole. In the

current study, two levels of severity were selected to simulate patients with progressive and symptomatic severe MR. Selected values for  $G_{MV}$  and their corresponding regurgitant volume are summarized in Table 4.3.

**Table 4.3 Simulated different levels of severity for mitral regurgitation (MR).**

$G_{MV}$ (L mmHg <sup>-1</sup> s <sup>-1</sup> )	Equivalent regurgitant volume (ml beat <sup>-1</sup> )	Represented stage of disease according to AHA guidelines [149]
1e-3	30	At risk of / Progressive MR
3e-3	70	Symptomatic severe MR

## 4.3 Results

### 4.3.1 Concentric growth in response to pressure overloading

Figure 4.2 illustrates the thickening of the LV in response to simulated levels of aortic stenosis according to Table 4.2. Both simulations started with identical default parameters and were allowed to reach to initial steady state while arterial pressure was maintained at  $P_{set} = 90$  mmHg by the baroreflex algorithm. In response to the mimicked “progressive AS” case, the growth algorithm increased  $\theta_{global,s_0}$  and  $\theta_{global,n_0}$  by an average of ~6% across the geometry, while they were increased by ~16% for the severe case. As a result, the myocardial volume for the severe case increased by roughly 19% more (178.9 ml vs 152 ml) than the progressive case, which resulted in more wall thickening for the unloaded geometry as is shown in Figure 4.2.a.

Regarding the chamber volume, for the severe case the end-diastolic volume increased by 6% while for the other case it increased by 1% relative to baseline. The end-systolic volume had a larger change, as it was increased by approximately 7% and 29% for the progressive and severe cases, respectively. This change in the chamber volume was also observed in stroke volume, as it was decreased by 6% for the severe case versus 2% for the other case. Consequently, the ejection fraction for the severe case was depressed by 12% whereas for the progressive case it was only reduced by 3%. Throughout both simulations, arterial pressure was maintained at the setpoint level by increasing heart rate, vascular tone, intracellular  $Ca^{2+}$  handling, and contractility of the myofilaments. Although the severe case reduced the stroke volume, the increase in heart rate by the baroreflex preserved the cardiac output for both cases, at roughly  $4.3 \text{ L min}^{-1}$ .

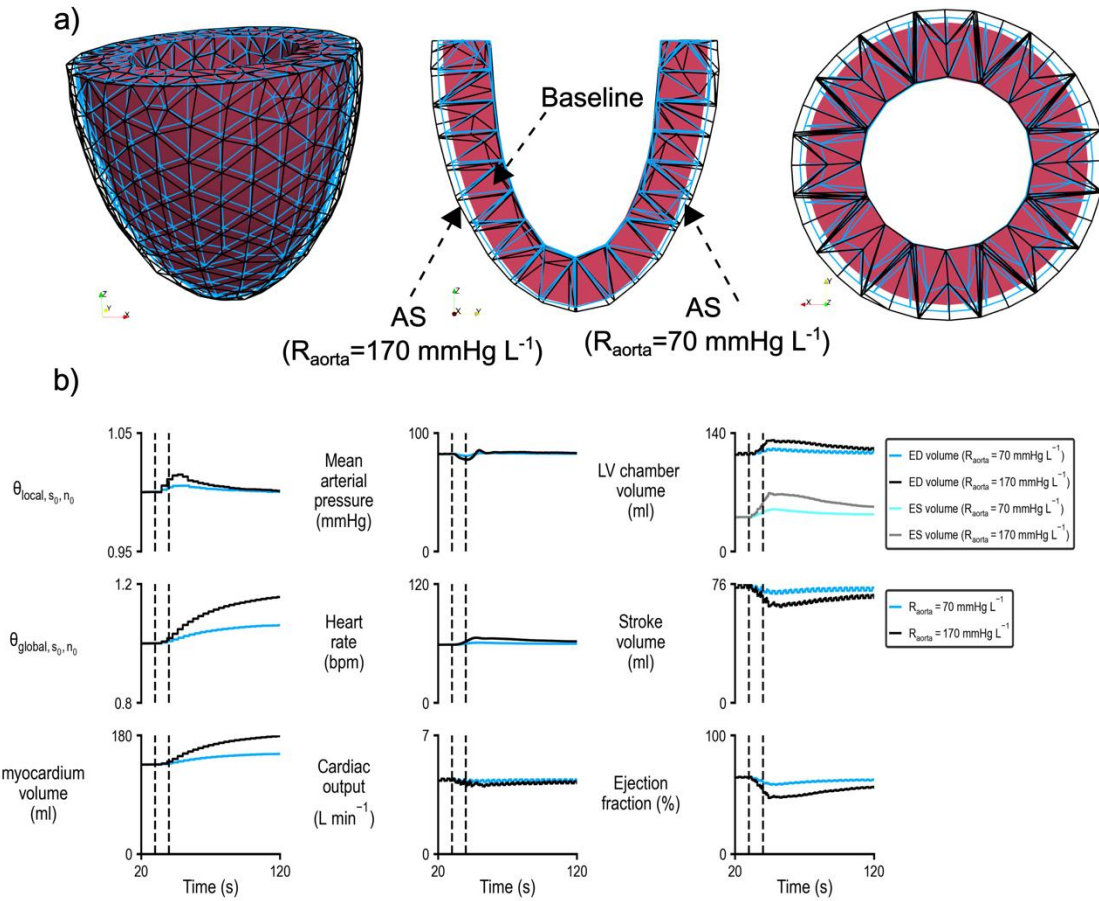


**Figure 4.2 Growth algorithm predicted more hypertrophy (wall thickening) in response to higher pressure overloading.**

a) Geometrical change in the unloaded left ventricle due to pressure overloading. b) Multipanel illustration of results for two levels of aortic stenosis. Two simulations of aortic stenosis (pressure overloading) with different severities were started with identical default parameters. For both simulations,  $R_{aorta}$  increased between 30 s and 40 s shown by vertical dashed lines.  $\theta_{local,s_0,n_0}$  is the local growth multiplier along sheet and sheet-normal directions,  $\theta_{global,s_0,n_0}$  is the global growth multiplier along sheet and sheet-normal directions.

### 4.3.2 Eccentric growth in response to volume overloading

Figure 4.3 depicts the model response to two levels of severity for volume overloading described in Table 4.3 by mimicking mitral regurgitation. Both simulations started with identical conditions as before. As shown in Figure 4.3, the growth algorithm increased  $\theta_{global, f_0}$  by approximately 23% and 38% for the progressive and severe cases, respectively. This subsequently led to growth of myocardial wall volume along myofiber direction by 32% for the severe case versus 18% for the progressive mitral regurgitation. Growth of myocytes along the local myofiber direction resulted in the dilation of the LV chamber. For the severe MR case, chamber volume increased by 94% and 130% at end-diastole and end-systole, respectively. In contrast, for progressive MR the chamber volume dilated only by 36% at end-diastole and 40% at end-systole. The higher regurgitant volume also resulted in more reduction in forward stroke volume (18% for the severe case vs. 2% for the progressive case) and more drop in ejection fraction (58% for the severe case versus 29% for the progressive case).

For the progressive MR simulation, the dilation of the chamber volume nearly restored the forward stroke volume and subsequently arterial pressure, which led to a subtle change by the parameters controlled by the baroreflex (e.g. heart rate increased by 3%). However, for the severe case, excessive dilation of the chamber volume could not recover the stroke volume, and thus arterial pressure was maintained at the setpoint level by further increasing the controlled parameters, i.e., heart rate increased by 13%. This combination of changes in forward stroke volume and heart rate resulted in only a 0.5% decrease of cardiac output for progressive MR, whereas for the severe case it reduced by 8%.

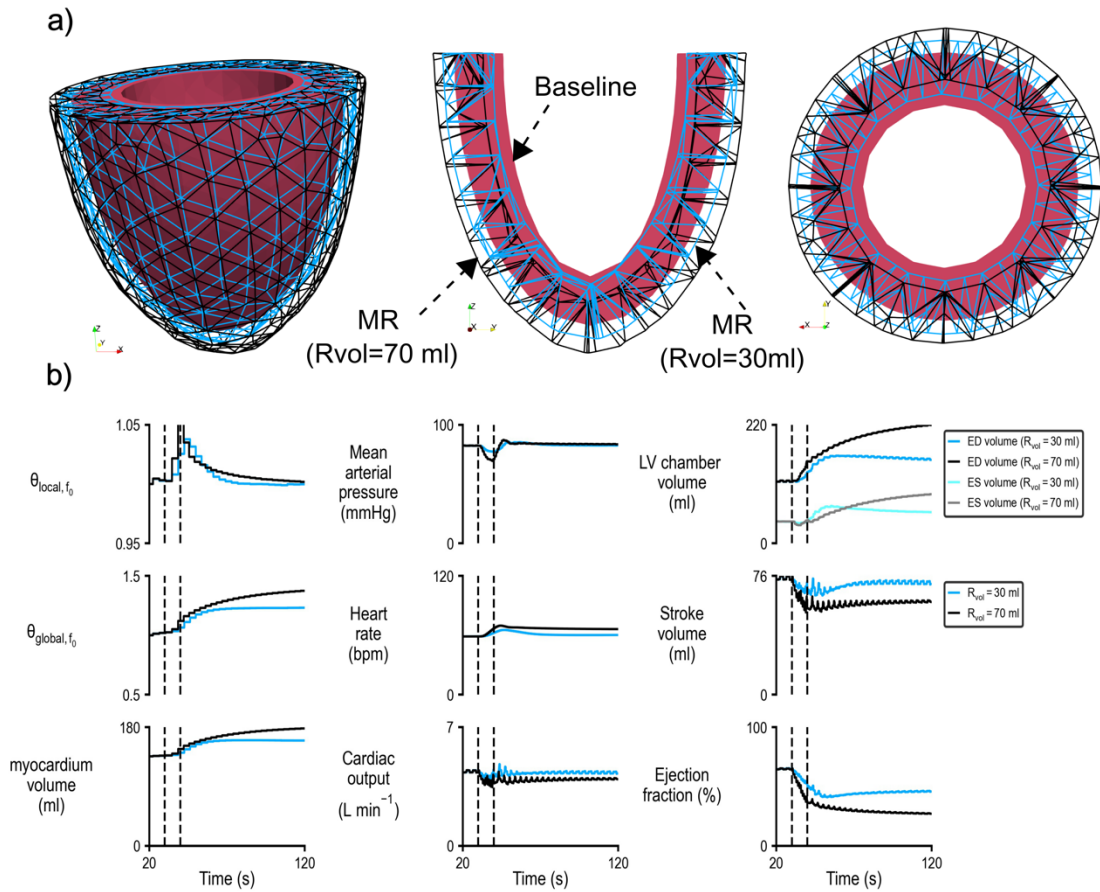


**Figure 4.3 Growth algorithm predicted more dilation in response to higher volume overloading.** a) Geometrical change in the unloaded left ventricle due to volume overloading. b) Multipanel illustration of results for two simulations of mitral regurgitation. Two levels of severity for volume overloading were started with identical default parameters. For both simulations,  $G_{MV}$  increased between 30 s and 40 s shown by vertical dashed lines.  $\theta_{local,f_0}$  is the local growth multiplier along myofiber direction,  $\theta_{global,f_0}$  is the global growth multiplier along myofiber direction.



### 4.3.3 Pressure-volume relationships

Figure 4.4 displays the predicted long-term changes in the pressure-volume relationship resulting from the two types of overloading with varying severities. The simulated cases for aortic stenosis exhibited higher peak systolic pressure as the severity increased. While the end-diastolic volume slightly increased, the end-systolic volume increased more, leading to a decrease in ejection fraction. Furthermore, increased aortic resistance resulted in a larger stroke work performed by the left ventricle, as represented by the enclosed area of the PV loop.

Regarding the volume overloading cases, increasing the severity led to more dilation of the left ventricular chamber volume, which shifted the PV loop rightward. Despite the peak systolic pressure remaining stable, the total stroke volume increased due to the higher retrograde blood flow through the mitral valve, resulting in more work performed by the LV. Additionally, the isovolumic contraction and relaxation phases became disrupted with increasing severity.

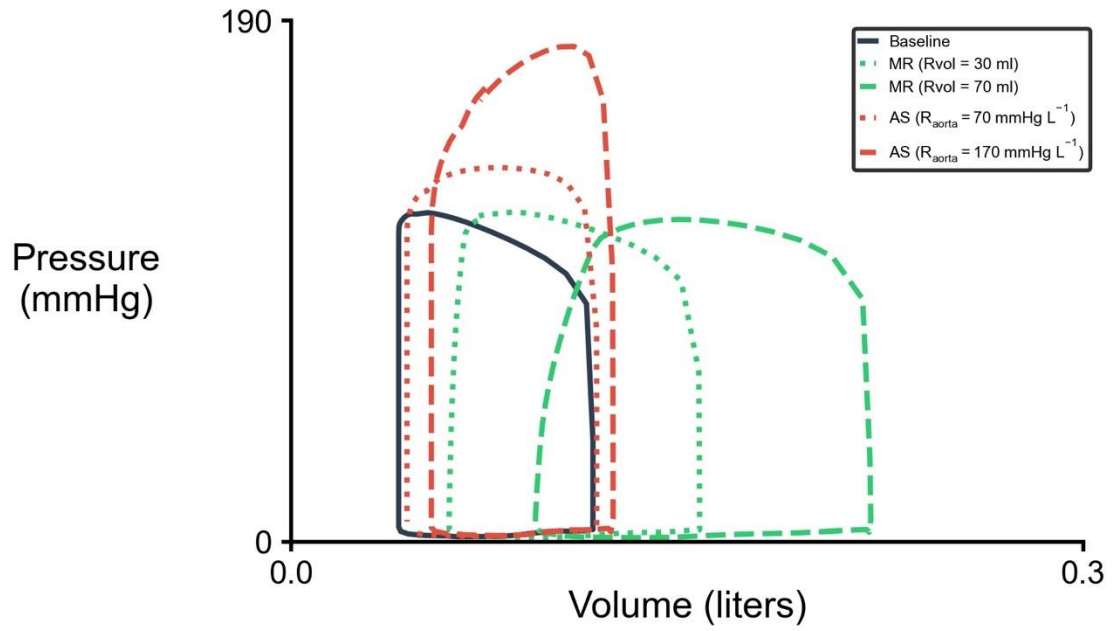


*Figure 4.4 Pressure-volume relationships in response to volume and pressure overloading.*

#### 4.3.4 Baroreflex impacted both hemodynamics and magnitude of growth

Figure 4.5 and Figure 4.6 demonstrate the impact of the baroreflex on the long-term growth of the LV in cases of severe aortic stenosis and mitral regurgitation, respectively. In the case of aortic stenosis, a higher pressure gradient across the aortic valve, resulting from elevated aortic resistance, caused a drop in mean arterial pressure by roughly 7% when the baroreflex was not taken into account. However, in the presence of the baroreflex, the mean arterial pressure remained at its setpoint level, which was done by adjusting the controlled parameters including an increase in heart rate by 7% and a decrease in venous compliance ( $C_{veins}$ ) by 15% (i.e. vasoconstriction). The adjustment in venous compliance led to a different preloading of the LV, as the mean venous pressure was 12% higher in the case with the baroreflex.

Furthermore, in the presence of the baroreflex, left ventricular volume dilated by 7% and 26% more at end diastole and end systole, respectively, compared to the non-baroreflex case. This led to a decrease in the stroke volume when the baroreflex was activated. However, the combined effects of higher heart rate, but lower stroke volume, for the baroreflex case resulted in a slightly higher cardiac output (i.e. 3%) than the non-baroreflex case.

Regarding the magnitude of growth, higher systolic arterial pressure in the case with the baroreflex led to higher afterload, and thus resulted in 5% more growth in the myocardium along the cross-sectional directions. This is depicted by slightly higher wall thickness in the unloaded geometry (Figure 4.5.a)

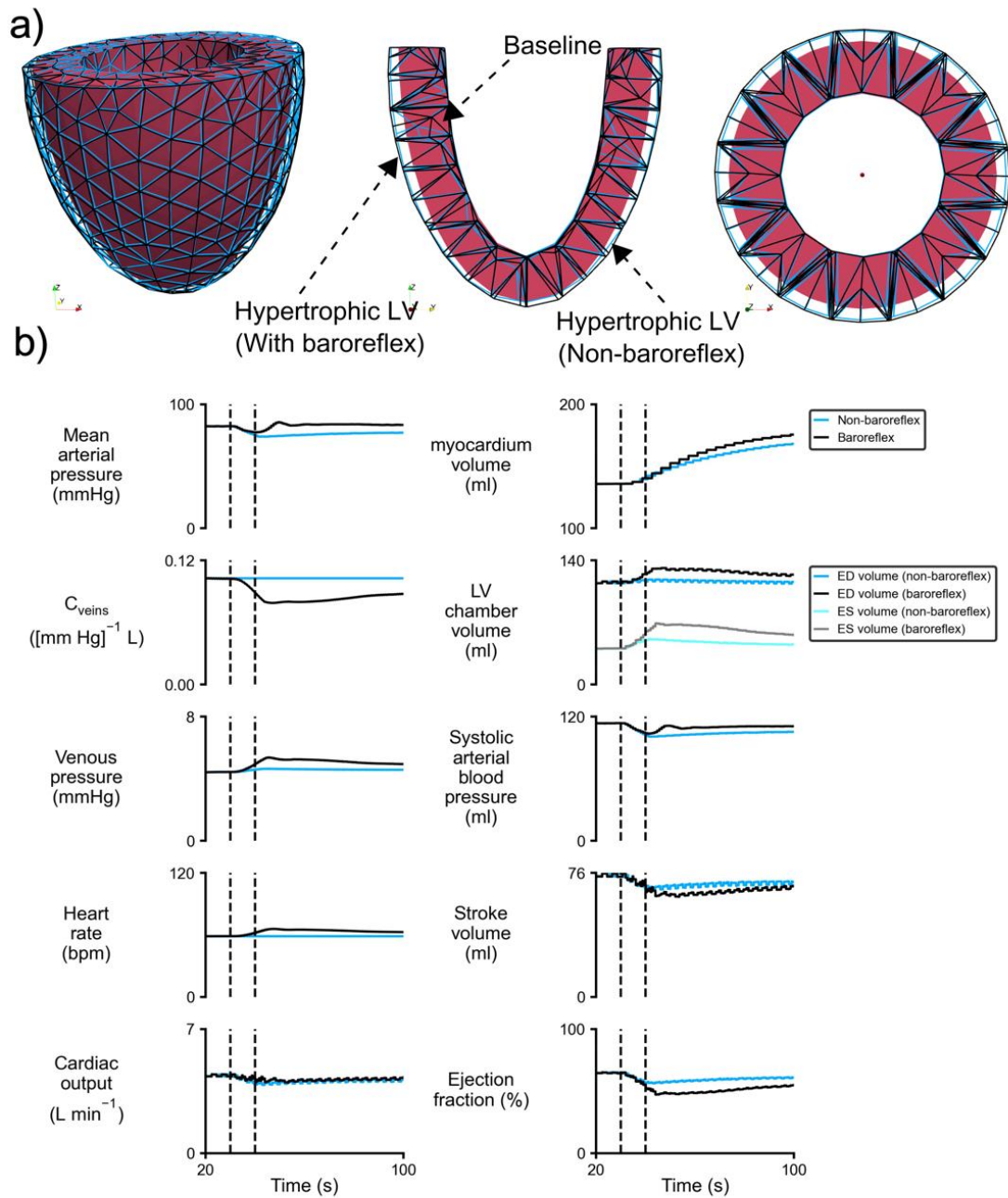


**Figure 4.5 Impact of baroreflex on capturing concentric growth.**

a) Geometrical change in the unloaded left ventricle due to pressure overloading. b) Multipanel illustration of results for two simulations of aortic stenosis. Both simulations were started with identical parameters. When both simulations reached their initial steady state, the baroreflex algorithm was deactivated for one of them, and then a similar perturbation (a 750% increase in  $R_{aorta}$ ) was applied to both cases.  $C_{veins}$  is venous compliance.

In the case of mitral regurgitation without the baroreflex, the retrograde blood flow reduced the forward stroke volume, resulting in a significant drop in mean arterial pressure by 25% (Figure 4.6) compared to the case with the baroreflex. The 27% decrease in the forward stroke volume at a constant heart rate led to a reduction in cardiac output by 27%. However, in the presence of the baroreflex, the 19% decrease in forward stroke volume was compensated by a 13% increase in heart rate, leading to only an 8% drop in cardiac output. In addition, the baroreflex algorithm adjusted the hemodynamic control parameters, such as a 24% decrease in venous compliance ( $C_{veins}$ ).

When comparing the magnitude of growth, severe MR resulted in 12% more growth of the myocardium along the myofibers in the presence of the baroreflex, which induced more dilation in the unloaded geometry (Figure 4.6.a). With the baroreflex, the left ventricular chamber volume at end-diastole dilated 44% more than the non-baroreflex case, whereas the end-systolic volume significantly increased 105% more than the case with the deactivated baroreflex. Ultimately, these changes in the chamber volume resulted in 8% more drop in ejection fraction for the case with the baroreflex in comparison to the non-baroreflex case.

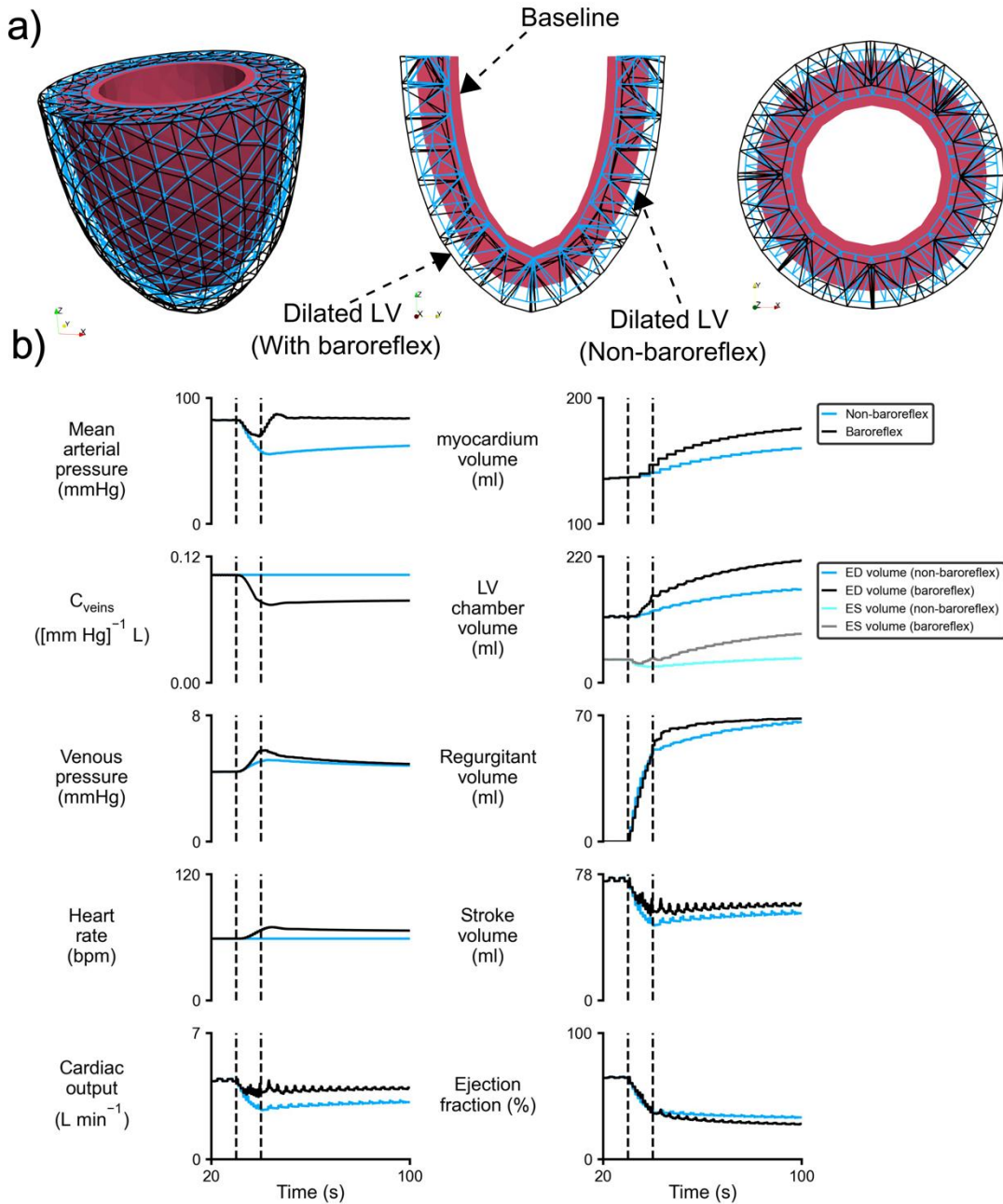


**Figure 4.6 Impact of baroreflex on eccentric growth.**

a) Geometrical change in the unloaded left ventricle due to volume overloading. b) Multipanel illustration of results for two simulations of mitral regurgitation. Both simulations started with identical parameters. After reaching the initial steady state, the baroreflex algorithm was deactivated for one of the simulations, and a similar regurgitant volume (i.e.,  $R_{vol} = 70 \text{ ml}$ ) was induced in both cases.  $C_{veins}$  is venous compliance.

#### **4.3.5 The coupled baroreflex-growth model reproduced left ventricular characteristics measured in clinical data**

To validate the model, predicted left ventricular dimensions were first normalized by an average body surface area of  $1.9 \text{ m}^2$  [199, 200]. These values were then compared to the data collected from the literature listed in Table 4.1. Figure 4.7 summarizes the model predictions for left ventricular dimension characteristics compared to the measured values from the literature. In the case of aortic stenosis (left-hand column in Figure 4.7), clinical data did not report any change in left ventricular volume from “Control” to “Patient” group, and this was captured by the model as the predicted values were in the reported range. Similarly, the current model predicted larger mass for the left ventricle as the disease severity increased, which matched with the reported range. For mitral regurgitation, the model predicted a larger left ventricular volume and mass, and for both severity levels, which were within the reported range of the clinical data.

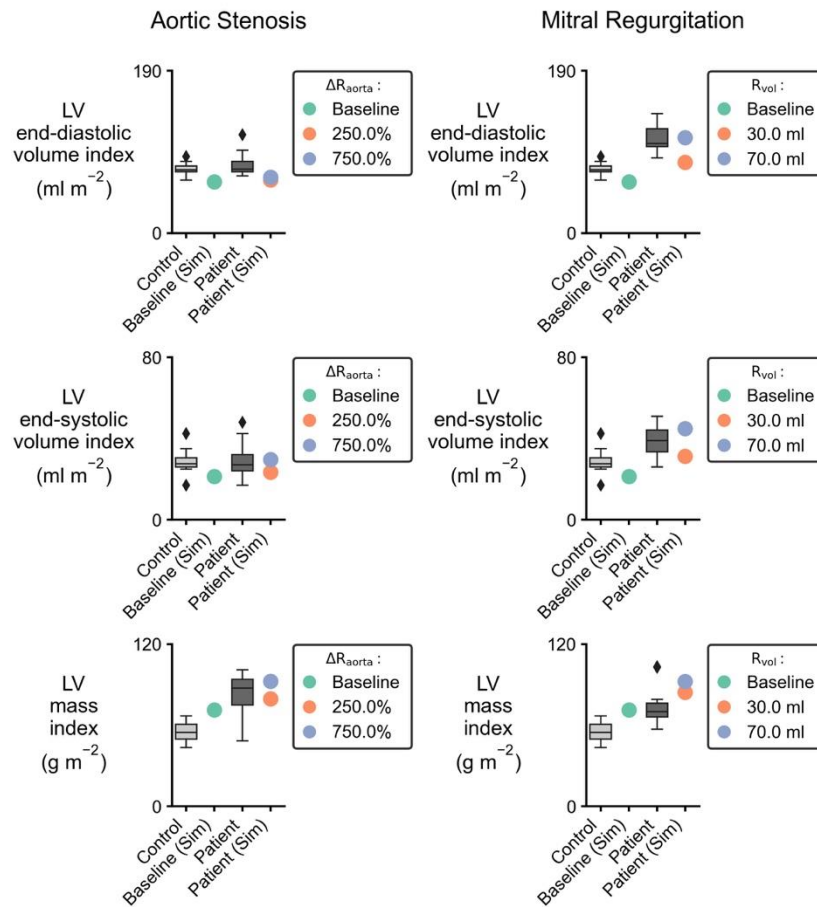


**Figure 4.7 Model validation with measured clinical data.**

Each column summarizes the model validation for a particular valvular disease (left, Aortic stenosis; right, Mitral regurgitation). In all panels, interquartile ranges for clinical data are shown with box plots in two groups of “Control” and “Patient”, whereas simulation results are shown with circle markers in two groups of “Baseline (Sim)” and “Patient (Sim)”. LV end-diastolic volume index: LV end-diastolic volume normalized by the body surface area, LV end-systolic volume index: LV end-systolic volume normalized by the body surface area, LV mass index: LV myocardium mass normalized by the body surface area.  $\Delta R_{aorta}$ : change in aortic resistance from baseline,  $R_{vol}$ : Regurgitant volume through mitral valve.



## **4.4 Discussion**

### **4.4.1 Overview**

The current approach extends the capabilities of a high-fidelity computational model of the cardiovascular system by incorporating a baroreflex feedback loop and a growth algorithm. The goal of this extension was to capture both the short-term and long-term response of the heart in simulations of valve disease. The results of this work demonstrate that the combined framework can model the long-term growth in response to two types of valve disease, aortic stenosis and mitral regurgitation, at two levels of severity. In addition, the baroreflex algorithm was able to maintain arterial pressure during the process of left ventricular growth. Lastly, the model could reproduce clinical characteristics of measured left ventricular dimension.

### **4.4.2 Capturing various timescales**

The extended model presented in this study benefits from the use of both feedback loops in simulations of valve diseases, and it highlights the importance of incorporating a baroreflex loop in simulations of left ventricular growth. Our previous studies illustrated in CHAPTER 2 and [138] have demonstrated the effectiveness of the implemented baroreflex loop in maintaining arterial pressure under different types of disease-mimicking perturbations such as acute valvular perturbations and myocardial infarction. Additionally, in CHAPTER 3, we showed that the growth algorithm alone can accurately capture the correct form of growth when the left ventricle is either pressure or volume overloaded.

In vivo, the hemodynamic reflex and growth feedback loops are the two mechanisms that work together to respond to alterations in left ventricular loading, but over

different timescales. The hemodynamic reflex, known as the baroreflex, is primarily responsible for the first-order short-term response of the heart to maintain its functionality in ejecting enough oxygenated blood to the rest of the body [201]. The growth mechanism, on the other hand, serves as a second-order long-term [65, 68] response that attempts to improve the pumping function of the heart by altering its geometry to compensate for the altered stress state that myocytes sense at the molecular level.

Therefore, combining the effect of these two mechanisms in simulations of valvular diseases is crucial. In our model, we selected the rate factors,  $k_{drive}$  in equation (4.8) and  $k_{control,i}$  in equation (4.9), of the baroreflex algorithm based on two considerations. First, we ensured that they were sufficiently large to enable smooth adjustments of the controlled parameters without inducing any instability in the execution of the finite element code. Second, we ensured that they were small enough to facilitate the quick restoration of arterial pressure over several cardiac cycles when the system is challenged.

In contrast, we selected the growth rate factors  $\tau_{fg,j}$  and  $\tau_{rg,j}$  in equation (4.13) such that left ventricular growth could occur with sufficient speed. However, we also introduced a separation of timescales between growth and elastic deformation, as described in the "Methods" section, to capture the full progression of growth. As a result, in our current work, the baroreflex algorithm responds to the disease-mimicking perturbation to maintain arterial pressure prior to the response of the growth algorithm, which takes place over a larger number of cardiac cycles. This feature replicates the physiological order of these mechanisms observed in vivo, as well as in other computational models [73], and highlights the fidelity of our approach.

### 4.4.3 Importance of baroreflex in simulations of LV growth

The incorporation of the baroreflex feedback loop in our current study has yielded several advantages in simulations of left ventricular growth. Firstly, the inclusion of the baroreflex feedback resulted in more physiologically realistic hemodynamics for simulating pressure and volume overloading (Figure 4.5 and Figure 4.6), as reported in the literature. For example, previous studies have demonstrated that patients with acute mitral regurgitation [187, 188] or aortic stenosis [104, 189] typically exhibit mean arterial pressures of approximately 90 mmHg with a cardiac output of 4 - 5 L min<sup>-1</sup>. Our model predictions were consistent with these reported clinical data, as the arterial pressure setpoint was assigned to be maintained at 90 mmHg and the ellipsoidal left ventricle produced a cardiac output of roughly 4.4 and 4.3 L min<sup>-1</sup> for simulated mitral regurgitation and aortic stenosis cases, respectively. Conversely, simulations without the baroreflex feedback loop resulted in non-physiological hemodynamics, as observed in CHAPTER 3 as well as other studies [40, 63], when acute valvular diseases were induced to challenge the model. In particular, our model led to 7% and 3.5% drop in mean arterial pressure and cardiac outputs, respectively, when aortic resistance was acutely increased from 20 to 170 mmHg L<sup>-1</sup>. These results were aligned with Rondanina and Bovendeerd's work [40], where their model predicted roughly 10% reduction in mean arterial pressure and cardiac output when using a unified stress-driven growth law for their simulation of acute aortic stenosis. For the non-baroreflex mitral regurgitation case, our model resulted in a 25% reduction in mean arterial pressure and a 27% reduction in cardiac output which were in the same reported range by Rondanina and Bovendeerd when using unified stress-driven growth law.

Secondly, the presence of the baroreflex feedback loop in our model also had an impact on the magnitude of predicted left ventricular growth. In the severe pressure overloading case (as shown in Figure 4.5), the absence of the baroreflex feedback loop led to 5% less growth in the myocardium along cross-fiber directions, compared to the case with baroreflex. This was mainly due to the fact that in the non-baroreflex case, the mean arterial pressure dropped to a lower level of 77 mmHg, while in the other case it remained at the baseline level. Consequently, the LV had to eject blood against a relatively lower afterload in the non-baroreflex case, which resulted in a lower time-averaged total stress in the LV wall over the cardiac cycle and subsequently less growth. Moreover, the current model captured an increase in LV end-systolic volume (Figure 4.5) and a rightward shift in the PV loop (Figure 4.4) in the presence of the baroreflex. Similar findings were also observed in Nicks et al.'s work [202] where they reported following acute aortic banding in mice, LV end-systolic volume and LV end-diastolic pressure increased compared to sham group. Based on our results, this could be associated with the regulation of venous compliance by baroreflex feedback loop to restore arterial pressure. In particular, the baroreflex algorithm in our model decreased venous compliance immediately after inducing aortic stenosis to mimic vasoconstriction, which led to higher venous pressure as shown in Figure 4.4. Subsequently, this resulted in more filling of LV during diastole and rightward shift of PV loop.

Moreover, the baroreflex had a notable impact on the magnitude of eccentric growth for the severe mitral regurgitant case, where the growth algorithm predicted 12% more growth in the presence of the baroreflex loop compared to the non-baroreflex case (Figure 4.6). Furthermore, incorporating the effects of the baroreflex led to 44% and 105%

more dilation of the LV volume at end-diastole and end-systole, respectively, which were fully aligned with the reported range for clinical data shown in Figure 4.7. Similarly, this could be explained by the role of baroreflex regulation of venous compliance. Essentially, when the retrograde blood flow through the mitral valve was induced, arterial pressure started to decrease as forward stroke volume was depressed. The immediate response of the baroreflex feedback loop to such a condition was to maintain arterial pressure by adjusting various controlled parameters, including heart rate and venous compliance. The baroreflex algorithm in the current model essentially controls the venous compliance such that when arterial pressure falls below its homeostatic level, the venous compliance decreases (CHAPTER 2, [138]) to mimic vasoconstriction [159, 201] (as shown in Figure 4.6). This event directly increases venous pressure and results in more filling of the LV with blood during diastole, which in turn can improve the ejection of blood based on the Frank-Starling effect. The increased filling of the LV results in excessive stretch of the myofibers, which is significantly greater than the overstretching of the myofibers due solely to the volume overloading in the non-baroreflex case. Since the higher stretch in the myofibers is associated with higher time-averaged passive stress, which is the stimulus signal for eccentric growth of myofibers in our model, this leads to more growth.

Taken together, these observations suggest the importance of the baroreflex in simulations of left ventricular growth, as other groups have also emphasized. For example, Rondanina and Bovendeerd [73] in their recent work investigated cardiac growth and circulatory adaption in three simulations of valve disease. They showed that incorporating a simplified hemodynamic adaption model, which could only regulate peripheral resistance and stressed blood volume, resulted into more realistic hemodynamics in simulations of

valve diseases. Regarding the impact of the reflex on their cardiac growth prediction, they reported that although the reflex improved the prediction of relative wall thickness in aortic stenosis simulations, it worsened the prediction of mass index for mitral regurgitation using a mixed stress-strain growth law that had already showed promising results for cardiac growth. In another study, Witzenburg and Holmes [159] investigated how the hemodynamic reflex affects cardiac growth predictions after myocardial infarction. Although they did not explicitly implement a reflex mechanism in their cardiac growth model, they showed variability in regulation of certain parameters by a hemodynamic reflex can impact the prediction of LV dilation post-MI, particularly those with a moderately sized infarct. They also noted that for simulations with very large infarcts, vasoconstriction had a dominant impact on the degree of LV dilation, which aligns with our own findings.

Another approach to mitigating the negative impact of not incorporating a hemodynamic reflex loop in models of cardiac growth has been to adjust certain parameters to assume preserved loading of the left ventricle throughout the simulation. For instance, Yoshida et al. [70] manually adjusted aortic resistance, stressed blood volume, and maximum myocardial stress to match reported hemodynamics in their simulations of acute pressure overloading. Similarly, Arumugam et al. [68] assumed constant preload and afterload throughout their simulations of anisotropic reverse cardiac growth in mechanical dyssynchrony. Although these adjustments may allow for more accurate hemodynamic modeling, they do not capture the dynamic regulation of loading that occurs through the hemodynamic reflex, and thus may not fully capture the complexity of cardiac growth and adaptation.

## 4.5 Limitations

While this model addressed one of the limitations of previous work described in CHAPTER 3 by adding the baroreflex feedback loop to maintain arterial pressure and have a more realistic hemodynamics, other limitations are still applicable to this model.

The first limitation is that the current model employs a generic ellipsoidal model of the left ventricle instead of a patient-specific model of the LV. Although this model is intended to serve as a proof of concept, using a patient-specific LV geometry along with measured characteristics such as blood pressure and LV dimensions could lead to a higher level of model validation in simulations of left-ventricular growth for patients with valvular disease.

Secondly, the control system of the baroreflex loop implemented in this study was not calibrated using patient data, as the study lacks the benefits of utilizing a patient-specific model. Here, we assumed that all parameters controlled by the baroreflex are adjusted with similar rate factors. However, in vivo this could vary among different patients. Capturing these details of the baroreflex loop was beyond the scope of this study, as it was only intended to preserve the loading of the LV during cardiac growth.

Lastly, this study did not model the material remodeling that might occur due to fibrosis, particularly under pressure overloading conditions. To tackle this limitation, other approaches can be used to implement tissue growth, such as the constrained mixture theory. This theory assumes that different tissue constituents (cells, collagen, elastin, etc.) have distinct production/turnover rates and are constrained to deform within a single continuum mixture. However, these methods are highly computationally expensive and have mainly

been used for arterial growth and remodeling, assuming simple 2D geometry, such as a thin-wall membrane [80, 82].

#### **4.6 Summary and conclusion**

This study incorporates two types of feedback loops that respond to alterations in left ventricular loading, but operate over different time scales. The first loop is called the baroreflex, which is primarily responsible for the short-term response of the heart to maintain its functionality in ejecting enough oxygenated blood to the rest of the body. The growth mechanism, on the other hand, serves as a long-term response that attempts to improve the pumping function of the heart by changing its geometry to compensate for the altered stress state that sarcomeres sense at the molecular level. Our integrated model reproduced clinical measures of LV growth in two types of valvular disease, namely aortic stenosis and mitral regurgitation, with two different levels of severity for each case. Furthermore, the results of this study showed that incorporating the effects of baroreflex control of arterial pressure in simulations of left ventricular growth not only led to more realistic hemodynamics, but also impacted the magnitude of growth. In particular, our results emphasized that the regulation of venous compliance (vasoconstriction) by baroreflex immediately after the onset of valvular diseases has a significant role on the extent of LV growth in the long term.



## 5.1 Summary of CHAPTER 1

Cardiomyocytes can adapt their size and shape in response to altered biomechanical stimuli under a mechanism which is broadly known as cardiac growth and remodeling (G&R). Although it is likely that cardiac G&R initially occurs as an adaptive response of the heart to the underlying stimuli, prolonged pathological changes can lead to increased risk of atrial fibrillation, heart failure, and sudden death. Computational models of the left ventricular growth have been emerging as effective tools for investigating the mechanisms that drive ventricular growth and remodeling. Such models can be used to evaluate the effects of molecular-level mechanisms on organ-level function, which could provide new insights for improving patient care. These models have provided an opportunity to quantitatively study the relationships between the underlying stimuli (primarily mechanical) and the adverse outcomes of cardiac G&R, i.e., alterations in ventricular size and function. State of the art computational models have shown promise in predicting the progression of cardiac G&R. However, there are still limitations that need to be addressed in future works to advance the field.

The first step towards improving the current state of existing models of LV growth was to do a thorough literature review. In CHAPTER 1 we summarized the current state of computational models of cardiac growth. In general, the majority of current models are based on volumetric growth theory which was initially demonstrated by Rodriguez et. al [38]. Then, the potential limitations of current models of cardiac G&R that need to be addressed before they can be utilized in clinical care were illustrated. These limitations were 1) lack of mechanistic contractile model of the heart, 2) lack of hemodynamic

feedback control, 3) inability of capturing the reversal of growth, 4) inability of applying computer models of cardiac G&R to the clinical care, and 5) complexity of model calibration and validation. Finally, the next feasible steps and future directions that could advance the field of cardiac G&R were described.

## **5.2 Summary of CHAPTER 2**

CHAPTER 2 tried to address two limitations of current computational models of cardiac G&R including 1) lack of mechanistic contractile model of the heart and 2) lack of hemodynamic feedback control, which were noted in CHAPTER 1. In this chapter, a new multiscale model of the cardiovascular system named MyoFE was presented, which incorporated a mechanistic model of contraction at the myosin level into a finite-element-based model of the left ventricle pumping blood through the systemic circulation. The model was coupled with a closed-loop feedback control of arterial pressure inspired by an algorithm previously published by our team. The reflex loop mimicked the afferent neuron pathway via a normalized afferent signal derived from arterial pressure. The efferent pathway was represented by a kinetic model that simulates the net result of neural processing in the medulla and cell-level responses to autonomic drive. The control algorithm modulated not only parameters such as heart rate and vascular tone of vessels in the lumped-parameter model of systemic circulation, but also spatially modulated intracellular  $\text{Ca}^{2+}$  dynamics and molecular-level function of both the thick and the thin myofilaments across the 3D geometry of the left ventricle. Results in CHAPTER 2 demonstrated that the baroreflex algorithm can regulate arterial pressure at different user-defined setpoints. In addition, arterial pressure was maintained in the presence of perturbations such as acute cases of aortic stenosis, mitral regurgitation, and myocardial

infarction. The illustrated capabilities of this new multiscale model were crucial for research related to computational investigations of growth and remodeling that were described in the following chapters of this dissertation.

### **5.3 Summary of CHAPTER 3**

In CHAPTER 3, the central framework of MyoFE illustrated in CHAPTER 2 was extended via a growth algorithm, based on volumetric growth theory, to simulate concentric growth (wall thickening / thinning) and eccentric growth (chamber dilation / constriction) in response to valvular diseases. Specifically in this extended model, concentric growth was controlled by time-averaged total stress along the fiber direction over a cardiac cycle while eccentric growth responded to time-averaged intracellular myofiber passive stress over a cardiac cycle. The new framework appropriately predicted two different forms of growth in response to two types of valvular disease, namely aortic stenosis and mitral regurgitation. Furthermore, simulations for each valvular disorder regained LV size and function (reversal of growth) when the disease-mimicking perturbation was removed. In conclusion, the illustrated results in CHAPTER 3 suggested that time-averaged total stress along the fiber direction over a cardiac cycle and time-averaged intracellular myofiber passive stress can be used to drive concentric and eccentric growth, respectively, in simulations of valve disease.

### **5.4 Summary of CHAPTER 4**

The heart functions within a complex system that adapts its function to alterations in loading via several mechanisms. For example, the baroreflex is a short-term feedback loop that modulates the heart's function on a beat-to-beat basis to control arterial pressure.

On the other hand, cardiac growth is a long-term adaptive response that occurs over weeks or months in response to changes in left ventricular loading. In CHAPTER 4, the impact of a baroreflex feedback loop on left ventricular growth in simulations of valve diseases was investigated. To achieve this purpose, the effects of a short-term baroreflex feedback loop that was described in CHAPTER 2 were coupled with a long-term growth algorithm (demonstrated in CHAPTER 3) using the MyoFE multiscale finite element model of the left ventricle. The baroreflex loop modulated the system from the molecular-level function of myofilaments up to system-level parameters such as heart rate to control arterial pressure. Meanwhile, the growth algorithm responded to the altered stress level of the myofibers to drive long-term changes in the geometry of the left ventricle.

The integrated model replicated clinical measures of left ventricular growth in two types of valvular diseases - aortic stenosis and mitral regurgitation - at two different levels of severity for each case. Furthermore, the results showed that incorporating the effects of baroreflex control in simulations of left ventricular growth not only led to more realistic hemodynamics, but also impacted the magnitude of growth. Specifically, the results demonstrated in CHAPTER 4 highlighted the significant role of regulating venous compliance (vasoconstriction) by the baroreflex immediately after the onset of valvular diseases, has on the extent of LV growth in the long term.

## **5.5 Future work**

Although the illustrated MyoFE framework in this dissertation has addressed several key limitations of existing models of cardiac G&R, the framework still requires several improvements before it can be applied to clinical care.

Firstly, as described in sections 3.5 and 4.5, the current approach uses a generic ellipsoidal 3D shape geometry of the human LV as a proof of concept. However, the framework would be more insightful if it were used to simulate a patient-specific model of LV growth. To do this, several steps need to be considered. First, a patient-specific geometry can be generated using clinical imaging data such as cardiac magnetic resonance imaging (CMRI). Then the model parameters must be calibrated to mimic the clinical characteristic of the patient. Some clinical measures can be acquired non-invasively such as chamber volumes, heart rate, arterial blood pressure, etc., but other types of characteristics, such as passive or active properties of the myocardial tissue require invasive experiments. Eventually, the calibrated model will be ready to simulate the patient-specific geometry of the heart that can be used to predict the progress of cardiac growth or evaluate different types of therapeutic interventions and assess the precise treatment.

Secondly, as briefly illustrated in 1.4.2, although a high-fidelity multiscale model of cardiac G&R can be significantly insightful, they are computationally expensive and labor intensive, which has hindered their application in clinical care [42]. Utilizing data driven models, such as machine learning techniques, to create a surrogate model of cardiac mechanics including G&R has been seen as a promising approach to overcome this drawback. Essentially, in this approach a surrogate model like Gaussian Process Emulator can be integrated with a physics-based model [203] like MyoFE to rapidly approximate a computationally expensive function of the heart, such as cardiac G&R, and evaluate the uncertainty inherent to the emulator. This surrogate model of MyoFE would be useful for

rapid calibration with available clinical data and then evaluating potential treatments of patients who suffer from dilated or hypertrophic myopathies.

Lastly, using machine learning techniques such as Gaussian Process Emulator [204] or physics-informed Neural Networks (PINN) [127], MyoFE can expand its capabilities to create a population-based virtual patient cohort of cardiac G&R. “Random variation with acceptance criteria” [205] could be an option for creating a virtual cohort of patients with cardiac G&R, especially when sufficient measurements for model parameter distributions are not available. According to this method, a virtual cohort can be created by randomly varying model parameters to generate a large number of parameter sets and then only accepting those combinations that result in physiological outcomes that fall within the inclusion/exclusion criteria. Using this large number of physics-based data, a surrogate model can be created to approximate the model function over the physiological region of parameters space and generate a cohort of patients that is statistically representative of the real population of patients. These virtual patient cohorts are particularly useful for generating in silico clinical trials that can impact the real current physical trials that are highly expensive in terms of required time and resources.

## APPENDICES

### APPENDIX 1. FILE S1

```
{
  "output_handler": {
    "mesh_object_to_save": [
      "displacement",
      "active_stress",
      "hs_length",
      "k_1",
      "k_3",
      "k_on",
      "k_act",
      "k_serca"
    ],
    "dumping_spatial_in_average": [
      true
    ],
    "output_data_path": [
      "../simulations/baro_baro_b_setpoint_-30//sim_output/data.csv"
    ],
    "mesh_output_path": [
      "../simulations/baro_baro_b_setpoint_-30//sim_output/"
    ],
    "frequency_n": [
      10
    ]
  },
}
```

```
"model": {
  "half_sarcomere": {
    "myofilaments": {
      "int_passive_1_slack": [
        850
      ],
      "k_4_1": [
        1.5
      ],
      "k_off": [
        200
      ],
      "prop_fibrosis": [
        0.0
      ],
      "ext_passive_exp_sigma": [
        100
      ],
      "k_1": [
        3
      ],
      "k_3": [
        120
      ],
      "k_2": [
        200
      ],
      "int_passive_exp_sigma": [
```



```
    100
  ],
  "k_cb": [
    0.001
  ],
  "int_passive_exp_L": [
    75
  ],
  "x_ps": [
    5
  ],
  "ext_passive_exp_L": [
    70
  ],
  "k_4_0": [
    80
  ],
  "implementation": {
    "int_passive_mode": [
      "exponential"
    ],
    "ext_passive_mode": [
      "exponential"
    ],
    "bare_zone_length": [
      80
    ],
    "bin_min": [
```

```
-10
],
"delta_G_ATP": [
    70000
],
"thick_filament_length": [
    815
],
"kinetic_scheme": [
    "3_state_with_SRX"
],
"thin_filament_length": [
    1120
],
"thick_wall_approximation": [
    true
],
"reference_hsl_0": [
    1100
],
"bin_width": [
    1
],
"max_rate": [
    2000
],
"bin_max": [
    10
```

```
],  
  "filament_compliance_factor": [  
    0.5  
  ],  
  "temperature": [  
    310  
  ]  
},  
"cb_number_density": [  
  6.9e+16  
],  
"ext_passive_l_slack": [  
  950  
],  
"k_coop": [  
  5  
],  
"k_force": [  
  0.001  
],  
"prop_myofilaments": [  
  0.6  
],  
"k_on": [  
  200000000.0  
]  
},  
"reference_hs_length": [  
  0.001  
]
```

```
    1100
  ],
  "initial_hs_length": [
    900
  ],
  "membranes": {
    "t_open": [
      0.01
    ],
    "k_act": [
      0.082
    ],
    "implementation": {
      "kinetic_scheme": [
        "simple_2_compartment"
      ]
    },
    "k_leak": [
      0.0006
    ],
    "k_serca": [
      8
    ],
    "Ca_content": [
      0.001
    ]
  }
},
```

```
"baroreflex": {
  "k_recov": [
    0.1
  ],
  "b_slope": [
    0.02
  ],
  "b_setpoint": [
    90
  ],
  "controls": {
    "control": [
      {
        "level": [
          "heart_rate"
        ],
        "k_recov": [
          0.1
        ],
        "k_drive": [
          0.03
        ],
        "symp_factor": [
          0.386
        ],
        "para_factor": [
          1.753497
        ],
      ]
    ]
  }
}
```

```
"variable": [  
  "t_quiescent_period"  
]  
},  
{  
  "level": [  
    "membranes"  
  ],  
  "k_recov": [  
    0.1  
  ],  
  "k_drive": [  
    0.03  
  ],  
  "symp_factor": [  
    3.0  
  ],  
  "para_factor": [  
    0.333  
  ],  
  "variable": [  
    "k_act"  
  ]  
},  
{  
  "level": [  
    "membranes"  
  ],
```

```
"k_recov": [  
  0.1  
],  
"k_drive": [  
  0.03  
],  
"symp_factor": [  
  3  
],  
"para_factor": [  
  0.333  
],  
"variable": [  
  "k_serca"  
]  
},  
{  
  "level": [  
    "myofilaments"  
  ],  
  "k_recov": [  
    0.1  
  ],  
  "k_drive": [  
    0.03  
  ],  
  "symp_factor": [  
    3  
  ]  
}
```

```
],
  "para_factor": [
    0.333
  ],
  "variable": [
    "k_1"
  ]
},
{
  "level": [
    "myofilaments"
  ],
  "k_recov": [
    0.1
  ],
  "k_drive": [
    0.03
  ],
  "symp_factor": [
    3
  ],
  "para_factor": [
    0.333
  ],
  "variable": [
    "k_3"
  ]
},
```



```
{
  "level": [
    "myofilaments"
  ],
  "k_recov": [
    0.1
  ],
  "k_drive": [
    0.03
  ],
  "symp_factor": [
    0.333
  ],
  "para_factor": [
    3
  ],
  "variable": [
    "k_on"
  ]
},
{
  "level": [
    "circulation"
  ],
  "k_recov": [
    0.1
  ],
  "k_drive": [
```

```
    0.03
  ],
  "symp_factor": [
    3
  ],
  "para_factor": [
    0.333
  ],
  "variable": [
    "arterioles_resistance"
  ]
},
{
  "level": [
    "circulation"
  ],
  "k_recov": [
    0.1
  ],
  "k_drive": [
    0.03
  ],
  "symp_factor": [
    0.333
  ],
  "para_factor": [
    3
  ],
  ],
```

```
        "variable": [
            "veins_compliance"
        ]
    },
    "k_drive": [
        20
    ],
    "circulation": {
        "blood_volume": [
            4.5
        ],
        "model_scheme": [
            "LV_with_6_compartments"
        ],
        "compartments": [
            {
                "slack_volume": [
                    0.3
                ],
                "compliance": [
                    0.0004
                ],
                "name": [
                    "aorta"
                ],
            }
        ],
    },

```

```
"resistance": [
  20
],
},
{
  "slack_volume": [
    0.3
  ],
  "compliance": [
    0.0008
  ],
  "name": [
    "arteries"
  ],
  "resistance": [
    20
  ]
},
{
  "slack_volume": [
    0.1
  ],
  "compliance": [
    0.001
  ],
  "name": [
    "arterioles"
  ],
  ],
```

```
"resistance": [
  1000
],
},
{
  "slack_volume": [
    0.25
  ],
  "compliance": [
    0.01
  ],
  "name": [
    "capillaries"
  ],
  "resistance": [
    350
  ]
},
{
  "slack_volume": [
    0.5
  ],
  "compliance": [
    0.03
  ],
  "name": [
    "venules"
  ],
  ],
```

```
"resistance": [
  50
],
},
{
  "inertance": [
    0
  ],
  "slack_volume": [
    2.0
  ],
  "compliance": [
    0.1
  ],
  "name": [
    "veins"
  ],
  "resistance": [
    50
  ]
},
{
  "slack_volume": [
    0.06
  ],
  "wall_density": [
    1055
  ],

```

```
        "initial_ed_volume": [
            0.15
        ],
        "name": [
            "ventricle"
        ],
        "resistance": [
            10
        ]
    }
]
}
},
"heart_rate": {
    "t_active_period": [
        0.003
    ],
    "t_first_activation": [
        0.2
    ],
    "t_quiescent_period": [
        0.92
    ]
},
"protocol": {
    "time_step": [
        0.001
    ],

```

```
"perturbation": {
  "perturbations": [
    {
      "variable": [
        "baro_b_setpoint"
      ],
      "t_stop_s": [
        40
      ],
      "total_change": [
        -30
      ],
      "t_start_s": [
        30
      ],
      "level": [
        "baroreflex"
      ]
    }
  ]
},
"no_of_time_steps": [
  80000
],
"baroreflex": {
  "activations": [
    {
      "t_stop_s": [
```



```

        400
    ],
    "t_start_s": [
        5
    ]
}
]
}
},
"mesh": {
    "solver": {
        "params": {
            "debugging_mode": [
                false
            ],
            "rel_tol": [
                1e-10
            ],
            "max_iter": [
                100
            ],
            "abs_tol": [
                1e-10
            ]
        }
    },
    "function_spaces": [
        {

```

```
"element_type": [  
  "DG"  
],  
"type": [  
  "scalar"  
],  
"name": [  
  "stimulusFS"  
],  
"degree": [  
  1  
]  
},  
{  
  "element_type": [  
    "DG"  
  ],  
  "type": [  
    "scalar"  
  ],  
  "name": [  
    "scalar"  
  ],  
  "degree": [  
    1  
  ]  
},  
{
```

```

"element_type": [
  "DG"
],
"type": [
  "tensor"
],
"name": [
  "tensor_space"
],
"degree": [
  1
]
},
{
"element_type": [
  "Quadrature"
],
"type": [
  "vector"
],
"name": [
  "material_coord_system_space"
],
"degree": [
  2
]
},
{

```

```
"element_type": [  
  "Quadrature"  
],  
"type": [  
  "scalar"  
],  
"name": [  
  "quadrature_space"  
],  
"degree": [  
  2  
]  
}  
],  
"apex_contractility": {  
  "components": [  
    {  
      "variable": [  
        "k_1"  
      ],  
      "factor": [  
        1  
      ],  
      "radius_ratio": [  
        0.4  
      ],  
      "level": [  
        "myofilaments"  
      ]  
    }  
  ]  
}
```

```

    ]
  },
  {
    "variable": [
      "k_on"
    ],
    "factor": [
      1
    ],
    "radius_ratio": [
      0.4
    ],
    "level": [
      "myofilaments"
    ]
  }
]
},
"mesh_path": [
  "../simulations/baro_baro_b_setpoint_30//sim_inputs/ellipsoidal_correct_fiber.hdf5"
],
"relative_path": [
  true
],
"pericardial": {
  "type": [
    "spring"
  ],

```

```
"k_spring": [  
    200  
]  
},  
"forms_parameters": {  
    "passive_law_parameters": {  
        "bfs": [  
            1.627  
        ],  
        "c": [  
            200  
        ],  
        "passive_law": [  
            "semi_structural"  
        ],  
        "bf": [  
            8.0  
        ],  
        "bt": [  
            3.58  
        ],  
        "phi_g": [  
            1.0  
        ],  
        "c3": [  
            15.0  
        ],  
        "c2": [  

```

```
        250
    ],
    "phi_m": [
        1.0
    ]
}
}
}
```

## APPENDIX 2. FILE S2

```
{
  "protocol":
  {
    "no_of_time_steps": [250000],
    "time_step": [0.001],
    "baroreflex":
    {
      "activations": [
        {
          "t_start_s": [5],
          "t_stop_s": [20]
        }
      ]
    },
    "growth":
    {
      "activations":
      [
        {
          "t_start_s": [20],
          "t_stop_s": [400]
        }
      ]
    },
    "perturbation":
    {
      "perturbations":
```



```

[
  {
    "level": ["circulation"],
    "variable": ["aorta_resistance"],
    "t_start_s": [30],
    "t_stop_s": [40],
    "total_change": [150]
  },
  {
    "level": ["circulation"],
    "variable": ["aorta_resistance"],
    "t_start_s": [130],
    "t_stop_s": [140],
    "total_change": [-150]
  },
  {
    "level": ["circulation"],
    "variable": ["mitral_insufficiency_conductance"],
    "t_start_s": [30],
    "t_stop_s": [40],
    "total_change": [0.0]
  }
]

},

"heart_rate": {

```

```

    "t_active_period": [0.003],
    "t_quiescent_period": [0.92],
    "t_first_activation": [0.1]
  },
  "mesh":
  {
    "relative_path": [true],

"mesh_path":["../demos/base/sim_inputs/new_mesh/ellipsoidal_correct_fiber.hdf5"],
    "function_spaces":
    [
      {
        "name":["stimulusFS"],
        "type":["scalar"],
        "element_type":["DG"],
        "degree": [1]
      },
      {
        "name":["scalar"],
        "type":["scalar"],
        "element_type":["DG"],
        "degree": [1]
      },
      {
        "name":["tensor_space"],
        "type":["tensor"],
        "element_type":["DG"],
        "degree": [1]
      },
    ]
  }

```

```

{
  "name":["growth_scalar_FS"],
  "type":["scalar"],
  "element_type":["DG"],
  "degree": [1]
},
{
  "name":["growth_tensor_FS"],
  "type":["tensor"],
  "element_type":["DG"],
  "degree": [1]
},
{
  "name":["material_coord_system_space"],
  "type":["vector"],
  "element_type":["Quadrature"],
  "degree": [2]
},
{
  "name":["quadrature_space"],
  "type":["scalar"],
  "element_type":["Quadrature"],
  "degree": [2]
}
],
"forms_parameters":
{
  "passive_law_parameters": {

```

```

    "passive_law": ["semi_structural"],
    "c": [200],
    "c2": [250],
    "c3": [15.0],
    "bf": [8.0],
    "bt": [3.58],
    "bfs": [1.627],
    "phi_m": [1.0],
    "phi_g": [1.0]
  }
},
"apex_contractility":
{
  "components":
  [
    {
      "radius_ratio": [0.4],
      "level": ["myofilaments"],
      "variable": ["k_1"],
      "factor": [1]
    },
    {
      "radius_ratio": [0.4],
      "level": ["myofilaments"],
      "variable": ["k_on"],
      "factor": [1]
    }
  ]
}

```

```

    },
    "solver":
    {
      "params":
      {
        "rel_tol": [1e-11],
        "abs_tol": [1e-11],
        "max_iter": [100],
        "debugging_mode": [false]
      }
    }
  },
  "model":
  {
    "circulation":
    {
      "model_scheme": ["LV_with_6_compartments"],
      "blood_volume": [4.5],
      "compartments":
      [
        {
          "name": ["aorta"],
          "resistance": [20],
          "compliance": [4e-4],
          "slack_volume": [0.3]
        },
        {
          "name": ["arteries"],

```

```
"resistance": [20],
"compliance": [8e-4],
"slack_volume": [0.3]
},
{
"name": ["arterioles"],
"resistance": [800],
"compliance": [1e-3],
"slack_volume": [0.1]
},
{
"name": ["capillaries"],
"resistance": [350],
"compliance": [1e-2],
"slack_volume": [0.25]
},
{
"name": ["venules"],
"resistance": [50],
"compliance": [0.03],
"slack_volume": [0.5]
},
{
"name": ["veins"],
"resistance": [50],
"compliance": [0.8e-1],
"slack_volume": [2.0],
"inertance": [0]
```

```

    },
    {
      "name": ["ventricle"],
      "resistance": [5],
      "slack_volume": [0.06],
      "wall_density": [1055],
      "initial_ed_volume": [0.15]
    }
  ]
},
"half_sarcomere":
{
  "initial_hs_length": [900],
  "reference_hs_length": [1100],
  "membranes":
  {
    "Ca_content": [1e-3],
    "k_leak": [6e-4],
    "k_act": [8.2e-2],
    "k_serca": [8],
    "t_open": [0.01],
    "implementation":
    {
      "kinetic_scheme": ["simple_2_compartment"]
    }
  },
  "myofilaments":
  {

```

```
"cb_number_density": [6.9e16],
"prop_fibrosis": [0.0],
"prop_myofilaments": [0.6],
"k_1": [3],
"k_force": [1e-3],
"k_2": [200],
"k_3": [120],
"k_4_0": [80],
"k_4_1": [1.5],
"k_cb": [0.001],
"x_ps": [5],
"k_on": [2e8],
"k_off": [200],
"k_coop": [5],
"int_passive_exp_sigma": [100],
"int_passive_exp_L": [75],
"int_passive_l_slack": [850],
"ext_passive_exp_sigma": [100],
"ext_passive_exp_L": [70],
"ext_passive_l_slack": [950],
"implementation":
{
  "kinetic_scheme": ["3_state_with_SRX"],
  "int_passive_mode": ["exponential"],
  "ext_passive_mode": ["exponential"],
  "max_rate": [2000],
  "temperature": [310],
  "bin_min": [-10],
```



```

    "bin_max": [10],
    "bin_width": [1],
    "filament_compliance_factor": [0.5],
    "thick_filament_length": [815],
    "thin_filament_length": [1120],
    "bare_zone_length": [80],
    "reference_hsl_0": [1100],
    "delta_G_ATP": [70000],
    "thick_wall_approximation": [true]
  }
}
},
"baroreflex":
{
  "b_setpoint": [90],
  "b_slope": [0.02],
  "k_drive": [20],
  "k_recov": [0.1],
  "controls":
  {
    "control":
    [
      {
        "level": ["heart_rate"],
        "variable": ["t_quiescent_period"],
        "k_drive": [0.03],
        "k_recov": [0.0],
        "para_factor": [1.753497],

```

```

    "symp_factor": [0.386]
  },
  {
    "level": ["membranes"],
    "variable": ["k_act"],
    "k_drive": [0.03],
    "k_recov": [0.0],
    "para_factor": [0.333],
    "symp_factor": [3.0]
  },
  {
    "level": ["membranes"],
    "variable": ["k_serca"],
    "k_drive": [0.03],
    "k_recov": [0.0],
    "para_factor": [0.333],
    "symp_factor": [3]
  },
  {
    "level": ["myofilaments"],
    "variable": ["k_1"],
    "k_drive": [0.03],
    "k_recov": [0.0],
    "para_factor": [0.333],
    "symp_factor": [3]
  },
  {
    "level": ["myofilaments"],

```

```

    "variable": ["k_3"],
    "k_drive": [0.03],
    "k_recov": [0.0],
    "para_factor": [0.333],
    "symp_factor": [3]
  },
  {
    "level": ["myofilaments"],
    "variable": ["k_on"],
    "k_drive": [0.03],
    "k_recov": [0.0],
    "para_factor": [3],
    "symp_factor": [0.333]
  },
  {
    "level": ["circulation"],
    "variable": ["arterioles_resistance"],
    "k_drive": [0.03],
    "k_recov": [0.0],
    "para_factor": [0.333],
    "symp_factor": [3]
  },
  {
    "level": ["circulation"],
    "variable": ["veins_compliance"],
    "k_drive": [0.03],
    "k_recov": [0.0],
    "para_factor": [3],

```

```

        "symp_factor": [0.333]
    }
]
}
},
"growth":
{
    "growth_frequency_n": [3],
    "components":
    [
        {
            "type": ["sheet"],
            "signal": ["total_stress"],
            "tau": [8],
            "theta_max": [1.5],
            "theta_min": [0.5],
            "local_theta_max": [1.1],
            "local_theta_min": [0.9]
        },
        {
            "type": ["sheet_normal"],
            "signal": ["total_stress"],
            "tau": [8],
            "theta_max": [1.5],
            "theta_min": [0.5],
            "local_theta_max": [1.1],
            "local_theta_min": [0.9]
        }
    ]
}

```

```

    ]
  }
},
"output_handler":
{
  "output_data_path":
["/mnt/gpfs2_4m/scratch/hsh245/growth_AS_150_rev/data.csv"],
  "mesh_output_path":
["/mnt/gpfs2_4m/scratch/hsh245/growth_AS_150_rev/mesh_output"],
  "mesh_object_to_save":
[
  "displacement",
  "active_stress",
  "hs_length",
  "facetboundaries",
  "k_1",
  "k_3",
  "k_on",
  "k_act",
  "k_serca",
  "local_theta_vis_sheet",
  "global_theta_vis_sheet",
  "local_theta_vis_sheet_normal",
  "global_theta_vis_sheet_normal",
  "stimulus_sheet",
  "deviation_sheet",
  "stimulus_sheet_normal",
  "deviation_sheet_normal",
  "setpoint_sheet",

```

```
        "setpoint_sheet_normal"
    ],
    "growth_mesh_path":
    ["/mnt/gpfs2_4m/scratch/hsh245/growth_AS_150_rev/mesh_output"],
    "dumping_spatial_in_average": [true],
    "frequency_n": [10]

}
}
```

### APPENDIX 3. FILE S3

```
{
  "protocol":
  {
    "no_of_time_steps": [250000],
    "time_step": [0.001],
    "baroreflex":
    {
      "activations": [
        {
          "t_start_s": [5],
          "t_stop_s": [4000]
        }
      ]
    },
    "growth":
    {
      "activations":
      [
        {
          "t_start_s": [20],
          "t_stop_s": [400]
        }
      ]
    },
    "perturbation":
    {
      "perturbations":
```

```

[
  {
    "level": ["circulation"],
    "variable": ["aorta_resistance"],
    "t_start_s": [0.005],
    "t_stop_s": [0.006],
    "total_change": [0]
  },
  {
    "level": ["circulation"],
    "variable": ["mitral_insufficiency_conductance"],
    "t_start_s": [30],
    "t_stop_s": [40],
    "total_change": [0.003]
  },
  {
    "level": ["circulation"],
    "variable": ["mitral_insufficiency_conductance"],
    "t_start_s": [130],
    "t_stop_s": [140],
    "total_change": [-0.003]
  }
]

},
"heart_rate": {

```



```

    "t_active_period": [0.003],
    "t_quiescent_period": [0.92],
    "t_first_activation": [0.1]
  },
  "mesh":
  {
    "relative_path": [true],

"mesh_path":["../demos/base/sim_inputs/new_mesh/ellipsoidal_correct_fiber.hdf5"],
    "function_spaces":
    [
      {
        "name":["stimulusFS"],
        "type":["scalar"],
        "element_type":["DG"],
        "degree": [1]
      },
      {
        "name":["scalar"],
        "type":["scalar"],
        "element_type":["DG"],
        "degree": [1]
      },
      {
        "name":["tensor_space"],
        "type":["tensor"],
        "element_type":["DG"],
        "degree": [1]
      },
    ]
  }

```

```

    {
      "name":["growth_scalar_FS"],
      "type":["scalar"],
      "element_type":["DG"],
      "degree": [1]
    },
    {
      "name":["growth_tensor_FS"],
      "type":["tensor"],
      "element_type":["DG"],
      "degree": [1]
    },
    {
      "name":["material_coord_system_space"],
      "type":["vector"],
      "element_type":["Quadrature"],
      "degree": [2]
    },
    {
      "name":["quadrature_space"],
      "type":["scalar"],
      "element_type":["Quadrature"],
      "degree": [2]
    }
  ],
  "forms_parameters":
  {
    "passive_law_parameters": {

```

```

    "passive_law": ["semi_structural"],
    "c": [200],
    "c2": [250],
    "c3": [15.0],
    "bf": [8.0],
    "bt": [3.58],
    "bfs": [1.627],
    "phi_m": [1.0],
    "phi_g": [1.0]
  }
},
"apex_contractility":
{
  "components":
  [
    {
      "radius_ratio": [0.4],
      "level": ["myofilaments"],
      "variable": ["k_1"],
      "factor": [1]
    },
    {
      "radius_ratio": [0.4],
      "level": ["myofilaments"],
      "variable": ["k_on"],
      "factor": [1]
    }
  ]
}

```

```

    },
    "solver":
    {
      "params":
      {
        "rel_tol": [1e-11],
        "abs_tol": [1e-11],
        "max_iter": [100],
        "debugging_mode": [false]
      }
    }
  },
  "model":
  {
    "circulation":
    {
      "model_scheme": ["LV_with_6_compartments"],
      "blood_volume": [4.5],
      "compartments":
      [
        {
          "name": ["aorta"],
          "resistance": [20],
          "compliance": [4e-4],
          "slack_volume": [0.3]
        },
        {
          "name": ["arteries"],

```

```
"resistance": [20],
"compliance": [8e-4],
"slack_volume": [0.3]
},
{
"name": ["arterioles"],
"resistance": [800],
"compliance": [1e-3],
"slack_volume": [0.1]
},
{
"name": ["capillaries"],
"resistance": [350],
"compliance": [1e-2],
"slack_volume": [0.25]
},
{
"name": ["venules"],
"resistance": [50],
"compliance": [0.03],
"slack_volume": [0.5]
},
{
"name": ["veins"],
"resistance": [50],
"compliance": [0.8e-1],
"slack_volume": [2.0],
"inertance": [0]
```

```

    },
    {
      "name": ["ventricle"],
      "resistance": [5],
      "slack_volume": [0.06],
      "wall_density": [1055],
      "initial_ed_volume": [0.15]
    }
  ]
},
"half_sarcomere":
{
  "initial_hs_length": [900],
  "reference_hs_length": [1100],
  "membranes":
  {
    "Ca_content": [1e-3],
    "k_leak": [6e-4],
    "k_act": [8.2e-2],
    "k_serca": [8],
    "t_open": [0.01],
    "implementation":
    {
      "kinetic_scheme": ["simple_2_compartment"]
    }
  },
  "myofilaments":
  {

```

```
"cb_number_density": [6.9e16],
"prop_fibrosis": [0.0],
"prop_myofilaments": [0.6],
"k_1": [3],
"k_force": [1e-3],
"k_2": [200],
"k_3": [120],
"k_4_0": [80],
"k_4_1": [1.5],
"k_cb": [0.001],
"x_ps": [5],
"k_on": [2e8],
"k_off": [200],
"k_coop": [5],
"int_passive_exp_sigma": [100],
"int_passive_exp_L": [75],
"int_passive_l_slack": [850],
"ext_passive_exp_sigma": [100],
"ext_passive_exp_L": [70],
"ext_passive_l_slack": [950],
"implementation":
{
  "kinetic_scheme": ["3_state_with_SRX"],
  "int_passive_mode": ["exponential"],
  "ext_passive_mode": ["exponential"],
  "max_rate": [2000],
  "temperature": [310],
  "bin_min": [-10],
```

```

    "bin_max": [10],
    "bin_width": [1],
    "filament_compliance_factor": [0.5],
    "thick_filament_length": [815],
    "thin_filament_length": [1120],
    "bare_zone_length": [80],
    "reference_hsl_0": [1100],
    "delta_G_ATP": [70000],
    "thick_wall_approximation": [true]
  }
}
},
"baroreflex":
{
  "b_setpoint": [90],
  "b_slope": [0.02],
  "k_drive": [20],
  "k_recov": [0.1],
  "controls":
  {
    "control":
    [
      {
        "level": ["heart_rate"],
        "variable": ["t_quiescent_period"],
        "k_drive": [0.03],
        "k_recov": [0.1],
        "para_factor": [1.753497],

```



```

    "symp_factor": [0.386]
  },
  {
    "level": ["membranes"],
    "variable": ["k_act"],
    "k_drive": [0.03],
    "k_recov": [0.1],
    "para_factor": [0.333],
    "symp_factor": [3.0]
  },
  {
    "level": ["membranes"],
    "variable": ["k_serca"],
    "k_drive": [0.03],
    "k_recov": [0.1],
    "para_factor": [0.333],
    "symp_factor": [3]
  },
  {
    "level": ["myofilaments"],
    "variable": ["k_1"],
    "k_drive": [0.03],
    "k_recov": [0.1],
    "para_factor": [0.333],
    "symp_factor": [3]
  },
  {
    "level": ["myofilaments"],

```

```

    "variable": ["k_3"],
    "k_drive": [0.03],
    "k_recov": [0.1],
    "para_factor": [0.333],
    "symp_factor": [3]
  },
  {
    "level": ["myofilaments"],
    "variable": ["k_on"],
    "k_drive": [0.03],
    "k_recov": [0.1],
    "para_factor": [3],
    "symp_factor": [0.333]
  },
  {
    "level": ["circulation"],
    "variable": ["arterioles_resistance"],
    "k_drive": [0.03],
    "k_recov": [0.1],
    "para_factor": [0.333],
    "symp_factor": [3]
  },
  {
    "level": ["circulation"],
    "variable": ["veins_compliance"],
    "k_drive": [0.03],
    "k_recov": [0.1],
    "para_factor": [3],

```

```

        "symp_factor": [0.333]
    }
]
}
},
"growth":
{
    "growth_frequency_n": [3],
    "components":
    [
        {
            "type": ["fiber"],
            "signal": ["myofiber_passive_stress"],
            "tau": [10],
            "theta_max": [1.5],
            "theta_min": [0.5],
            "local_theta_max": [1.1],
            "local_theta_min": [0.9]
        }
    ]
}
},
"output_handler":
{
    "output_data_path":
["/mnt/gpfs2_4m/scratch/hsh245/growth_MR_0.003_baro_rev/data.csv"],
    "mesh_output_path":
["/mnt/gpfs2_4m/scratch/hsh245/growth_MR_0.003_baro_rev/mesh_output"],
    "mesh_object_to_save":

```

```

[
  "displacement",
  "active_stress",
  "hs_length",
  "facetboundaries",
  "k_1",
  "k_3",
  "k_on",
  "k_act",
  "k_serca",
  "local_theta_vis_fiber",
  "global_theta_vis_fiber",
  "deviation_fiber",
  "stimulus_fiber",
  "setpoint_fiber"
],
"growth_mesh_path":
["/mnt/gpfs2_4m/scratch/hsh245/growth_MR_0.003_baro_rev/mesh_output"],
"dumping_spatial_in_average": [true],
"frequency_n": [10]
}
}

```

## APPENDIX 4. SUPPLEMENTARY FIGURES

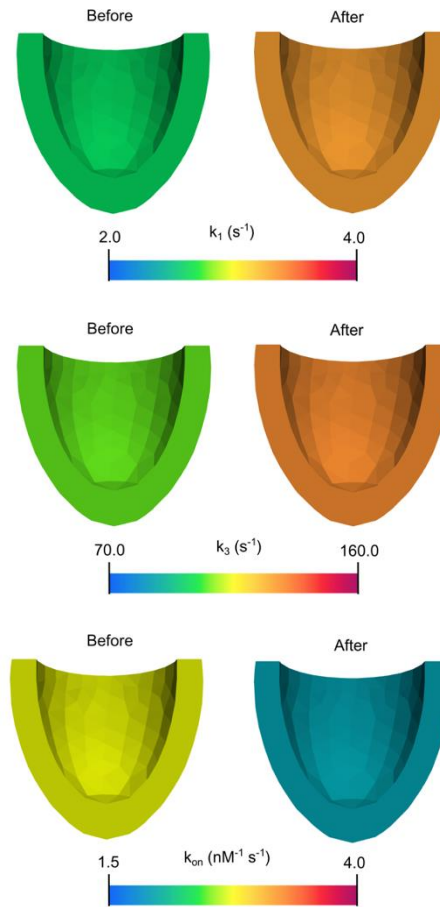


*Figure S 1 Baroreflex regulation of parameters related to thick filament function before and after increasing the setpoint from 90 to 120 mmHg.*

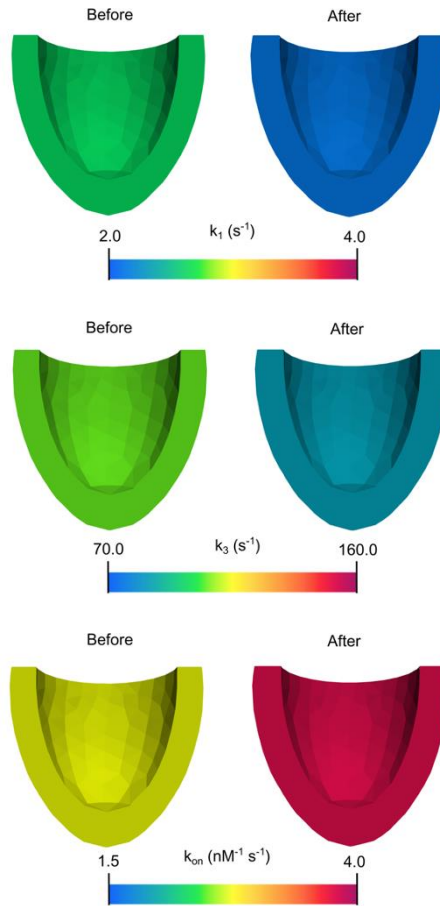


*Figure S 2 Baroreflex regulation of parameters related to thick filament function before and after decreasing the setpoint from 90 to 60 mmHg.*

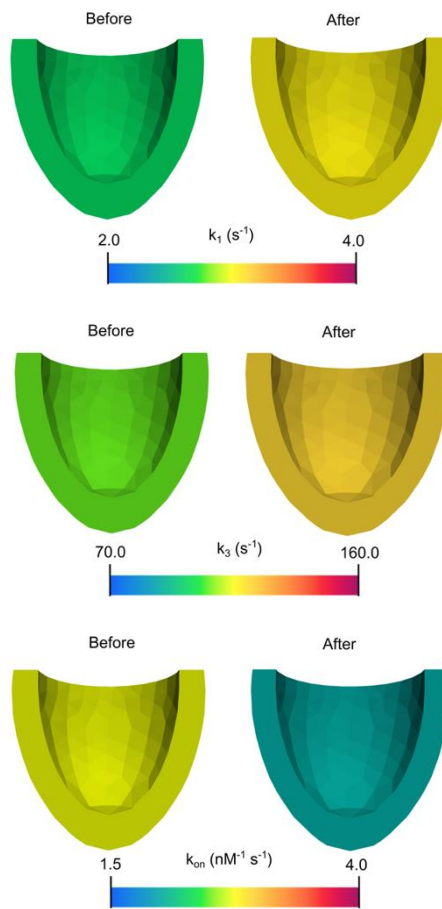


*Figure S 3 Baroreflex regulation of parameters related to thick filament function before and after increasing aortic resistance.*

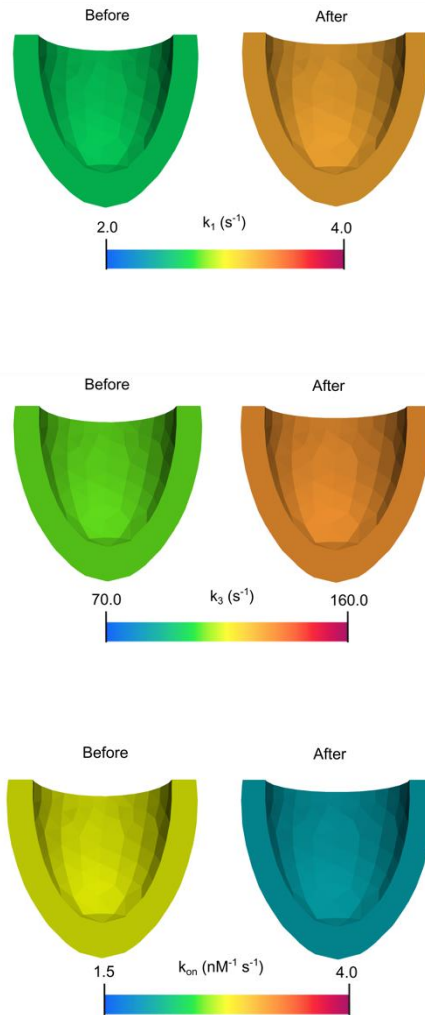


**Figure S 4 Baroreflex regulation of parameters related to thick filament function before and after inducing mitral regurgitation.**



## REFERENCES

1. Sharifi, H., et al., *Multiscale simulations of left ventricular growth and remodeling*. Biophys Rev, 2021. **13**(5): p. 729-746.
2. Nakamura, M. and J. Sadoshima, *Mechanisms of physiological and pathological cardiac hypertrophy*. Nat Rev Cardiol, 2018. **15**(7): p. 387-407.
3. Swynghedauw, B., *Developmental and functional adaptation of contractile proteins in cardiac and skeletal muscles*. Physiol Rev, 1986. **66**(3): p. 710-71.
4. Rajendra Acharya, U., et al., *Heart rate variability: a review*. Med Biol Eng Comput, 2006. **44**(12): p. 1031-51.
5. Wisdom, K.M., S.L. Delp, and E. Kuhl, *Use it or lose it: multiscale skeletal muscle adaptation to mechanical stimuli*. Biomech Model Mechanobiol, 2015. **14**(2): p. 195-215.
6. Hill, J.A. and E.N. Olson, *Cardiac plasticity*. N Engl J Med, 2008. **358**(13): p. 1370-80.
7. Ehler, E. and M. Gautel, *The sarcomere and sarcomerogenesis*. Adv Exp Med Biol, 2008. **642**: p. 1-14.
8. Weber, K.T. and C.G. Brilla, *Pathological hypertrophy and cardiac interstitium. Fibrosis and renin-angiotensin-aldosterone system*. Circulation, 1991. **83**(6): p. 1849-65.
9. Chung, E. and L.A. Leinwand, *Pregnancy as a cardiac stress model*. Cardiovasc Res, 2014. **101**(4): p. 561-70.
10. Milliken, M.C., et al., *Left ventricular mass as determined by magnetic resonance imaging in male endurance athletes*. Am J Cardiol, 1988. **62**(4): p. 301-5.
11. Fagard, R., *Athlete's heart*. Heart, 2003. **89**(12): p. 1455-61.
12. Maron, B.J. and A. Pelliccia, *The heart of trained athletes: cardiac remodeling and the risks of sports, including sudden death*. Circulation, 2006. **114**(15): p. 1633-44.
13. Li, J., et al., *New frontiers in heart hypertrophy during pregnancy*. Am J Cardiovasc Dis, 2012. **2**(3): p. 192-207.
14. Savu, O., et al., *Morphological and functional adaptation of the maternal heart during pregnancy*. Circ Cardiovasc Imaging, 2012. **5**(3): p. 289-97.
15. Umar, S., et al., *Cardiac structural and hemodynamic changes associated with physiological heart hypertrophy of pregnancy are reversed postpartum*. J Appl Physiol (1985), 2012. **113**(8): p. 1253-9.
16. Frey, N. and E.N. Olson, *Cardiac hypertrophy: the good, the bad, and the ugly*. Annu Rev Physiol, 2003. **65**: p. 45-79.
17. Shimizu, I. and T. Minamino, *Physiological and pathological cardiac hypertrophy*. J Mol Cell Cardiol, 2016. **97**: p. 245-62.
18. Pitoulis, F.G. and C.M. Terracciano, *Heart Plasticity in Response to Pressure- and Volume-Overload: A Review of Findings in Compensated and Decompensated Phenotypes*. Front Physiol, 2020. **11**: p. 92.
19. Lalande, S. and B.D. Johnson, *Diastolic dysfunction: a link between hypertension and heart failure*. Drugs Today (Barc), 2008. **44**(7): p. 503-13.
20. Drazner, M.H., *The progression of hypertensive heart disease*. Circulation, 2011. **123**(3): p. 327-34.

21. Berta, E., et al., *Hypertension in Thyroid Disorders*. Front Endocrinol (Lausanne), 2019. **10**: p. 482.
22. Carabello, B.A. and W.J. Paulus, *Aortic stenosis*. Lancet, 2009. **373**(9667): p. 956-66.
23. Siu, S.C. and C.K. Silversides, *Bicuspid aortic valve disease*. J Am Coll Cardiol, 2010. **55**(25): p. 2789-800.
24. Lindman, B.R., et al., *Calcific aortic stenosis*. Nat Rev Dis Primers, 2016. **2**: p. 16006.
25. Enriquez-Sarano, M., C.W. Akins, and A. Vahanian, *Mitral regurgitation*. Lancet, 2009. **373**(9672): p. 1382-94.
26. Akinseye, O.A., A. Pathak, and U.N. Ibebuogu, *Aortic Valve Regurgitation: A Comprehensive Review*. Curr Probl Cardiol, 2018. **43**(8): p. 315-334.
27. Carabello, B.A., et al., *Left ventricular hypertrophy due to volume overload versus pressure overload*. Am J Physiol, 1992. **263**(4 Pt 2): p. H1137-44.
28. Grossman, W., D. Jones, and L.P. McLaurin, *Wall stress and patterns of hypertrophy in the human left ventricle*. J Clin Invest, 1975. **56**(1): p. 56-64.
29. Maron, B.J. and M.S. Maron, *Hypertrophic cardiomyopathy*. Lancet, 2013. **381**(9862): p. 242-55.
30. Maron, B.J., et al., *Clinical Spectrum and Management of Heart Failure in Hypertrophic Cardiomyopathy*. JACC Heart Fail, 2018. **6**(5): p. 353-363.
31. Maron, B.J., *Hypertrophic cardiomyopathy: a systematic review*. JAMA, 2002. **287**(10): p. 1308-20.
32. Vera, C.D., et al., *Myosin motor domains carrying mutations implicated in early or late onset hypertrophic cardiomyopathy have similar properties*. J Biol Chem, 2019. **294**(46): p. 17451-17462.
33. Maron, B.J., M.S. Maron, and C. Semsarian, *Genetics of hypertrophic cardiomyopathy after 20 years: clinical perspectives*. J Am Coll Cardiol, 2012. **60**(8): p. 705-15.
34. Spudich, J.A., *Three perspectives on the molecular basis of hypercontractility caused by hypertrophic cardiomyopathy mutations*. Pflugers Arch, 2019. **471**(5): p. 701-717.
35. Watkins, H., H. Ashrafian, and C. Redwood, *Inherited cardiomyopathies*. N Engl J Med, 2011. **364**(17): p. 1643-56.
36. Frey, N., M. Luedde, and H.A. Katus, *Mechanisms of disease: hypertrophic cardiomyopathy*. Nat Rev Cardiol, 2011. **9**(2): p. 91-100.
37. Maron, B.J., *Clinical Course and Management of Hypertrophic Cardiomyopathy*. N Engl J Med, 2018. **379**(20): p. 1977.
38. Rodriguez, E.K., A. Hoger, and A.D. McCulloch, *Stress-dependent finite growth in soft elastic tissues*. J Biomech, 1994. **27**(4): p. 455-67.
39. Mojumder, J., et al., *Mechanical stimuli for left ventricular growth during pressure overload*. Exp Mech, 2021. **61**(1): p. 131-146.
40. Rondanina, E. and P.H.M. Bovendeerd, *Evaluation of stimulus-effect relations in left ventricular growth using a simple multiscale model*. Biomech Model Mechanobiol, 2020. **19**(1): p. 263-273.
41. Lee, L.C., et al., *A computational model that predicts reverse growth in response to mechanical unloading*. Biomech Model Mechanobiol, 2015. **14**(2): p. 217-29.

42. Peirlinck, M., et al., *Precision medicine in human heart modeling : Perspectives, challenges, and opportunities*. Biomech Model Mechanobiol, 2021. **20**(3): p. 803-831.
43. Alastrue, V., et al., *Assessing the use of the "opening angle method" to enforce residual stresses in patient-specific arteries*. Ann Biomed Eng, 2007. **35**(10): p. 1821-37.
44. Skalak, R., et al., *Compatibility and the genesis of residual stress by volumetric growth*. J Math Biol, 1996. **34**(8): p. 889-914.
45. Genet, M., et al., *Heterogeneous growth-induced prestrain in the heart*. J Biomech, 2015. **48**(10): p. 2080-9.
46. Rachev, A., N. Stergiopoulos, and J.J. Meister, *A model for geometric and mechanical adaptation of arteries to sustained hypertension*. J Biomech Eng, 1998. **120**(1): p. 9-17.
47. Taber, L.A., *A model for aortic growth based on fluid shear and fiber stresses*. J Biomech Eng, 1998. **120**(3): p. 348-54.
48. Kuhl, E., et al., *Computational modeling of arterial wall growth. Attempts towards patient-specific simulations based on computer tomography*. Biomech Model Mechanobiol, 2007. **6**(5): p. 321-31.
49. Rodriguez, J., J.M. Goicolea, and F. Gabaldon, *A volumetric model for growth of arterial walls with arbitrary geometry and loads*. J Biomech, 2007. **40**(5): p. 961-71.
50. Saez, P., et al., *Computational modeling of hypertensive growth in the human carotid artery*. Comput Mech, 2014. **53**(6): p. 1183-1196.
51. Lin, I.E. and L.A. Taber, *A model for stress-induced growth in the developing heart*. J Biomech Eng, 1995. **117**(3): p. 343-9.
52. Taber, L.A., *Biomechanical growth laws for muscle tissue*. J Theor Biol, 1998. **193**(2): p. 201-13.
53. Taber, L.A. and S. Chabert, *Theoretical and experimental study of growth and remodeling in the developing heart*. Biomech Model Mechanobiol, 2002. **1**(1): p. 29-43.
54. Ramasubramanian, A., et al., *On modeling morphogenesis of the looping heart following mechanical perturbations*. J Biomech Eng, 2008. **130**(6): p. 061018.
55. Ramasubramanian, A. and L.A. Taber, *Computational modeling of morphogenesis regulated by mechanical feedback*. Biomech Model Mechanobiol, 2008. **7**(2): p. 77-91.
56. Kroon, W., et al., *Computational modeling of volumetric soft tissue growth: application to the cardiac left ventricle*. Biomech Model Mechanobiol, 2009. **8**(4): p. 301-9.
57. Omens, J.H., *Stress and strain as regulators of myocardial growth*. Prog Biophys Mol Biol, 1998. **69**(2-3): p. 559-72.
58. Rausch, M.K., et al., *Computational modeling of growth: systemic and pulmonary hypertension in the heart*. Biomech Model Mechanobiol, 2011. **10**(6): p. 799-811.
59. Klepach, D., et al., *Growth and remodeling of the left ventricle: A case study of myocardial infarction and surgical ventricular restoration*. Mech Res Commun, 2012. **42**: p. 134-141.

60. Del Bianco, F., et al., *Electromechanical effects of concentric hypertrophy on the left ventricle: A simulation study*. Comput Biol Med, 2018. **99**: p. 236-256.
61. Emery, J.L. and J.H. Omens, *Mechanical regulation of myocardial growth during volume-overload hypertrophy in the rat*. Am J Physiol, 1997. **273**(3 Pt 2): p. H1198-204.
62. Guterl, K.A., et al., *Isometric contraction induces rapid myocyte remodeling in cultured rat right ventricular papillary muscles*. Am J Physiol Heart Circ Physiol, 2007. **293**(6): p. H3707-12.
63. Kerckhoffs, R.C., J. Omens, and A.D. McCulloch, *A single strain-based growth law predicts concentric and eccentric cardiac growth during pressure and volume overload*. Mech Res Commun, 2012. **42**: p. 40-50.
64. Witzenburg, C.M. and J.W. Holmes, *Predicting the Time Course of Ventricular Dilatation and Thickening Using a Rapid Compartmental Model*. J Cardiovasc Transl Res, 2018. **11**(2): p. 109-122.
65. Lee, L.C., et al., *An integrated electromechanical-growth heart model for simulating cardiac therapies*. Biomech Model Mechanobiol, 2016. **15**(4): p. 791-803.
66. Goktepe, S., et al., *A multiscale model for eccentric and concentric cardiac growth through sarcomerogenesis*. J Theor Biol, 2010. **265**(3): p. 433-42.
67. Genet, M., et al., *Modeling Pathologies of Diastolic and Systolic Heart Failure*. Ann Biomed Eng, 2016. **44**(1): p. 112-27.
68. Arumugam, J., et al., *Model of Anisotropic Reverse Cardiac Growth in Mechanical Dyssynchrony*. Sci Rep, 2019. **9**(1): p. 12670.
69. Peirlinck, M., et al., *Using machine learning to characterize heart failure across the scales*. Biomech Model Mechanobiol, 2019. **18**(6): p. 1987-2001.
70. Yoshida, K., et al., *Predictions of hypertrophy and its regression in response to pressure overload*. Biomech Model Mechanobiol, 2020. **19**(3): p. 1079-1089.
71. Berberoğlu, E.S., H.O.; Göktepe, S., *Computational modeling of coupled cardiac electromechanics incorporating cardiac dysfunctions*. European Journal of Mechanics - A/Solids, 2014. **48**: p. 60-73.
72. Witzenburg, C.M. and J.W. Holmes, *A Comparison of Phenomenologic Growth Laws for Myocardial Hypertrophy*. J Elast, 2017. **129**(1-2): p. 257-281.
73. Rondanina, E. and P.H.M. Bovendeerd, *Stimulus-effect relations for left ventricular growth obtained with a simple multi-scale model: the influence of hemodynamic feedback*. Biomech Model Mechanobiol, 2020. **19**(6): p. 2111-2126.
74. Estrada, A.C., et al., *A multiscale model of cardiac concentric hypertrophy incorporating both mechanical and hormonal drivers of growth*. Biomech Model Mechanobiol, 2021. **20**(1): p. 293-307.
75. Yoshida, K.S., J. J.; Holmes, J. W, *Multiscale model of heart growth during pregnancy: Integrating mechanical and hormonal signaling*. bioRxiv, 2020.
76. Humphrey, J.D.a.R., K. R., *A Constrained Mixture Model for Growth and Remodeling of Soft Tissues*. Mathematical Models and Methods in Applied Sciences, 2002. **12**: p. 407-430.
77. Cyron, C.J., R.C. Aydin, and J.D. Humphrey, *A homogenized constrained mixture (and mechanical analog) model for growth and remodeling of soft tissue*. Biomech Model Mechanobiol, 2016. **15**(6): p. 1389-1403.

78. Valentin, A., J.D. Humphrey, and G.A. Holzapfel, *A finite element-based constrained mixture implementation for arterial growth, remodeling, and adaptation: theory and numerical verification*. Int J Numer Method Biomed Eng, 2013. **29**(8): p. 822-49.
79. Ateshian, G.A. and J.D. Humphrey, *Continuum mixture models of biological growth and remodeling: past successes and future opportunities*. Annu Rev Biomed Eng, 2012. **14**: p. 97-111.
80. Valentin, A. and G.A. Holzapfel, *Constrained Mixture Models as Tools for Testing Competing Hypotheses in Arterial Biomechanics: A Brief Survey*. Mech Res Commun, 2012. **42**: p. 126-133.
81. J. D. Humphrey, *Constrained Mixture Models of Soft Tissue Growth and Remodeling – Twenty Years After*. Journal of Elasticity, 2021.
82. Baek, S., K.R. Rajagopal, and J.D. Humphrey, *A theoretical model of enlarging intracranial fusiform aneurysms*. J Biomech Eng, 2006. **128**(1): p. 142-9.
83. Latorre, M. and J.D. Humphrey, *Fast, Rate-Independent, Finite Element Implementation of a 3D Constrained Mixture Model of Soft Tissue Growth and Remodeling*. Comput Methods Appl Mech Eng, 2020. **368**.
84. Mousavi, S.J. and S. Avril, *Patient-specific stress analyses in the ascending thoracic aorta using a finite-element implementation of the constrained mixture theory*. Biomech Model Mechanobiol, 2017. **16**(5): p. 1765-1777.
85. Yoshida, K. and J.W. Holmes, *Computational models of cardiac hypertrophy*. Prog Biophys Mol Biol, 2021. **159**: p. 75-85.
86. Arts, T., et al., *Adaptation to mechanical load determines shape and properties of heart and circulation: the CircAdapt model*. Am J Physiol Heart Circ Physiol, 2005. **288**(4): p. H1943-54.
87. Guccione, J.M. and A.D. McCulloch, *Mechanics of active contraction in cardiac muscle: Part I--Constitutive relations for fiber stress that describe deactivation*. J Biomech Eng, 1993. **115**(1): p. 72-81.
88. Guccione, J.M., L.K. Waldman, and A.D. McCulloch, *Mechanics of active contraction in cardiac muscle: Part II--Cylindrical models of the systolic left ventricle*. J Biomech Eng, 1993. **115**(1): p. 82-90.
89. Beyar, R. and S. Sideman, *Model for left ventricular contraction combining the force length velocity relationship with the time varying elastance theory*. Biophys J, 1984. **45**(6): p. 1167-77.
90. Santamore, W.P. and D. Burkhoff, *Hemodynamic consequences of ventricular interaction as assessed by model analysis*. Am J Physiol, 1991. **260**(1 Pt 2): p. H146-57.
91. Bovendeerd, P.H., et al., *Dependence of intramyocardial pressure and coronary flow on ventricular loading and contractility: a model study*. Ann Biomed Eng, 2006. **34**(12): p. 1833-45.
92. Cazorla, O., et al., *Differential expression of cardiac titin isoforms and modulation of cellular stiffness*. Circ Res, 2000. **86**(1): p. 59-67.
93. Janicki, J.S. and G.L. Brower, *The role of myocardial fibrillar collagen in ventricular remodeling and function*. J Card Fail, 2002. **8**(6 Suppl): p. S319-25.
94. Bers, D.M., *Cardiac excitation-contraction coupling*. Nature, 2002. **415**(6868): p. 198-205.

95. Solis, C. and R.J. Solaro, *Novel insights into sarcomere regulatory systems control of cardiac thin filament activation*. J Gen Physiol, 2021. **153**(7).
96. Huxley, A.F., *Muscular contraction*. J Physiol, 1974. **243**(1): p. 1-43.
97. Campbell, K.S., *Dynamic coupling of regulated binding sites and cycling myosin heads in striated muscle*. J Gen Physiol, 2014. **143**(3): p. 387-99.
98. Campbell, K.S., P.M.L. Janssen, and S.G. Campbell, *Force-Dependent Recruitment from the Myosin Off State Contributes to Length-Dependent Activation*. Biophys J, 2018. **115**(3): p. 543-553.
99. Rice, J.J., et al., *Approximate model of cooperative activation and crossbridge cycling in cardiac muscle using ordinary differential equations*. Biophys J, 2008. **95**(5): p. 2368-90.
100. Zhang, X., et al., *Evaluation of a Novel Finite Element Model of Active Contraction in the Heart*. Front Physiol, 2018. **9**: p. 425.
101. Mann, C.K., et al., *Force-dependent recruitment from myosin OFF-state increases end-systolic pressure-volume relationship in left ventricle*. Biomech Model Mechanobiol, 2020. **19**(6): p. 2683-2692.
102. Everett, R.J., et al., *Timing of intervention in aortic stenosis: a review of current and future strategies*. Heart, 2018. **104**(24): p. 2067-2076.
103. Gotzmann, M., et al., *Hemodynamics of paradoxical severe aortic stenosis: insight from a pressure-volume loop analysis*. Clin Res Cardiol, 2019. **108**(8): p. 931-939.
104. Lloyd, J.W., et al., *Hemodynamic Response to Nitroprusside in Patients With Low-Gradient Severe Aortic Stenosis and Preserved Ejection Fraction*. J Am Coll Cardiol, 2017. **70**(11): p. 1339-1348.
105. Acker, M.A., et al., *Mitral-valve repair versus replacement for severe ischemic mitral regurgitation*. N Engl J Med, 2014. **370**(1): p. 23-32.
106. Treibel, T.A., et al., *Reverse Myocardial Remodeling Following Valve Replacement in Patients With Aortic Stenosis*. J Am Coll Cardiol, 2018. **71**(8): p. 860-871.
107. Birks, E.J., et al., *Prospective Multicenter Study of Myocardial Recovery Using Left Ventricular Assist Devices (RESTAGE-HF [Remission from Stage D Heart Failure]): Medium-Term and Primary End Point Results*. Circulation, 2020. **142**(21): p. 2016-2028.
108. Stellbrink, C., et al., *Impact of cardiac resynchronization therapy using hemodynamically optimized pacing on left ventricular remodeling in patients with congestive heart failure and ventricular conduction disturbances*. J Am Coll Cardiol, 2001. **38**(7): p. 1957-65.
109. Lee, L.C., et al., *Algisyl-LVR with coronary artery bypass grafting reduces left ventricular wall stress and improves function in the failing human heart*. Int J Cardiol, 2013. **168**(3): p. 2022-8.
110. Wang, H., et al., *Effects of hydrogel injection on borderzone contractility post-myocardial infarction*. Biomech Model Mechanobiol, 2018. **17**(5): p. 1533-1542.
111. Wang, H., et al., *Computational sensitivity investigation of hydrogel injection characteristics for myocardial support*. J Biomech, 2017. **64**: p. 231-235.
112. Dabiri, Y., et al., *Application of feed forward and recurrent neural networks in simulation of left ventricular mechanics*. Sci Rep, 2020. **10**(1): p. 22298.

113. Mirams, G.R., et al., *Uncertainty and variability in computational and mathematical models of cardiac physiology*. J Physiol, 2016. **594**(23): p. 6833-6847.
114. Watson, S.R., J.D. Dormer, and B. Fei, *Imaging technologies for cardiac fiber and heart failure: a review*. Heart Fail Rev, 2018. **23**(2): p. 273-289.
115. Lee, L.C., G.S. Kassab, and J.M. Guccione, *Mathematical modeling of cardiac growth and remodeling*. Wiley Interdiscip Rev Syst Biol Med, 2016. **8**(3): p. 211-26.
116. Oberkampf, W.L. and M.F. Baroneb, *Measures of agreement between computation and experiment: Validation metrics*. Computational Physics, 2006. **217**(1): p. 5-36.
117. Ryall, K.A., et al., *Network reconstruction and systems analysis of cardiac myocyte hypertrophy signaling*. J Biol Chem, 2012. **287**(50): p. 42259-68.
118. Frank, D.U., M.D. Sutcliffe, and J.J. Saucerman, *Network-based predictions of in vivo cardiac hypertrophy*. J Mol Cell Cardiol, 2018. **121**: p. 180-189.
119. Toepfer, C.N., et al., *Hypertrophic cardiomyopathy mutations in MYBPC3 dysregulate myosin*. Sci Transl Med, 2019. **11**(476).
120. Robinson, P., et al., *Dilated and hypertrophic cardiomyopathy mutations in troponin and alpha-tropomyosin have opposing effects on the calcium affinity of cardiac thin filaments*. Circ Res, 2007. **101**(12): p. 1266-73.
121. Campbell, K.S., B.S. Chrisman, and S.G. Campbell, *Multiscale Modeling of Cardiovascular Function Predicts That the End-Systolic Pressure Volume Relationship Can Be Targeted via Multiple Therapeutic Strategies*. Front Physiol, 2020. **11**: p. 1043.
122. Ariga, R., et al., *Identification of Myocardial Disarray in Patients With Hypertrophic Cardiomyopathy and Ventricular Arrhythmias*. J Am Coll Cardiol, 2019. **73**(20): p. 2493-2502.
123. Avazmohammadi, R., et al., *Interactions between structural remodeling and volumetric growth in right ventricle in response to pulmonary arterial hypertension*. J Biomech Eng, 2019.
124. Alber, M., et al., *Integrating machine learning and multiscale modeling-perspectives, challenges, and opportunities in the biological, biomedical, and behavioral sciences*. NPJ Digit Med, 2019. **2**: p. 115.
125. Raissi, M.P., P; Karniadakis, G.E., *Physics-informed neural networks: A deep learning framework for solving forward and inverse problems involving nonlinear partial differential equations*. Journal of Computational Physics, 2019. **378**: p. 686-707.
126. Rudy, S.H.B., S. L.; Proctor, J. L.; Kutz, J. N., *Data-driven discovery of partial differential equations*. SCIENCE ADVANCES, 2017. **3**.
127. Buoso, S., T. Joyce, and S. Kozerke, *Personalising left-ventricular biophysical models of the heart using parametric physics-informed neural networks*. Med Image Anal, 2021. **71**: p. 102066.
128. Costabal, F.S.Y., Y.; Perdikaris, P.; Hurtado, D. E.; and Kuhl, E., *Physics-Informed Neural Networks for Cardiac Activation Mapping*. Front Physiol, 2020. **8**.
129. Shade, J.K., et al., *Predicting risk of sudden cardiac death in patients with cardiac sarcoidosis using multimodality imaging and personalized heart modeling in a multivariable classifier*. Sci Adv, 2021. **7**(31).

130. Peng, G.C.Y., et al., *Multiscale modeling meets machine learning: What can we learn?* Arch Comput Methods Eng, 2021. **28**(3): p. 1017-1037.
131. Lee, T., I. Bilonis, and A.B. Tepole, *Propagation of uncertainty in the mechanical and biological response of growing tissues using multi-fidelity Gaussian process regression.* Comput Methods Appl Mech Eng, 2020. **359**.
132. Sack, K.L., et al., *Construction and Validation of Subject-Specific Biventricular Finite-Element Models of Healthy and Failing Swine Hearts From High-Resolution DT-MRI.* Front Physiol, 2018. **9**: p. 539.
133. Washio, T., et al., *Ventricular fiber optimization utilizing the branching structure.* Int J Numer Method Biomed Eng, 2016. **32**(7).
134. Lanfranchi, P.A. and V.K. Somers, *Arterial baroreflex function and cardiovascular variability: interactions and implications.* Am J Physiol Regul Integr Comp Physiol, 2002. **283**(4): p. R815-26.
135. Ursino, M., *Interaction between carotid baroregulation and the pulsating heart: a mathematical model.* Am J Physiol, 1998. **275**(5): p. H1733-47.
136. Jezek, F., et al., *Systems analysis of the mechanisms governing the cardiovascular response to changes in posture and in peripheral demand during exercise.* J Mol Cell Cardiol, 2022. **163**: p. 33-55.
137. Beard, D.A., et al., *A computational analysis of the long-term regulation of arterial pressure.* F1000Res, 2013. **2**: p. 208.
138. Sharifi, H., et al., *A multiscale model of the cardiovascular system that regulates arterial pressure via closed loop baroreflex control of chronotropism, cell-level contractility, and vascular tone.* Biomech Model Mechanobiol, 2022. **21**(6): p. 1903-1917.
139. Marian, A.J. and E. Braunwald, *Hypertrophic Cardiomyopathy: Genetics, Pathogenesis, Clinical Manifestations, Diagnosis, and Therapy.* Circ Res, 2017. **121**(7): p. 749-770.
140. Reed, G.W., J.E. Rossi, and C.P. Cannon, *Acute myocardial infarction.* Lancet, 2017. **389**(10065): p. 197-210.
141. Rodell, C.B., et al., *Injectable Shear-Thinning Hydrogels for Minimally Invasive Delivery to Infarcted Myocardium to Limit Left Ventricular Remodeling.* Circ Cardiovasc Interv, 2016. **9**(10).
142. Bayer, J.D., et al., *A novel rule-based algorithm for assigning myocardial fiber orientation to computational heart models.* Ann Biomed Eng, 2012. **40**(10): p. 2243-54.
143. M. S. Alnaes, J.B., J. Hake, A. Johansson, B. Kehlet, A. Logg, C. Richardson, J. Ring, M. E. Rognes and G. N. Wells, *The FEniCS Project Version 1.5.* Archive of Numerical Software 3, 2015.
144. Guccione, J.M., A.D. McCulloch, and L.K. Waldman, *Passive material properties of intact ventricular myocardium determined from a cylindrical model.* J Biomech Eng, 1991. **113**(1): p. 42-55.
145. Xi, C., G.S. Kassab, and L.C. Lee, *Microstructure-based finite element model of left ventricle passive inflation.* Acta Biomater, 2019. **90**: p. 241-253.
146. Schmid, M. and C.N. Toepfer, *Cardiac myosin super relaxation (SRX): a perspective on fundamental biology, human disease and therapeutics.* Biol Open, 2021. **10**(2).



147. Solaro, R.J., M. Henze, and T. Kobayashi, *Integration of troponin I phosphorylation with cardiac regulatory networks*. *Circ Res*, 2013. **112**(2): p. 355-66.
148. Kampourakis, T., Y.B. Sun, and M. Irving, *Myosin light chain phosphorylation enhances contraction of heart muscle via structural changes in both thick and thin filaments*. *Proc Natl Acad Sci U S A*, 2016. **113**(21): p. E3039-47.
149. Otto, C.M., et al., *2020 ACC/AHA Guideline for the Management of Patients With Valvular Heart Disease: A Report of the American College of Cardiology/American Heart Association Joint Committee on Clinical Practice Guidelines*. *Circulation*, 2021. **143**(5): p. e72-e227.
150. Ioannou, C.V., et al., *Hemodynamics induced after acute reduction of proximal thoracic aorta compliance*. *Eur J Vasc Endovasc Surg*, 2003. **26**(2): p. 195-204.
151. Pagoulatou, S., et al., *Acute and Long-Term Effects of Aortic Compliance Decrease on Central Hemodynamics: A Modeling Analysis*. *Front Physiol*, 2021. **12**: p. 701154.
152. Wegria, R., et al., *Effect of acute mitral insufficiency of various degrees on mean arterial blood pressure, coronary blood flow cardiac output and oxygen consumption*. *Circ Res*, 1958. **6**(3): p. 301-6.
153. Stouffer, R.V.K.M.G.C.G.A., *Mitral Regurgitation*, in *Cardiovascular Hemodynamics for the Clinician, Second Edition*. 2016. p. 154-162.
154. Theroux, P., et al., *Regional Myocardial function in the conscious dog during acute coronary occlusion and responses to morphine, propranolol, nitroglycerin, and lidocaine*. *Circulation*, 1976. **53**(2): p. 302-14.
155. Matthews, D.C.C.H.G., *Cardiac Pressure–Volume Loops*, in *Basic Physiology for Anaesthetists*. 2019, Cambridge University Press. p. 136-140.
156. Gao, H., et al., *Estimating prognosis in patients with acute myocardial infarction using personalized computational heart models*. *Sci Rep*, 2017. **7**(1): p. 13527.
157. Leung, S.W., et al., *Regional end-systolic circumferential strain demonstrates compensatory segmental contractile function in patients with ST-segment elevation myocardial infarction*. *J Biomech*, 2021. **129**: p. 110794.
158. Mendiola, E.A., et al., *Contractile Adaptation of the Left Ventricle Post-myocardial Infarction: Predictions by Rodent-Specific Computational Modeling*. *Ann Biomed Eng*, 2022.
159. Witzenburg, C.M. and J.W. Holmes, *The Impact of Hemodynamic Reflex Compensation Following Myocardial Infarction on Subsequent Ventricular Remodeling*. *J Biomech Eng*, 2019. **141**(9): p. 0910101-09101010.
160. La Rovere, M.T., et al., *Baroreflex sensitivity, clinical correlates, and cardiovascular mortality among patients with a first myocardial infarction. A prospective study*. *Circulation*, 1988. **78**(4): p. 816-24.
161. Farrell, T.G., et al., *Prognostic value of baroreflex sensitivity testing after acute myocardial infarction*. *Br Heart J*, 1992. **67**(2): p. 129-37.
162. La Rovere, M.T., et al., *Baroreflex sensitivity and heart-rate variability in prediction of total cardiac mortality after myocardial infarction. ATRAMI (Autonomic Tone and Reflexes After Myocardial Infarction) Investigators*. *Lancet*, 1998. **351**(9101): p. 478-84.

163. Wu, E., et al., *Infarct size by contrast enhanced cardiac magnetic resonance is a stronger predictor of outcomes than left ventricular ejection fraction or end-systolic volume index: prospective cohort study*. *Heart*, 2008. **94**(6): p. 730-6.
164. Caggiano, L.R., J.W. Holmes, and C.M. Witzenburg, *Individual variability in animal-specific hemodynamic compensation following myocardial infarction*. *J Mol Cell Cardiol*, 2022. **163**: p. 156-166.
165. Wenk, J.F., et al., *Regional left ventricular myocardial contractility and stress in a finite element model of posterobasal myocardial infarction*. *J Biomech Eng*, 2011. **133**(4): p. 044501.
166. Lee, L.C., et al., *A novel method for quantifying in-vivo regional left ventricular myocardial contractility in the border zone of a myocardial infarction*. *J Biomech Eng*, 2011. **133**(9): p. 094506.
167. Arts, T., et al., *Control of whole heart geometry by intramyocardial mechano-feedback: a model study*. *PLoS Comput Biol*, 2012. **8**(2): p. e1002369.
168. Freiburg, A., et al., *Series of exon-skipping events in the elastic spring region of titin as the structural basis for myofibrillar elastic diversity*. *Circ Res*, 2000. **86**(11): p. 1114-21.
169. Davis, J., et al., *A Tension-Based Model Distinguishes Hypertrophic versus Dilated Cardiomyopathy*. *Cell*, 2016. **165**(5): p. 1147-1159.
170. Petersen, S.E., et al., *Reference ranges for cardiac structure and function using cardiovascular magnetic resonance (CMR) in Caucasians from the UK Biobank population cohort*. *J Cardiovasc Magn Reson*, 2017. **19**(1): p. 18.
171. Maceira, A.M., et al., *Normalized left ventricular systolic and diastolic function by steady state free precession cardiovascular magnetic resonance*. *J Cardiovasc Magn Reson*, 2006. **8**(3): p. 417-26.
172. Chin, C.W., et al., *Echocardiography underestimates stroke volume and aortic valve area: implications for patients with small-area low-gradient aortic stenosis*. *Can J Cardiol*, 2014. **30**(9): p. 1064-72.
173. Chin, C.W.L., et al., *Myocardial Fibrosis and Cardiac Decompensation in Aortic Stenosis*. *JACC Cardiovasc Imaging*, 2017. **10**(11): p. 1320-1333.
174. Luszczak, J., et al., *Assessment of left ventricle function in patients with symptomatic and asymptomatic aortic stenosis by 2-dimensional speckle-tracking imaging*. *Med Sci Monit*, 2012. **18**(12): p. MT91-6.
175. Everett, R.J., et al., *Extracellular Myocardial Volume in Patients With Aortic Stenosis*. *J Am Coll Cardiol*, 2020. **75**(3): p. 304-316.
176. Spath, N.B., et al., *Global Longitudinal Strain Analysis Using Cardiac MRI in Aortic Stenosis: Comparison with Left Ventricular Remodeling, Myocardial Fibrosis, and 2-year Clinical Outcomes*. *Radiol Cardiothorac Imaging*, 2019. **1**(4): p. e190027.
177. Lyon, R.C., et al., *Mechanotransduction in cardiac hypertrophy and failure*. *Circ Res*, 2015. **116**(8): p. 1462-1476.
178. Knoll, R., et al., *The cardiac mechanical stretch sensor machinery involves a Z disc complex that is defective in a subset of human dilated cardiomyopathy*. *Cell*, 2002. **111**(7): p. 943-55.

179. Edwards, N.C., et al., *Quantification of left ventricular interstitial fibrosis in asymptomatic chronic primary degenerative mitral regurgitation*. *Circ Cardiovasc Imaging*, 2014. **7**(6): p. 946-53.
180. Schiros, C.G., et al., *Magnetic resonance imaging with 3-dimensional analysis of left ventricular remodeling in isolated mitral regurgitation: implications beyond dimensions*. *Circulation*, 2012. **125**(19): p. 2334-42.
181. Seldrum, S., et al., *Assessment of Left Ventricular Reverse Remodeling by Cardiac MRI in Patients Undergoing Repair Surgery for Severe Aortic or Mitral Regurgitation*. *J Cardiothorac Vasc Anesth*, 2019. **33**(7): p. 1901-1911.
182. Barone-Rochette, G., et al., *Aortic valve area, stroke volume, left ventricular hypertrophy, remodeling, and fibrosis in aortic stenosis assessed by cardiac magnetic resonance imaging: comparison between high and low gradient and normal and low flow aortic stenosis*. *Circ Cardiovasc Imaging*, 2013. **6**(6): p. 1009-17.
183. Huxley, A.F., *Muscle structure and theories of contraction*. *Prog Biophys Biophys Chem*, 1957. **7**: p. 255-318.
184. Oomen, P.J.A., et al., *A rapid electromechanical model to predict reverse remodeling following cardiac resynchronization therapy*. *Biomech Model Mechanobiol*, 2022. **21**(1): p. 231-247.
185. Washio, T., et al., *Using Systolic Local Mechanical Load to Predict Fiber Orientation in Ventricles*. *Front Physiol*, 2020. **11**: p. 467.
186. Kamperidis, V., et al., *Left ventricular systolic function assessment in secondary mitral regurgitation: left ventricular ejection fraction vs. speckle tracking global longitudinal strain*. *Eur Heart J*, 2016. **37**(10): p. 811-6.
187. Bakkestrom, R., et al., *Cardiac remodelling and haemodynamic characteristics in primary mitral valve regurgitation*. *Open Heart*, 2018. **5**(2): p. e000919.
188. Myerson, S.G., et al., *Determination of Clinical Outcome in Mitral Regurgitation With Cardiovascular Magnetic Resonance Quantification*. *Circulation*, 2016. **133**(23): p. 2287-96.
189. Singh, A., et al., *Symptom Onset in Aortic Stenosis: Relation to Sex Differences in Left Ventricular Remodeling*. *JACC Cardiovasc Imaging*, 2019. **12**(1): p. 96-105.
190. Harrison-Bernard, L.M., *The renal renin-angiotensin system*. *Adv Physiol Educ*, 2009. **33**(4): p. 270-4.
191. Wong, P.C., J. Guo, and A. Zhang, *The renal and cardiovascular effects of natriuretic peptides*. *Adv Physiol Educ*, 2017. **41**(2): p. 179-185.
192. Lee, H.J., et al., *Diffuse Myocardial Fibrosis and Diastolic Function in Aortic Stenosis*. *JACC Cardiovasc Imaging*, 2020. **13**(12): p. 2561-2572.
193. Liu, B., et al., *Myocardial fibrosis in asymptomatic and symptomatic chronic severe primary mitral regurgitation and relationship to tissue characterisation and left ventricular function on cardiovascular magnetic resonance*. *J Cardiovasc Magn Reson*, 2020. **22**(1): p. 86.
194. Lee, S.P., et al., *Assessment of diffuse myocardial fibrosis by using MR imaging in asymptomatic patients with aortic stenosis*. *Radiology*, 2015. **274**(2): p. 359-69.
195. Polte, C.L., et al., *Characterization of Chronic Aortic and Mitral Regurgitation Undergoing Valve Surgery Using Cardiovascular Magnetic Resonance*. *Am J Cardiol*, 2017. **119**(12): p. 2061-2068.

196. Everett, R.J., et al., *Progression of Hypertrophy and Myocardial Fibrosis in Aortic Stenosis: A Multicenter Cardiac Magnetic Resonance Study*. Circ Cardiovasc Imaging, 2018. **11**(6): p. e007451.
197. Steadman, C.D., et al., *Determinants and functional significance of myocardial perfusion reserve in severe aortic stenosis*. JACC Cardiovasc Imaging, 2012. **5**(2): p. 182-9.
198. Uretsky, S., et al., *Quantification of left ventricular remodeling in response to isolated aortic or mitral regurgitation*. J Cardiovasc Magn Reson, 2010. **12**: p. 32.
199. Verbraecken, J., et al., *Body surface area in normal-weight, overweight, and obese adults. A comparison study*. Metabolism, 2006. **55**(4): p. 515-24.
200. Lang, R.M., et al., *Recommendations for cardiac chamber quantification by echocardiography in adults: an update from the American Society of Echocardiography and the European Association of Cardiovascular Imaging*. J Am Soc Echocardiogr, 2015. **28**(1): p. 1-39 e14.
201. Di Rienzo, M., et al., *Baroreflex contribution to blood pressure and heart rate oscillations: time scales, time-variant characteristics and nonlinearities*. Philos Trans A Math Phys Eng Sci, 2009. **367**(1892): p. 1301-18.
202. Nicks, A.M., et al., *Pressure overload by suprarenal aortic constriction in mice leads to left ventricular hypertrophy without c-Kit expression in cardiomyocytes*. Sci Rep, 2020. **10**(1): p. 15318.
203. Rodero, C., et al., *Calibration of Cohorts of Virtual Patient Heart Models Using Bayesian History Matching*. Ann Biomed Eng, 2023. **51**(1): p. 241-252.
204. Longobardi, S., A. Sher, and S.A. Niederer, *In silico identification of potential calcium dynamics and sarcomere targets for recovering left ventricular function in rat heart failure with preserved ejection fraction*. PLoS Comput Biol, 2021. **17**(12): p. e1009646.
205. Niederer, S.A., et al., *Creation and application of virtual patient cohorts of heart models*. Philos Trans A Math Phys Eng Sci, 2020. **378**(2173): p. 20190558.

## VITA

### Hossein Sharifi

#### EDUCATION

---

**University of Kentucky** Lexington, KY  
Ph.D. in Mechanical Engineering 2018 - Present  
Dissertation: Multiscale Modeling of Cardiac Growth and Baroreflex Control  
Advisor: [Jonathan F. Wenk](#)

**University of Kentucky** Lexington, KY  
M.S. in Civil Engineering 2016 - 2018  
Thesis: Finite Element Evaluation of 2-Cell RC Box Culverts  
Advisor: [Issam E. Harik](#)

**Shiraz University** Shiraz, Iran  
B.S. in Civil Engineering 2010 - 2014

#### PROFESSIONAL POSITIONS

---

**Dept. of Mechanical Engineering**, University of Kentucky, Lexington, KY  
Research Assistant 2018 – 2023

**Dassault Systèmes Corp.**, Providence, RI  
Industry Solution Technical (Cardiovascular Biomechanics Engineering) – Intern  
2022 – 2023

**Dept. of Civil Engineering**, University of Kentucky, Lexington, KY  
Research Assistant 2017 – 2018

**Kentucky Transportation Center**, University of Kentucky, Lexington, KY  
Research Assistant 2017

#### HONORS AND AWARDS

---

1. Awarded travel funding for attending to Cardiac Physiome Workshop 04/2023  
Source of funding: National Science Foundation (NSF)  
Amount: \$750
2. Awarded travel funding for attending to Cardiac Physiome Workshop 04/2023  
Source of funding: Dept. of Mechanical Engineering, University of Kentucky  
Amount: \$900
3. Awarded travel funding for attending to Summer Biomechanics, Bioengineering,  
and Biotransport Conference (SB3C) 06/2022

Source of funding: Dept. of Mechanical Engineering, University of Kentucky  
Amount: \$900

## PUBLICATIONS

---

1. **Sharifi H.**, Mann, C.K., Wenk J. F., Campbell K. S. *A multiscale model of the cardiovascular system that regulates arterial pressure via closed loop baroreflex control of chronotropism, cell-level contractility, and vascular tone*, Biomech Model Mechanobiol, (2022). <https://doi.org/10.1007/s10237-022-01628-8>
2. **Sharifi, H.**, Mann, C.K., Rockward, A.L. et al. *Multiscale simulations of left ventricular growth and remodeling*, Biophys Rev 13, 729–746 (2021). <https://doi.org/10.1007/s12551-021-00826-5>
3. **Sharifi H.**, Mann, C.K., Noor, A.Z., et al. *Reproducibility of systolic strain in mice using cardiac magnetic resonance feature tracking*, Cardiovasc Eng Tech, (2022). <https://doi.org/10.1007/s13239-022-00621-7>
4. **Sharifi H.**, Peiris A., Harik I. E., *Triage Method for Load Rating Bridge Size Two-Cell Reinforced Concrete Box Culverts for the AASHTO LRFD Design Load*, Structure and Infrastructure Engineering (2021). <https://doi.org/10.1080/15732479.2021.2015793>

## PRESENTATIONS AND TALKS

---

1. Title: Multiscale modeling of cardiac valve disease using cell-level signals to drive myocardial growth June 2022  
Conference: Summer Biomechanics, Bioengineering, and Biotransport Conference ([SB3C](#)), US, MD
2. Title: Multiscale modeling of LV growth under autonomic regulation of baroreflex feedback loop June 2021  
Conference: Summer Biomechanics, Bioengineering, and Biotransport Conference ([SB3C](#)) (Virtual)

